Numerical Modeling of Radar Response to Snow for Snow Depth Retrieval using Multiple Backscattering Measurements

Fatme Mazeh

▶ To cite this version:

Fatme Mazeh. Numerical Modeling of Radar Response to Snow for Snow Depth Retrieval using Multiple Backscattering Measurements. Optics / Photonic. Université Grenoble Alpes; Université Libanaise, 2018. English. NNT : 2018GREAT055 . tel-01952817

HAL Id: tel-01952817
https://theses.hal.science/tel-01952817

Submitted on 12 Dec 2018

Communauté
UNIVERSITÉ Grenoble Alpes

THÈSE

Pour obtenir le grade de

DOCTEUR DE LA COMMUNAUTÉ UNIVERSITÉ GRENOBLE ALPES

Spécialité : OPTIQUE ET RADIOFREQUENCES

Arrêté ministériel : 25 mai 2016

Présentée par

Fatme MAZEH

Thèse dirigée par **Fabien NDAGIJIMANA**, Professeur, UGA
et codirigée par **Jalal JOMAAH**

préparée au sein du **Laboratoire Laboratoire de Génie Electrique**
dans **l'École Doctorale Electronique, Electrotechnique, Automatique, Traitement du Signal (EEATS)**

Modélisation Numérique de la Réponse du Radar à la Neige pour Mesurer sa Profondeur avec la Technique de la Rétrodiffusion Multiple

Numerical Modeling of Radar Response to Snow for Snow Depth Retrieval using Multiple Backscattering Measurements

Thèse soutenue publiquement le **7 septembre 2018**,
devant le jury composé de :

Monsieur FABIEN NDAGIJIMANA
PROFESSEUR, UNIVERSITE GRENOBLE ALPES, Directeur de thèse
Monsieur MOHAMED RAMMAL
PROFESSEUR, UNIVERSITE LIBANAISE - LIBAN, Rapporteur
Monsieur MONCEF KADI
PROFESSEUR, ESIGELEC ROUEN, Rapporteur
Monsieur JALAL JOMAAH
PROFESSEUR, UNIVERSITE LIBANAISE - LIBAN, Directeur de thèse
Monsieur HUSSAM AYAD
PROFESSEUR ASSOCIE, UNIVERSITE LIBANAISE - LIBAN, Co-directeur de thèse
Monsieur ALI RAHHAL
MAITRE DE CONFERENCES, UNIV. INTERNATIONALE LIBANAISE - LIBAN, Examinateur
Monsieur GHALEB FAOUR
DIRECTEUR DE RECHERCHE, CONSEIL NAT. RECH. SCIENTIFIQUE - LIBAN, Président

Acknowledgements

First and foremost, I would like to thank *God Almighty* for giving me strength and ability to undertake this research study and complete it satisfactorily. Without God's blessings, this achievement would not have been possible.

The work of this thesis was made possible by the joint financial support of the *Lebanese University*, to whom go my grateful thanks. There are no proper words to express my deep gratitude and respect for my research supervisors, *Prof. Jalal Jomaah* and *Prof. Fabien Ndagijimana*, whose talent and enthusiasm has inspired me to devote myself into the path of seeking truth and knowledge. I thank for their support in building up my research career. I owe my deepest respect to them. I would like to thank the two universities, *Lebanese University* and *Grenoble University*, that I have spent my years in pursuing my PhD degree.

I am especially indebted to *Dr. Hussam Ayad* for his mentorship and guidance as my PhD co-supervisor, always willing to give me time and help when required. I learned from him how to analyze a problem from the first physical principle, and to move upon a solution based on careful logical deduction, experienced mathematical derivation, and physical insights. It is through answering his harsh questions that I learned to question and defend myself, and to argue my own viewpoint and explain it to others. I thank for his training in writing, in making a presentation, and in choosing a topic.

My sincere thanks must also go to *Dr. Ghaleb Faour*, the director of the National Council for Scientific Research (CNRS) in Lebanon – Remote Sensing Center, for serving in my dissertation committee. He generously gave me his time to provide me some information regarding snow properties in Lebanon and valuable comments toward improving my work. Many thanks also to my thesis reviewers *Prof. Mohamed Rammal* and *Prof. Moncef Kadi* for evaluating my work and giving their helpful suggestions and corrections. I would like to thank *Dr. Ali Rahhal* for his acceptance to participate as an examiner in the dissertation committee.

To my beloved mother *Souad*, who died last year … I miss you mom. This thesis is heartily dedicated to you for your great role in my life and your numerous sacrifices for educating and preparing me for my future. Mom, you are gone but your belief in me has made this journey possible. I hoped that you are still alive to see this thesis completed.

My acknowledgments are also owed to my classmates especially: *Kassem Jomaah*, *Bilal Hammoud*, and *Zeinab Fneich* who shared me their insightful thoughts, valuable data, and scientific discussion. They offer me complementary perspectives. Kassem and Bilal really helped me a lot in everything concerning France registration when I was not able to travel.

I am mostly grateful to the love I received from my family. Without the love and education from my father, nothing is possible. I am so grateful to my two sisters *Zeinab* and *Nour* who are always willing to hear me about my experiences.

Words cannot express how grateful I am to my dear husband *Mostafa*. I am so appreciative for his constant love, understanding, encouraging, and patience. His continuous support helped me to complete this research work.

List of Publications

❖ *Conference Publications:*

Mazeh, F., Ayad, H., Ndadijimana, F., Faour, G., Fadlallah, M., & Jomaah, J. (2016, September). Effective permittivity of snow for radar detection: Numerical validation by the fem method. In *Antennas and Propagation (MECAP), 2016 IEEE Middle East Conference on* (pp. 1-4). IEEE.

Mazeh, F., Hammoud, B., Ayad, H., Ndadijimana, F., Faour, G., Fadlallah, M., and Jomaah J. (2018). Snow depth retrieval algorithm from Radar Backscattering Measurements at L- and X-Band using Multi-Incidence Angles. In *The 2018 International Conference on High Performance Computing and Simulation (HPCS).*

Mazeh, F., Ayad, H., Khalil, A., Fadllallah, M., & Jomaah, J. (2014, November). A tri-band branch-line coupler design using double-Lorentz transmission line Metamaterial. In *Microwave Conference (APMC), 2014 Asia-Pacific* (pp. 1250-1252). IEEE.

Mazeh, F., Ayad, H., Khalil, A., Rahal, A., Fadllallah, M., Jomaah, J., & Ndagijimana, F. (2014, December). Design and optimization of a double-Lorentz transmission line for tri-band applications. In *Microwave Symposium (MMS), 2014 14th Mediterranean* (pp. 1-6). IEEE.

Mazeh, F., Ayad, H., Haroun, M., Jomaah, K., Ndagijimana, F. (2015). Even-odd mode of a tri-band double-Lorentz transmission line metamaterial. In *Third International Workshop on Metamaterial by Design (IWMb)*, Paris.

Mazeh, F., Ayad, H., Fadllallah, M., Ndagijimana, F., Jomaah, J. (2015, April). Even-odd mode analysis of a tri-band branch-line coupler based on double-Lorentz transmission lines. In *Lebanese Association for the Advancement of Science (LAAS)*, Lebanon.

❖ *Journal Publications:*

Mazeh, F., Ayad, H., Ndadijimana, F., Faour, G., Fadlallah, M., and Jomaah J. (2018). Numerical Analysis of Radar Response to Snow Using Multiple Backscattering Measurements for Snow Depth Retrieval. In *Progress In Electromagnetics Research (PIER B-2018).*

Mazeh, F., Ayad, H., Fadlallah, M., Joumaa, K., Jomaah, J., & Ndagijimana, F. (2016). Even-odd mode of a double-Lorentz metamaterial and its application to a tri-band branch-line coupler. *EPJ Applied Metamaterials*, *3*, 8.

Abstract

Study of snow is an important domain of research in hydrology and meteorology. It has been demonstrated that snow physical properties can be retrieved using active microwave sensors. This requires an understanding of the interaction between electromagnetic (EM) waves with natural media. The objective of this work is two-fold: to study numerically all physical forward models concerning the EM wave interaction with snow and to develop an inverse scattering algorithm to estimate snow depth based on radar backscattering measurements at different frequencies and incidence angles. For the first part, the goal is to solve the scattering calculations by means of the well-known electromagnetic simulator Ansoft High Frequency Structure Simulator (HFSS). The numerical simulations include: the effective permittivity of snow, surface scattering phenomena in layered homogeneous media (air-snow-ground) with rough interfaces, and volume scattering phenomena when treating snow as a dense random media. So, the critical issue for the first part of this thesis is testing the validity of theoretical forward models through a careful numerical setup.

For the second part, the study is extended to develop a retrieval method to estimate snow thickness over ground from backscattering observations at L- and X-band (2 and 10 GHz) using multiple incidence angles. The return signal from snow over ground is influenced by: surface scattering, volume scattering, and the noise effects of the radar system. So, the backscattering coefficient from the medium is modeled statistically by including a White Gaussian Noise (WGN) into the simulation. This inversion algorithm involves two steps. The first is to estimate snow density using L-band co-polarized backscattering coefficient at normal incidence. The second is to estimate snow depth from X-band co-polarized backscattering coefficients using two different incidence angles. For a 0.02 noise variance, all retrieved values have an error less than 2% for a snow depth range of [50-300] cm. This algorithm was verified by simulation using Agilent's SystemVue electronic system level design software.

.

Table of Contents

List of Figures

List of Tables

List of Abbreviations

MIMO:	Multiple-input multiple-output
HFSS:	High Frequency Structure Simulator
EM:	Electromagnetic
FEM:	Finite element method
TEM:	Transverse electromagnetic
LHC:	Left-handed circular
RHC:	Right-handed circular
PML:	Perfectly matched layer
PE:	Perfect electric
PM:	Perfect magnetic
FD:	Finite difference
FDTD:	Finite difference time domain
TVB:	Tinga Voss Blossey
PVS:	Polder Van Santen
PO:	Physical optics
GO:	Geometric optics
ECF:	Exponential correlation function
GCF:	Gaussian correlation function
ACF:	Autocorrelation function
LUT:	Look up table
RCS:	Radar cross section
I^2EM:	Improved integral equation model
PRISM:	Polarimetric radar inversion for soil moisture
SMART:	Soil moisture assessment radar technique
STL:	Stereolithographic
S^2RT/R:	Single scattering radiative transfer model
SWE:	Snow water equivalent
WGN:	White gaussian noise
FMCW:	Frequency Modulated Continuous Wave
SAR:	Synthetic Aperture Radar
SCLP:	Snow and Cold Land Processes
RT:	Radiative transfer

List of Symbols

ε': Electric permittivity of a material
ε_0: Free space permittivity (8.85×10^{-12} F/m)
μ': Magnetic permeability of a material
μ_0: Magnetic permeability of vacuum ($4\pi\times10^{-7}$ H/m)
ρ_v: volume charge density (C/m^3)
σ: conductivity (S/m)
E: Electric field intensity (V/m)
H: Magnetic field intensity (A/m)
J: Current density (A/m^2)
ω: Angular frequency (rad/s)
ε'': Dielectric loss factor of the material
$\tan\delta$: Dielectric loss tangent
γ: Propagation constant (rad/s)
u_p: Phase velocity (m/s)
λ: Wavelength (m)
k: Wavenumber (m^{-1})
η: Intrinsic impedance (Ω)
α: Attenuation constant (Np/m)
β: Phase constant (rad/m)
λ_0: Wavelength in free space (m)
c: Speed of wave in vacuum (m/s)
δ_s: Skin depth (m)
E_{x0}: x- component of the electric field
E_{y0}: y- component of the electric field
$\tau(z,t)$: Inclination angle
δ: Phase difference between y- and x- components of the electric field
ψ: Rotation angle
χ: Ellipticity angle
R: Axial ratio of the polarization ellipse
f: Frequency (GHz)
ε_{snow}: Permittivity of snow
ε_{soil}: Permittivity of soil
n: Index of refraction
θ_1: Incidence angle
θ_1': Reflection angle
θ_2: Refraction angle
θ_c: Critical angle

ρ_h: Reflection coefficient at horizontal polarization
ρ_v: Reflection coefficient at vertical polarization
T_h: Transmission coefficient at horizontal polarization
T_v: Transmission coefficient at vertical polarization
Γ: Reflectivity
T: Transmissivity
θ_B: Brewster angle
P: Effective reflection coefficient of a three-layered structure
d: Thickness (m)
σ^o: Backscattering coefficient (dB)
m_s Soil moisture (%)
H: Horizontal polarization
V: Vertical polarization
P_{inc}: Incident power (W)
P_{ref}: Reflected power (W)
S_{21}: Transmission coefficient
P: Electric dipole moment density
χ_e: Electric susceptibility
D: Flux density (As/m^2)
ε_e: Permittivity of the background
ε_i: Permittivity of inclusions
ε_{eff}: Effective permittivity
v_i: Volume fraction of inclusions
ε_{ds}: Dielectric constant of dry snow
ε_{ws}: Dielectric constant of wet snow
ε_i: Permittivity of ice
ρ_s: Snow density (g/cm3)
T °C: Temperature (°C)
m_v: Liquid water content in snow (%)
θ_s: Scattering angle
ϕ: Azimuth angle
G^t: Transmit antenna gain (dB)
G^r: Receive antenna gain (dB)
σ_{pq}: pq-polarized radar cross section (dB/m^2)
R: Range between target and antenna (m)
A: Illumination area (m^2)
S^s: Power density of the scattered wave (W/m^2)
S^i: Power density of the incident wave (W/m^2)
s: Rms height of the surface (m)
l: Correlation length of the surface (m)
ks: Electromagnetic roughness

J_0:	Zeroth order Bessel function of the first kind
γ^0_{pq}:	Bistatic scattering coefficient (dB)
L:	Surface length (m)
g:	Tapering parameter (m)
Γ_0:	Fresnel reflectivity at normal incidence
q:	Cross-polarized ratio
p:	Co-polarized ratio
σ^0_{as}:	Surface scattering component by the air/snow interface (dB)
σ^0_{v}:	Snow volume scattering component (dB)
σ^0_{gv}:	Multiple scattering component (dB)
σ^0_{g}:	Surface scattering by the snow/soil interface (dB)
r:	Snow grain size (mm)
a:	Albedo
κ_s:	Scattering losses (Np/m)
κ_e:	Extinction coefficient (Np/m)
κ_a:	volume absorption coefficient (Np/m)
N:	Number of surfaces
ρ_w:	Density of water (kg/m^3)
δ_p:	Penetration depth (m)
mu:	Mean
σ^2:	Variance
τ:	Optical depth (Np)

General Introduction

Seasonal snow has a great impact on the Earth's climate system due to its high albedo. It can reflect 80 to 90 percent of the incident solar radiation back into space; thus, regulating the Earth's energy balance. Moreover, one sixth of the total population of the world depends on snowmelt runoff to meet their fresh water needs [1] and for agricultural irrigation requirements [2]. In some drainage basins, rapid spring snowmelt may also cause flooding and thus predicting the runoff resulting from snowmelt is an important part of the flood control system [2, 3]. That's why there is a demand for an estimation of the snow depth as well as snow water equivalent (SWE) in an accurate manner.

The old classical method used to measure snow depth is probing a ruler through the snow to the ground surface with its zero point at the ground surface. That's what is called a fixed snow stake. This classical method needs a physical contact to reach the target. However, remote sensing is the key to monitor snow cover due to its capability to record, measure, and analyze information from a distance using electromagnetic radiation. Remote sensors are mounted on aircrafts or satellites to determine the snow cover area, snow depth, and snow water equivalent; but snow physical parameters can't be measured directly by these systems. Therefore, some electromagnetic theory study is required to obtain useful information from the sensor. The propagation process and the interaction of the electromagnetic wave with the target should be well understood as well as the target's electromagnetic properties and how they depend on its physical properties. Radiometers are passive microwave sensors that measure the thermal emission radiated by the target and need an external energy source which is -in most cases- the sun. Microwave radiometers can be used to retrieve the snow water equivalent of dry snow, but they cannot be used to distinguish wet snow and wet ground during the melting period [4]. That's why microwave radars are used as potential applications for the estimation of snow properties. Radars are active sensors that transmit a signal to the target and measure the signal scattered back from the target providing its own energy source.

The aim of this work is to develop the capability to characterize the remote target from the radar response. Such characterization starts with a prediction information about the dielectric model of the target, i.e. the effective permittivity of snow. Then, a great understanding of the scattering mechanism between an electromagnetic wave and air-snow-ground media is required so that the potential for information retrieval from the remote sensor is greater. Finally is the design of a high accurate sensor response based on the retrieval algorithms done. The first two levels are well presented in this thesis leaving the implementation of the radar for future work.

Physically, snow is a three component dielectric mixture: air, ice, and liquid water. Electromagnetically, it is characterized by a dielectric constant which depends on frequency, temperature, water content, density, shape of ice particles and water inclusions [5]. In theoretical microwave modeling of random media such as snow, the calculation of the effective permittivity is essential which describes propagation and attenuation. Investigation of the effective permittivity of snow started by Cumming 1952 [6] and a summary of dielectric models of snow is found in [5]. These models are extracted from classical electromagnetic mixing formulas where the effective medium approach is applied; thus, treating snow to be an isotropic medium under a restriction that the size of the inclusions is much smaller than the wavelength of the electromagnetic field used. By modeling snow to be a mixture of constituents, dry snow is a mixture of ice and air and wet snow is a mixture of air, ice, and water.

The objective of this thesis is two-fold: to study wave scattering phenomena in layered media with rough interfaces (air – snow - ground) and to develop an inverse scattering problem to estimate snow depth based on the use of a multiple-input multiple-output (MIMO) radar which has the potential to operate at two frequencies and can scan multiple incidence angles simultaneously. *Chapter 1* of this thesis begins with a brief overview regarding the properties of electromagnetic waves, and how they are reflected by layered media. Then, the numerical modeling approach for calculating the reflection coefficient of the air-snow-ground system with planar interfaces is presented using Ansoft's High Frequency Structure Simulator (HFSS). Horizontally and vertically polarized incident waves were tested and simulation results were in a good agreement with theoretical values.

It was necessary to study the inhomogeneity of snow to have an accurate estimation of its density for snow depth recover from the reflected signal toward the radar with a minimum error. This is described numerically in *Chapter 2* using the finite element method (FEM) where the effective permittivity of a fully 3-D mixture of snow is calculated. The effective permittivity (ε_{eff}) of snow is obtained from the transmission coefficient (S_{21}) which is related to ε_{eff} by a non-linear complex equation. The calculated permittivity distribution was also compared with the theoretical mixing models. It was shown that Looyenga's model best fits the FEM simulated results in both cases: overlapped and non-overlapped ice inclusions. That's why Looyenga's model will be used in the snow density estimation method.

In reality, air-snow and snow-ground interfaces are non-planar and the layers to be treated are heterogeneous. The main purpose of *Chapter 3* is to illustrate the backscatter behavior for multilayered homogeneous structures (air – snow - ground) with rough interfaces using an electromagnetic simulator. The backscattering coefficient as well as the bistatic scattering coefficient are calculated using an averaging process over N different rough surfaces with the same roughness conditions because it is impossible to model an infinite layer in HFSS. The surface scattering calculations were done for different incidence angles at a frequency that neglect the effect of the heterogeneity of snow. Then, the study is extended to treat snow as a heterogeneous mixture of air and ice to model the effect of volume scatterers in the snow volume which has a great impact in snow depth retrieval. The volume backscattering coefficient was calculated at frequency in the X-band spectrum because the effect of the ice inclusions can be well seen at such band. The calculated values were compared with the single-scattering radiative transfer (S^2RT/R) model. These numerical simulations were just a key to understand how electromagnetic waves are scattered by media and to choose the best fit forward model compared with the numerical results to use it in the snow depth retrieval algorithm.

Provided with the surface and volume scattering coefficients at different frequencies and incidence angles, *Chapter 4* will present an inverse scattering problem to retrieve the snow depth from the calculated L- and X-band (2 and 10 GHz) co-polarized backscattering coefficients at different incidence angles. That's the key to use a MIMO radar so that signals can be sent and received simultaneously. The return signal from the medium is due to the ground roughness, the snow volume, and the noise from the radar system. So, surface and volume scattering effects are modeled from physical forward models that best fit our numerical results, and noise effects are modeled by including a White Gaussian Noise (WGN) into the simulation. So, we used the statistical distribution of the backscattering coefficient under various snow depths, snow densities, and incident frequencies to retrieve snow depth. The developed algorithm requires that snow is dry. This inverse scattering problem involves two steps. The first is the estimation of snow density using L-band co-polarized backscattering measurement at normal incidence. The second is the recovery of the snow depth from X-band radar backscattering coefficients using two different incidence angles. Furthermore, the backscatter behavior of wet snow is also presented and a proposed algorithm to classify the snow cover state (dry or wet) is done.

Modern radar systems that operate in environments with strong clutter, noise and jamming require advanced digital signal processing techniques. Addressing this complexity requires the generation of realistic test signals and system-level scenarios that can be used to create and verify the radar signal processing algorithms. That’s why our algorithm was tested by simulating using Agilent’s SystemVue electronic system level design software in *Chapter 4* also. SystemVue is the shortest path from imagination to verified hardware for radar system designs by allowing the creative modeling of a radar system from transmitter to receiver. The snow target was modeled in the simulator using a Matlab script due to its high complexity of input parameters that is responsible for the calculation of the backscattering coefficient.

Finally is the *conclusion* that summarizes this work and provides recommendations for future work.

Chapter 1: Electromagnetic Wave Propagation and Reflection

1.1 INTRODUCTION

To understand how microwave sensors operate and how the electromagnetic (EM) quantities they measure are transformed into geophysical information, it is necessary to understand how EM waves interact with natural media [7]. Such interaction is called: scattering, absorption, transmission, and emission. The scattered electromagnetic energy measured by a radar depends on the properties of the target as well as the properties of the sensor itself (frequency, incidence angle, and the polarization of the antennas).

This chapter provides a review of the properties of EM waves and the wave reflection at planar boundaries. Then, the numerical modelling approach for calculating the reflection coefficient of the air-snow-ground system with planar interfaces is presented using an electromagnetic simulator. Ansoft's High Frequency Structure Simulator (HFSS) can model multilayer structures and predict the theoretical electromagnetic response utilizing the finite element method (FEM) by solving Maxwell's equations.

1.2 PLANE WAVES

A time-varying electric field induces a magnetic field and, conversely, a time-varying magnetic field induces an electric field. This cyclic pattern often results in electromagnetic waves propagating through free space and in natural media [7].

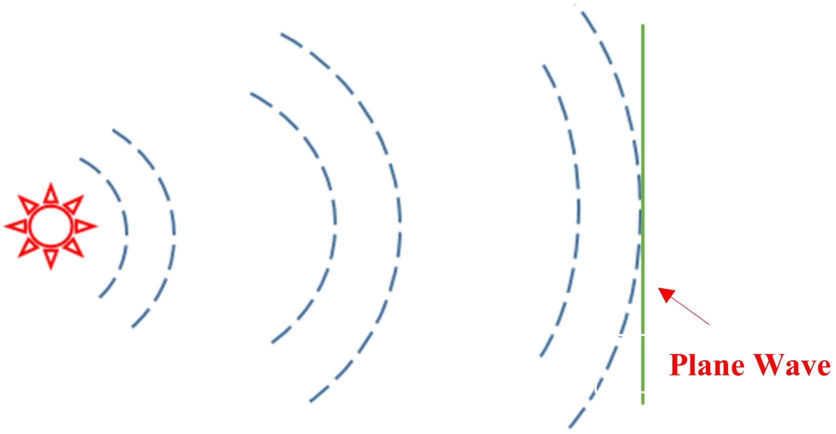

Figure 1-1: Waves radiated by EM waves to a distant observer.

A wave produced by an antenna expands in the form of a spherical wave. To an observer very far away from the source, the radius of the spherical wavefront increases. This wavefront appears approximately planar, as it if were part of a uniform plane wave with identical properties at all points in the plane tangent to the wavefront [7] as shown in Figure 1-1. Spherical waves are easily described using spherical coordinate system.

1.2.1 Constitutive Parameters

A specific medium is characterized by [8]:

- $\varepsilon'\varepsilon_0$ = electrical permittivity (F/m)
- $\mu = \mu' \mu_0$ = magnetic permeability (H/m)
- ρ_v = volume charge density (C/m^3)
- σ = conductivity (S/m)

where $\varepsilon_0=8.85\times10^{-12}$ F/m is the permittivity of free space and ε' is the permittivity of the material relative to that of free space. Similarly, the permeability of free space is $\mu_0=4\pi\times10^{-7}$ H/m and μ' is the relative magnetic permeability. In this thesis, we deal with non-magnetic media, i.e. $\mu'=1$. For a pure dielectric, $\sigma = 0$ and the propagating wave undergoes no attenuation; however, a conducting medium is a material with a non-zero conductivity and attenuation.

1.2.2 Maxwell's Equations

Maxwell's equations are the set of four fundamental equations governing electromagnetism describing the behavior of electric and magnetic fields. In a homogeneous isotropic medium, the differential form of Maxwell's equations is given by [9]:

$$\nabla . E = \frac{\rho_v}{\varepsilon' \varepsilon_0} \quad \text{(Gauss's law)} \tag{1.1a}$$

$$\nabla \times E = -\mu \frac{\partial H}{\partial t} \quad \text{(Faraday's law)} \tag{1.1b}$$

$$\nabla . \mathrm{H} = 0 \quad \text{(Gauss's law for magnetism)} \tag{1.1c}$$

$$\nabla \times H = J + \varepsilon' \varepsilon_0 \frac{\partial E}{\partial t} \quad \text{(Ampere's law)} \tag{1.1d}$$

where E is the electric field intensity in (V/m), H is the magnetic field intensity in (A/m), and J is the current density in (A/m^2) flowing through the medium. Maxwell's equations form the foundation of electromagnetism, optics, and electric circuits. For time-harmonic quantities, Maxwell's equations assume the following form in the phasor domain:

$$\nabla . E = \frac{\rho_v}{\varepsilon ' \varepsilon_0} \tag{1.2a}$$

$$\nabla \times E = -j\omega\mu H \tag{1.2b}$$

$$\nabla . \mathrm{H} = 0 \tag{1.2c}$$

$$\nabla \times H = J + j\omega\varepsilon ' \varepsilon_0 E \tag{1.2d}$$

1.2.3 Complex Permittivity

In a medium with conductivity (σ), the conduction current density (J) is related to the electric field (E) by ohm's law (J = σ E). Substituting ohm's law in (1.2d), the fourth Maxwell's equation can be written as:

$$\nabla \times H = j\omega\varepsilon_0 (\varepsilon ' - \mathrm{j}\frac{\sigma}{\omega\varepsilon_0})E \tag{1.3}$$

So, the complex dielectric constant (ε) can be written in terms of a real part (ε') and an imaginary part (ε") as in (1.4):

$$\varepsilon = \varepsilon ' - j\frac{\sigma}{\omega\varepsilon_0} \tag{1.4}$$

where

$$\varepsilon '' = \frac{\sigma}{\omega\varepsilon_0} \tag{1.5}$$

ε" is called the dielectric loss factor of the material. For a lossless medium with $\sigma = 0$, it follows that ε" = 0 and ε = ε'. The ratio ε" / ε' is called the dielectric loss tangent because it measures the power loss in the medium.

$$\tan\delta = \frac{\varepsilon ''}{\varepsilon '} \tag{1.6}$$

1.2.4 Wave Equation

The equations (1.2a), (1.2b), (1.2c), and (1.2d) are first order differential equations with two variables E and H. They can be combined to give a second order equation in E or H alone known as the homogeneous vector wave equation. After taking the curl of both sides of (1.2b) and using appropriate substitution, the homogeneous wave equation for E is given by [8]:

$$\nabla^2 E + \omega^2 \mu\varepsilon\varepsilon_0 E = 0 \tag{1.7}$$

The propagation constant (γ) is defined by:

$$\gamma^2 = -\omega^2 \mu\varepsilon\varepsilon_0 \tag{1.8}$$

where the wave equation can be written as:

$$\nabla^2 E - \gamma^2 E = 0 \tag{1.9}$$

1.3 PLANE WAVE PROPAGATION

Waves may propagate in both lossless and lossy media. An electromagnetic wave can propagate in a lossless medium with no loss of energy (zero attenuation). However, a lossy medium (with non-zero conductivity) absorbs part of the energy carried by an EM wave traveling through it (non-zero attenuation) [7].

1.3.1 Lossless Media

The properties of an electromagnetic wave, such as its phase velocity (u_p) and wavelength (λ), depend on the angular frequency (ω) and the medium's three constitutive parameters: ε', μ, and σ [7]. If the medium is nonconducting ($\sigma = 0$), the wave does not suffer any attenuation as it travels and hence the medium is said to be lossless ($\varepsilon = \varepsilon'$) [8]. For a lossless media, it is usual to define the wavenumber (*k*) as:

$$k = \omega\sqrt{\mu\varepsilon'\varepsilon_0} \tag{1.10}$$

The wave equation will then be written as:

$$\nabla^2 E + k^2 E = 0 \tag{1.11}$$

The intrinsic impedance (η) of a lossless medium is defined as:

$$\eta = \sqrt{\frac{\mu}{\varepsilon'\varepsilon_0}} \tag{1.12}$$

It can be shown that, for any uniform plane wave traveling in an arbitrary direction k, the electric and magnetic field phasors E and H are related as:

$$H = \frac{1}{\eta} k \times E \tag{1.13a}$$

$$E = -\eta k \times H \tag{1.13b}$$

The relations given by (1.13a) and (1.13b) are valid for lossless and lossy media but with a different expression for η. The phase velocity of the wave (u_p) is defines as:

$$u_p = \frac{\omega}{k} = \frac{1}{\sqrt{\mu\varepsilon'\varepsilon_0}} \tag{1.14}$$

In vacuum where $\varepsilon' = 1$, the phase velocity (u_p) is equal to 299,792,458 m/s and the intrinsic impedance (η) is equal to 377 Ω.

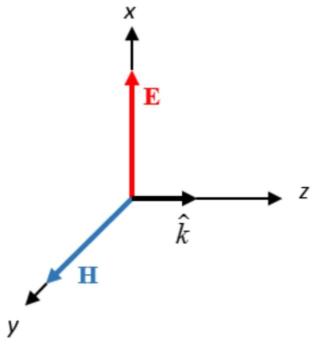

Figure 1-2: TEM wave propagating in the z-direction.

Because the electric field and magnetic fields are perpendicular to each other, and both are perpendicular to the direction of wave travel, this wave is said to be transverse electromagnetic (TEM) as illustrated in Figure 1-2. E(z,t) and H(z,t) exhibit the same functional dependence on z and t, they are said to be in phase; when the amplitude of one of them reaches a maximum, the amplitude of the other does so too [7]. The fact that E and H are in phase is characteristic of waves propagating in lossless media.

1.3.2 Lossy Media

If a medium is conducting ($\sigma \neq 0$), a current ($J = \sigma E$) will flow; hence, the dielectric constant will have a non-zero imaginary part ($\varepsilon'' \neq 0$). Since γ is complex, it can be expressed as:

$$\gamma = \alpha + j\beta \qquad (1.15)$$

where α is the medium's attenuation constant and β is its phase constant with their expressions shown in (1.16a) and (1.16b) respectively.

$$\alpha = -\omega\sqrt{\mu\varepsilon_0}\,\mathrm{Im}\left\{\sqrt{\varepsilon}\right\} \quad (\mathrm{Np/\,m}) \qquad (1.16a)$$

$$\beta = \omega\sqrt{\mu\varepsilon_0}\,\mathrm{Re}\left\{\sqrt{\varepsilon}\right\} \quad (\mathrm{rad/\,m}) \qquad (1.16b)$$

Using the rules of complex algebra and in the case of low-loss dielectrics, (1.16a) and (1.16b) leads to [8]:

$$\alpha \approx \frac{\pi\varepsilon''}{\lambda_0\sqrt{\varepsilon'}} \quad (\mathrm{Np/\,m}) \qquad (1.17a)$$

$$\beta \approx \frac{2\pi}{\lambda_0}\sqrt{\varepsilon'} \quad (\mathrm{rad/\,m}) \qquad (1.17b)$$

where $\lambda_0 = c\,/\,f$ is the wavelength in free space. Thus a wave travelling in a lossy medium will be attenuated by a factor of $e^{-\alpha z}$. As the field attenuates, part of the power carried by an EM wave gets converted into heat due to conduction in the medium. As the wave travels a distance δ_s, the wave travelled through the medium is attenuated by a factor e^{-1}.

$$\delta_s = \frac{1}{\alpha} \quad \text{(m)} \tag{1.18}$$

This distance is called the skin depth of the medium which characterizes how deep an electromagnetic wave can penetrate into a conducting medium [10]. The intrinsic impedance of the lossy medium is defined as:

$$\eta = \sqrt{\frac{\mu_0}{\varepsilon'\varepsilon_0}}(1 - \mathrm{j}\frac{\varepsilon''}{\varepsilon'})^{-1/2} \quad (\Omega) \tag{1.19}$$

1.4 WAVE POLARIZARION

The polarization of a uniform plane wave describes the time varying behavior of the electric field intensity vector at a given point in space [10]. The polarization state can be linear, circular, or elliptical. For a plane wave travelling in the $+z$ direction, the electric field phasor E(z) is given by:

$$E(\mathrm{z}) = \mathrm{E}_{x0}\, e^{-jkz}\, x + \mathrm{E}_{y0}\, e^{-jkz}\, y \tag{1.20}$$

The two amplitudes E_{x0} and E_{y0} are complex quantities characterized by a magnitude and a phase angle. The polarization of the wave depends on the phase of E_{y0} relative to that of E_{x0}. So, we can define E_{x0} and E_{y0} as:

$$\mathrm{E}_{x0} = a_x \tag{1.21a}$$

$$\mathrm{E}_{y0} = a_y e^{j\delta} \tag{1.21b}$$

where δ is the phase difference between the y- and x- components of E, $a_x = |E_{x0}| \geq 0$, and $a_y = |E_{y0}| \geq 0$. So, the corresponding instantaneous field is:

$$\begin{aligned} E(\mathrm{z,t}) &= \mathrm{Re}[\mathrm{E(z)}e^{j\omega t}] \\ \mathrm{E(z,t)} &= a_x \cos(\omega \mathrm{t} - \mathrm{kz})x + a_y \cos(\omega \mathrm{t} - \mathrm{kz} + \delta)y \end{aligned} \tag{1.22}$$

At a specific position z, the direction of E(z,t) is characterized by its inclination angle τ(z,t), defined with respect to the x-axis and its magnitude |E(z,t)|.

$$|E(\mathrm{z,t})| = \left[a_x^2 \cos^2(\omega \mathrm{t} - kz) + a_y^2 \cos^2(\omega \mathrm{t} - kz + \delta)\right]^{1/2} \tag{1.23}$$

$$\tau(\mathrm{z,t}) = \tan^{-1}\left[\frac{E_y(\mathrm{z,t})}{E_x(\mathrm{z,t})}\right] \tag{1.24}$$

1.4.1 Linear Polarization

A wave is said to be linearly polarized if for a fixed *z*, the tip of the E(z,t) traces a straight line segment as a function of time [7]. This happens when $E_x(z,t)$ and $E_y(z,t)$ are in phase ($\delta = 0$) or out of phase ($\delta = \pi$). Figure 1-3 illustrates a linearly polarized travelling wave.

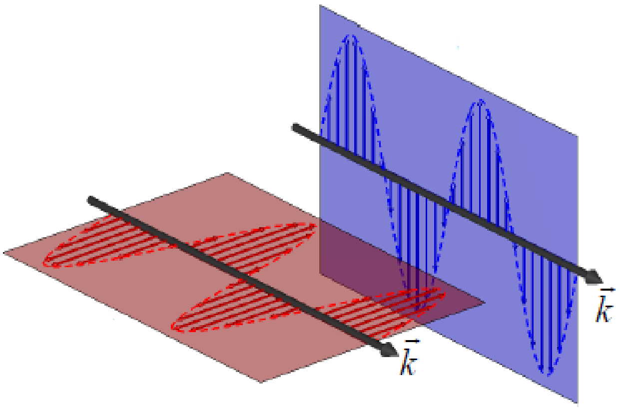

Figure 1-3: Linearly polarized travelling wave [11].

If $a_y = 0$, then $\tau = 0$ or π, and the wave is *x*-polarized; however, if $a_x = 0$, then $\tau = \pm\pi/2$, and the wave is *y*-polarized.

1.4.2 Circular Polarization

A wave is said to be circularly polarized if the magnitudes of the x- and y- components of E(z) are equal and the phase difference δ is $\pm \pi/2$. It is called left-handed circularly polarized if $\delta = \pi/2$ and right-handed circularly polarized if $\delta = -\pi/2$.

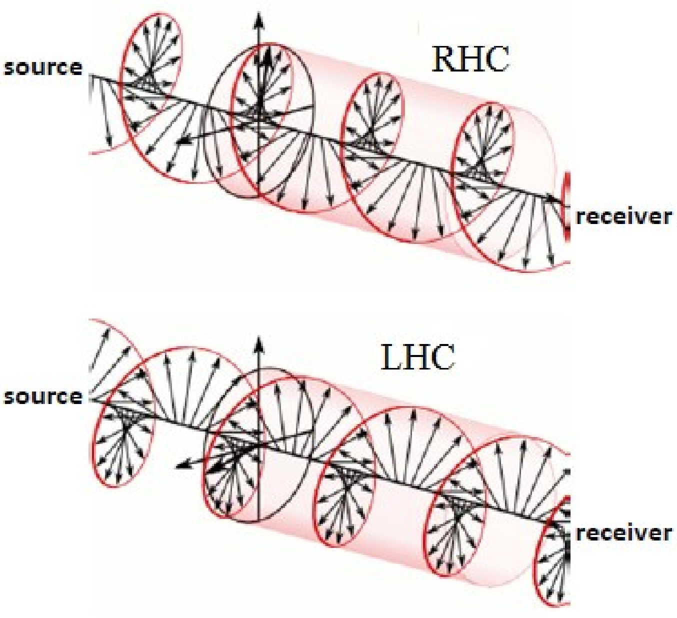

Figure 1-4: Circularly polarized plane waves [11].

For a left-handed circular (LHC) polarization where $a_x = a_y$ and $\delta = \pi/2$, the inclination angle is:

$$\tau(z,t) = -(\omega t - kz) \tag{1.25}$$

For a right-handed circular (RHC) polarization where $a_x = a_y$ and $\delta = -\pi/2$, the inclination angle is:

$$\tau(z,t) = (\omega t - kz) \tag{1.26}$$

Polarization is taken as the time-varying electric field view with the wave coming toward you. As viewed from the receiver in Figure 1-4, the LHC polarization case is shown where the tip of E(z,t) rotates in a clockwise direction; similarly for that of the RHC polarization where the tip of E(z,t) rotates in a counter clockwise direction.

1.4.3 Elliptical Polarization

A wave is said to be elliptically polarized when the tip of E(z,t) traces an ellipse in the plane perpendicular to the direction of propagation. The shape of the ellipse and the field's handedness (left-handed or right-handed) are determined by the values of the ratio (a_y / a_x) and the phase difference δ. The polarization ellipse is shown in Figure 1-5 where the length of its major axis is *a* and the length of its major axis is *b*. The rotation angle ψ is defined as the angle between the major axis of the ellipse and a reference direction, chosen here to be the *x*-axis.

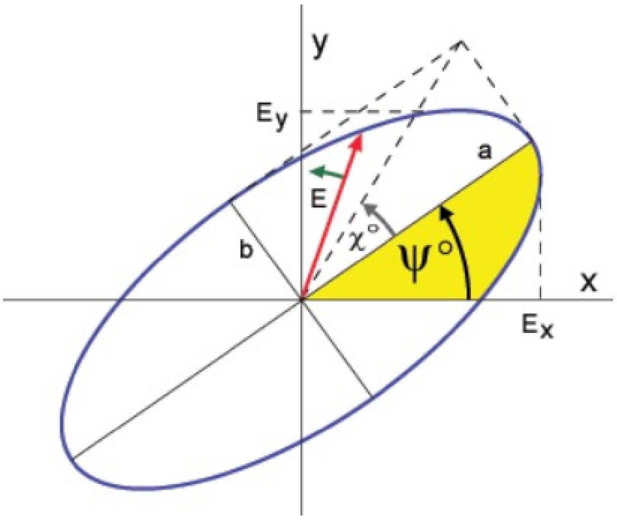

Figure 1-5: Polarization ellipse with the x-y plane [12].

The shape of the ellipse and its handedness are characterized by the ellipticity angle χ, defined as:

$$\tan \chi = \pm \frac{b}{a} \tag{1.27}$$

For the left-handed rotation, tan χ is positive; and for the right handed rotation, tan χ is negative. The quantity R = a / b is called the axial ratio of the polarization ellipse, and it varies between 1 for circular polarization and ∞ for linear polarization.

1.5 WAVE REFLECTION AND TRANSMISSION AT OBLIQUE INCIDENCE

In this section, reflections and transmissions at oblique wave incidence is examined for two different wave polarizations. The special cases of particular interest in remote sensing are treated. The $z = 0$ plane forms the boundary between media 1 and 2 with constitutive parameters (ε_1', μ_0) and (ε_2', μ_0), respectively. To analyze reflections and transmissions at oblique angles of incidence, we need to introduce the plane of incidence, which is defined as the plane containing the direction of wave travel, k_{inc}, and the surface normal to the boundary. When the electric field is perpendicular to the plane of incidence, the polarization of the wave is referred to as perpendicular polarization [8]. When the electric field is parallel to the plane of incidence, the polarization is referred to as parallel polarization [8].

In remote sensing, the polarization with E perpendicular to the plane of incidence is also called horizontal polarization (E-polarization) because E is parallel to Earth's surface, and that with E parallel to the plane of incidence is called vertical polarization (H-polarization) because in this case it is the magnetic field that is parallel to Earth's surface [7].

The angles of incidence, reflection, and transmission, defined with respect to the normal to the boundary (the z-axis), are θ_1, θ_1', and θ_2, respectively. These three angles are interrelated by Snell's laws.

$$\theta_1 = \theta_1' \qquad \text{(Snell's law of reflection)} \qquad (1.28)$$

$$\gamma_2 \sin\theta_2 = \gamma_1 \sin\theta_1 \qquad \text{(Snell's law of refraction)} \qquad (1.29)$$

The index of refraction (n) of a nonmagnetic material is defined as:

$$n = \sqrt{\varepsilon'} \qquad (1.30)$$

A material is denser than another material if it has a greater index of refraction. The value of the incidence angle (θ_1) that corresponds to a 90° refraction angle is called the critical angle (θ_c). In this case, the refracted wave propagates along the surface with no transmitted energy into medium 2.

$$\sin\theta_c = \sqrt{\frac{\varepsilon'_2}{\varepsilon'_1}} \qquad (1.31)$$

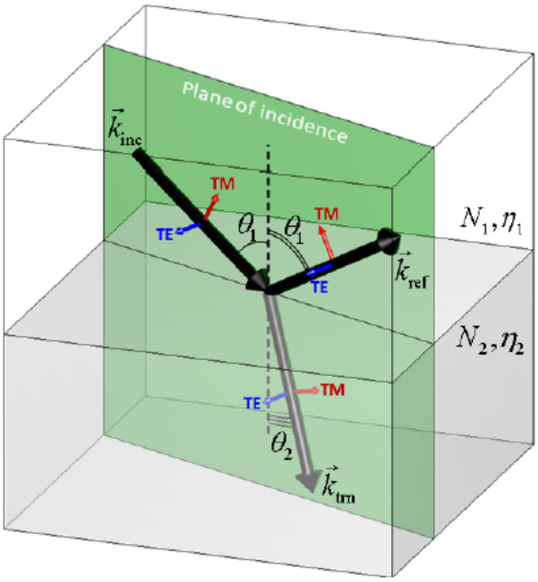

Figure 1-6: Wave reflection and refraction at a planar boundary between different media [11].

The Fresnel reflection (ρ_h) and transmission coefficients (T_h) for horizontal polarization are defined as:

$$\rho_h = \frac{\eta_2 \cos\theta_1 - \eta_1 \cos\theta_2}{\eta_2 \cos\theta_1 + \eta_1 \cos\theta_2} \tag{1.32}$$

$$\tau_h = \frac{2\eta_2 \cos\theta_1}{\eta_2 \cos\theta_1 + \eta_1 \cos\theta_2} \tag{1.33}$$

$$\tau_h = 1 + \rho_h \tag{1.34}$$

The Fresnel reflection (ρ_v) and transmission coefficients (T_v) for vertical polarization are defined as:

$$\rho_v = \frac{\eta_2 \cos\theta_2 - \eta_1 \cos\theta_1}{\eta_2 \cos\theta_2 + \eta_1 \cos\theta_1} \tag{1.35}$$

$$\tau_v = \frac{2\eta_2 \cos\theta_1}{\eta_1 \cos\theta_1 + \eta_2 \cos\theta_2} \tag{1.36}$$

$$\tau_v = 1 + \rho_v \tag{1.37}$$

The reflection and transmission coefficients are defined as the ratios of the reflected and transmitted electric field amplitudes to the amplitude of the incident electric field [7]. However, the reflectivity (Γ) is the ratio of the reflected power to the incident power and the transmissivity (T) is the ratio of the transmitted power to the incident power. The reflectivity and the transmissivity are defined by (1.36) and (1.37) respectively:

$$\Gamma = |\rho|^2 \tag{1.38}$$

$$\mathrm{T} = |\tau|^2 \frac{\eta_1 \cos\theta_2}{\eta_2 \cos\theta_1} \tag{1.39}$$

$$\mathrm{T} = 1 - \Gamma \tag{1.40}$$

The incident angle θ_1 which reduces the reflection coefficient for vertical polarization to zero, is referred to as the Brewster angle (θ_B) [10]. For nonmagnetic materials, the Brewster angle exists only for vertical polarization, and its value depends on the ratio ($\varepsilon_2' / \varepsilon_1'$) [7]. At the Brewster angle, the vertically polarized component of the incident wave is totally transmitted into medium 2. Taking $\rho_v = 0$ gives that $\eta_1 \cos\theta_1 = \eta_2 \cos\theta_2$. Applying then Snell's law for nonmagnetic material, Brewster angle (θ_B) will be then defined by:

$$\theta_B = \tan^{-1}\sqrt{\frac{\varepsilon_2'}{\varepsilon_1'}} \tag{1.41}$$

The Brewster angle is also called the polarizing angle. This is because, if a wave composed of both horizontal and vertical polarization components is incident upon a non-magnetic surface at the Brewster angle θ_B, the vertically polarized component is totally transmitted into the second medium, and only the horizontally polarized component is reflected by the surface [10].

1.6 NUMERICAL SIMULATION OF A TWO LAYERED STRUCTURE

1.6.1 HFSS Overview

One of the objectives of this study is to validate numerically the forward models that are capable to explain the interaction of EM waves with the snow medium using the simulation software Ansoft's High Frequency Structure Simulator (HFSS). Ansoft's HFSS [13] is an electromagnetic simulator used to predict the theoretical electromagnetic response of various structures utilizing the finite element method (FEM). HFSS can find a solution to Maxwell's equations for heterogeneous structures as well as multilayered structures and even including inclusions. The basic idea of the finite element method is to divide the full problem space into many smaller regions (elements) -known as the mesh- and represents the field in each element by a local function taking into account the boundary conditions [14]. In HFSS, such elements take the form of tetrahedral. The mesh is refined many times with progressively smaller elements with a new solution being obtained after each refinement. A final solution is obtained when reaching convergence depending on the value of ΔE (the change in the calculated energy value).

Before starting the calculation, the HFSS structure setup should be well drawn with its suitable boundary conditions and excitations. Material properties should be assigned to the geometric model using the material manager. Throughout the simulation setups done in this thesis, incident plane wave excitation is used where the incident angle and the excitation are specified using spherical polar coordinates. Depending on the type of the problem to be solved, boundary conditions must be assigned to the outer faces of the model. The boundary conditions used in the simulations done in Chapters 1 and 3 are: perfectly matched layer (PML), layered impedance, and master/slave; while, perfect electric conductor (PEC) and perfect magnetic conductor (PMC) are applied in Chapter 2.

There are two types of boundary conditions that are used to design infinite periodic structure. HFSS provides the combination of PEC and PMC as well as master-slave boundary conditions to realize a periodic design. A perfectly matched layer is an artificial absorbing layer for electromagnetic fields, commonly used in numerical methods to simulate problems with open boundaries. The key property of a PML is the ability to strongly absorb outgoing waves from the interior of a computational region without reflecting them back into the interior. The applied layered impedance boundary condition in this thesis acts as if there is an infinite material on the other side of the boundary providing a total absorption. It can also be used to create a change in permittivity at the boundary. In this work, a layered impedance boundary condition was applied below the structure to achieve a half-space ground layer. Once the boundaries and materials are assigned for a geometry model, HFSS then uses the finite element method to solve the problem. Reflection coefficients are evaluated using the HFSS field calculator which we will discuss later.

1.6.2 Numerical Results of $|\rho_h|$ and $|\rho_v|$ for Air - Soil Composite

As a first step in this thesis, the electromagnetic response of air-ground (soil) structure is studied where the dielectric constant of air is 1 and that of wet soil is 25. In this section, the air-ground interface is considered to be flat where the effect of surface roughness is added later.

Table 1-1 shows a comparison between numerical simulations and theoretical values for different incidence angles in case of horizontal and vertical polarizations. To illustrate the variations of the magnitudes of ρ_h and ρ_v, Figure 1-7 shows the plots for an incident wave in air into a dielectric surface of wet soil. It can be seen from this figure that $|\rho_h| = |\rho_v|$ at normal incidence ($\theta_1 = 0^\circ$), as expected, $|\rho_h| = |\rho_v| = 1$ at grazing incidence ($\theta_1 = 90^\circ$), and $|\rho_v| = 0$ at Brewster angle ($\theta_B = 78.69^\circ$).

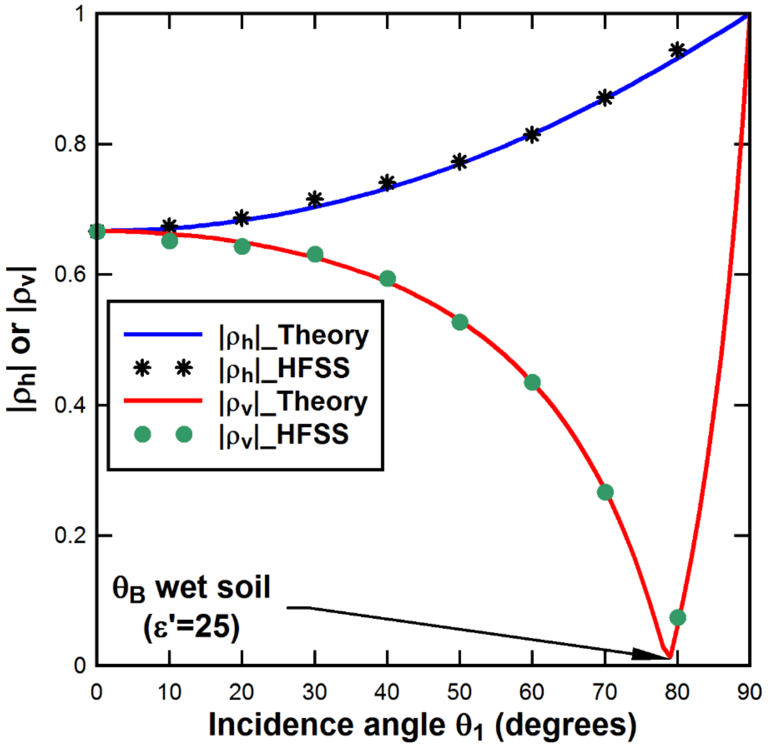

Figure 1-7: Plots for $|\rho_h|$ and $|\rho_v|$ as a function of θ_1 for incidence in air upon wet soil (ε' = 25).

Table 1-1: Bistatic Reflection Coefficient for Air/Ground Two-Layered Model.

	Horizontal Polarization		**Vertical Polarization**	
Incidence Angle	$|\rho_h|$_HFSS	$|\rho_h|$_Theory	$|\rho_v|$_HFSS	$|\rho_v|$_Theory
0°	0.6667	0.6667	0.6667	0.6667
10°	0.6707	0.6742	0.6520	0.6625
20°	0.6829	0.6866	0.6437	0.6497
30°	0.7035	0.7154	0.6316	0.6263
40°	0.7324	0.7409	0.5942	0.5887
50°	0.7698	0.7734	0.5275	0.5296
60°	0.8156	0.8146	0.4353	0.4348
70°	0.8697	0.8715	0.2668	0.2703
80°	0.9316	0.9442	0.0745	0.0607

1.7 LAYERED MEDIA

A reflected signal is obtained when there is a dielectric contrast between two media. The three materials of interest in this thesis are: air, snow, and ground (soil). The permittivity of air is close to one under all conditions. For the case of snow and ground, it is more complex. Dry snow behaves as a mixture of air and ice, resulting in a permittivity that can vary from 1 to

3.15. Its imaginary part is much smaller than the real part and will not have a large effect on the reflection coefficient. As snow wetness increases, the real and imaginary part of the dielectric constant of snow increases.

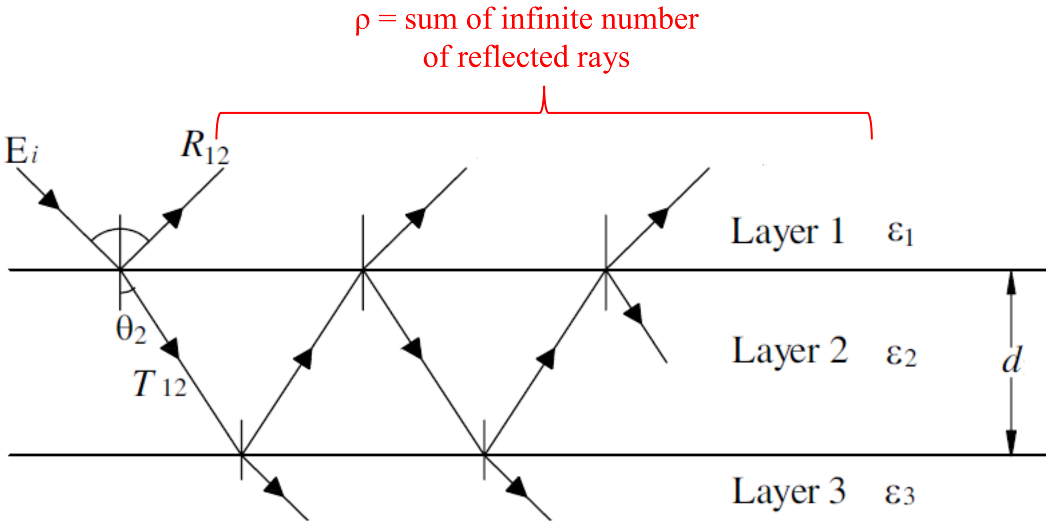

Figure 1-8: Three-layered structure with planar boundaries [15].

Figure 1-8 shows a physical model of a three-layered structure with planar boundaries. This model assumes a large distance of air followed by the depth of the middle layer (snow) and then a half-space of medium 3 (ground). Snow is a low-loss medium when dry and lossy when wet.

The effective reflection coefficient (ρ) for such three-layered structure is derived using the multiple reflection method [7] for horizontal and vertical polarization. The expression of ρ can be derived by tracking all the multiple reflections and transmissions that occur at the two boundaries. The various reflection, transmission, and propagation mechanisms encountered by a wave incident in medium 1 upon medium 2 at incidence angle θ_1 include:

- ρ_{12} = reflection coefficient at the boundary between media 1 and 2, for incidence in medium 1 at angle θ_1.
- ρ_{21} = reflection coefficient at the boundary between media 1 and 2, for incidence in medium 2 at angle θ_2. Note that $\rho_{21} = -\rho_{12}$.
- τ_{12} = transmission coefficient from medium 1 to medium 2 when incidence is at angle θ_2. Note that $\tau_{12} = 1+\rho_{12}$ for h polarization and $\tau_{12} = (1+\rho_{12})\cos\theta_2 / \cos\theta_1$ for v polarization.

- τ_{21} = transmission coefficient from medium 2 to medium 1 when incidence is at angle θ_2. Note that $\tau_{21} = 1+ \rho_{21}$ for h polarization and $\tau_{21} = (1+ \rho_{21}) \cos\theta_2 / \cos\theta_1$ for v polarization.
- $L = e^{-\gamma 2d\cos\theta 2}$ = propagation factor in medium 2 between its top boundary and bottom boundary (or between its bottom boundary and top boundary) along angle θ_2.
- ρ_{23} = reflection coefficient at the boundary between media 2 and 3, for incidence in medium 2 at angle θ_2. Note that $\rho_{21} = - \rho_{12}$.

For an incident field with E^i_0 = 1 V/m, the first reflection contribute to ρ_{12}, the second one is $\tau_{21}\rho_{23}L^2\tau_{12}$, and so on. Summing up all the upward moving waves in medium 1 gives:

$$\begin{aligned}\rho &= \rho_{12} + \tau_{21}\rho_{23}L^2\tau_{12} + \tau_{21}\rho_{23}^2\rho_{21}L^4\tau_{12} + \ldots \\ &= \rho_{12} + \tau_{21}\tau_{12}\rho_{23}L^2(1 + \mathrm{x} + \mathrm{x}^2 + \ldots)\end{aligned} \tag{1.42}$$

where $x = \rho_{12}\rho_{23}L^2$. We note that the magnitudes of ρ_{12}, ρ_{23}, and L^2 are all smaller than 1. Hence, $x < 1$. If we make the substitutions $\tau_{21} = 1 + \rho_{21} = 1 - \rho_{12}$, $\tau_{12} = 1 + \rho_{12}$, and $1 / (1-x) = 1 + x + x2 + \ldots$, equation (1.40) becomes:

$$\rho = \rho_{12} + \frac{(1-\rho_{12})(1+\rho_{12})\rho_{23}L^2}{1-\rho_{21}\rho_{23}L^2} \tag{1.43}$$

Upon making the substitutions $\rho_{21} = - \rho_{12}$ and $L^2 = e^{-2\gamma 2d\cos\theta 2}$ and simplifying the expression, we obtain:

$$\rho = \frac{\rho_{12} + \rho_{23}e^{-2\gamma_2 d\cos\theta_2}}{1+\rho_{12}\rho_{23}e^{-2\gamma_2 d\cos\theta_2}} \tag{1.44}$$

where d is the thickness of the middle layer, γ_2 is the propagation constant in medium 2, and θ_2 is the refraction angle in medium 2. All the derivation process is from [7, Section 2-10.3].

For the horizontally polarized case:

$$\rho_{12} = \frac{\eta_2\cos\theta_1 - \eta_1\cos\theta_2}{\eta_2\cos\theta_1 + \eta_1\cos\theta_2} \tag{1.45a}$$

$$\rho_{23} = \frac{\eta_3\cos\theta_2 - \eta_2\cos\theta_3}{\eta_3\cos\theta_2 + \eta_2\cos\theta_3} \tag{1.45b}$$

For the vertically polarized case:

$$\rho_{12} = \frac{\eta_2\cos\theta_2 - \eta_1\cos\theta_1}{\eta_2\cos\theta_2 + \eta_1\cos\theta_1} \tag{1.46a}$$

$$\rho_{23} = \frac{\eta_3 \cos\theta_3 - \eta_2 \cos\theta_2}{\eta_3 \cos\theta_3 + \eta_2 \cos\theta_2} \tag{1.46b}$$

where η is the intrinsic impedance of the medium.

1.8 NUMERICAL MODELING OF A MULTILAYERED STRUCTURE IN HFSS

1.8.1 Model Description

The main objective of this thesis is to estimate snow depth over ground using a microwave sensor. However, the backscattering coefficient σ^0 measured by radars depends on the Fresnel reflection coefficients of the surface. So, it is important to be able to model the reflection coefficient of a multi-layered structure. A specific scenario of interest is when a soil surface is covered by a layer of snow. The problem is modelled as a three-layer configuration:

Medium 1: Air

Medium 2: Uniform layer of snow of thickness *d*

Medium 3: Ground (Soil).

Table 1-2: Geophysical Data of Snow over Ground

Medium	Depth (m)	Permittivity
Air	4	1
Snow	0.3	1.9
Ground	Half-space	11.3-j1.5
Air/Snow Interface: Planar Snow/Ground Interface: Planar		

In this section, the snow and ground layers are considered to be homogeneous with an effective permittivity constant. The surfaces are considered to be flat where the surface roughness effect is included later. For a snow density of 0.45 g/cm^3, the effective permittivity of dry snow is 1.9; however, for low soil moisture (m_s = 20%), a permittivity of 11.3-j1.5 is used for the soil layer.

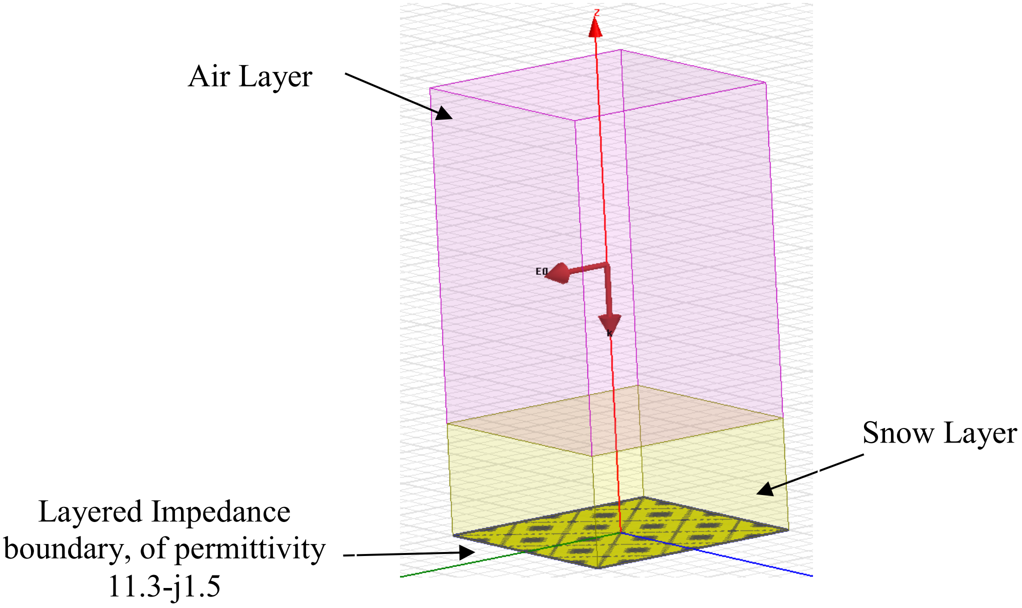
Air Layer

Snow Layer

Layered Impedance boundary, of permittivity 11.3-j1.5

Figure 1-9: Three-layered structure setup in HFSS.

1.8.2 HFSS Calculation Setup

Boundary conditions must be applied to the boundary faces of the structure. The boundary conditions used in this work are: "*perfectly matched layer (PML)*", "*layered impedance*", and "*master/slave*" as shown in Figure 1-10. The plane wave is the natural choice for satellite radar and radiometer applications. The incident angle of the beam and its polarization (H or V) must be defined. The direction of the electric field vector specifies the polarization of the antenna. The incident angle range was chosen to vary from 0° to 80°.

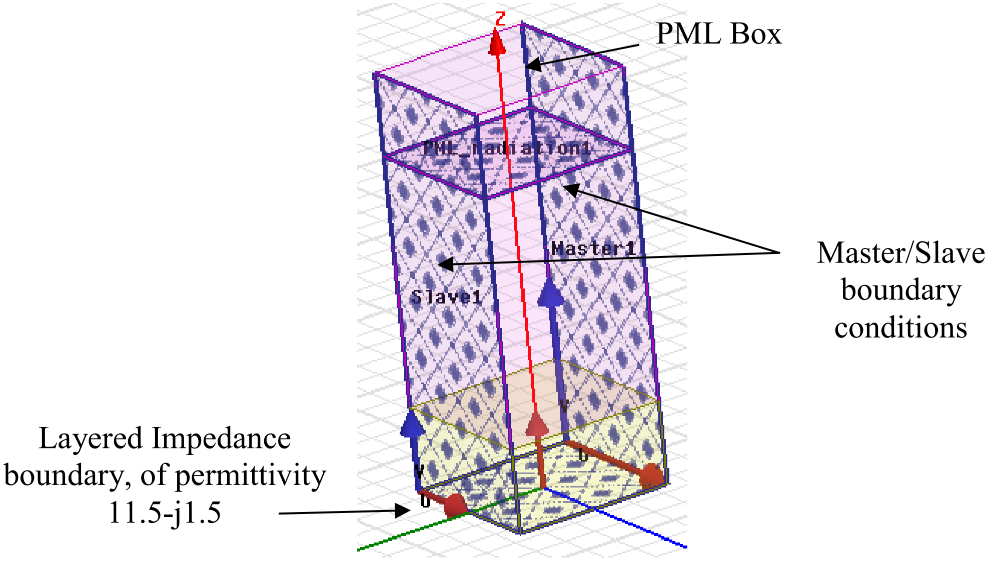

PML Box

Master/Slave boundary conditions

Layered Impedance boundary, of permittivity 11.5-j1.5

Figure 1-10: Boundary conditions used in the setup.

1.8.3 Analyzing Results Calculated by HFSS

The reflection coefficient is calculated using the field calculator in HFSS. Using this calculator, one can perform mathematical operations on any of the field quantities within the solution space to derive specialized quantities [16]. The net power flow through a surface is calculated by integrating the poynting vector normal to that surface. Cut-planes must be generated to represent the integration location and should be normal to both the incident and the scattered ray directions as shown in Figure 1-11. The cut-plane for magnitude integration data should not be too close to the very reactive near fields. Its root point was taken at 4 m over the reflection surface.

The calculator will be used to extract two quantities [17]:

- P_{inc}: incident power computed using incident field solutions as shown in Figure 1-11(a):

$$P_{inc} = \left| \int_S \frac{1}{2} (\mathrm{E}_{inc} \times \mathrm{H}_{inc}^*).dS \right| \tag{1.47}$$

- P_{ref}: reflected power computed using scattered field solutions as shown in Figure 1-11(b):

$$P_{ref} = \left| \int_S \frac{1}{2} (\mathrm{E}_{ref} \times \mathrm{H}_{ref}^*).dS \right| \tag{1.48}$$

These two quantities will then be used to compute the reflection coefficient:

$$\rho = (\mathrm{P}_{\mathrm{ref}} / \mathrm{P}_{\mathrm{inc}})^{1/2} \tag{1.49}$$

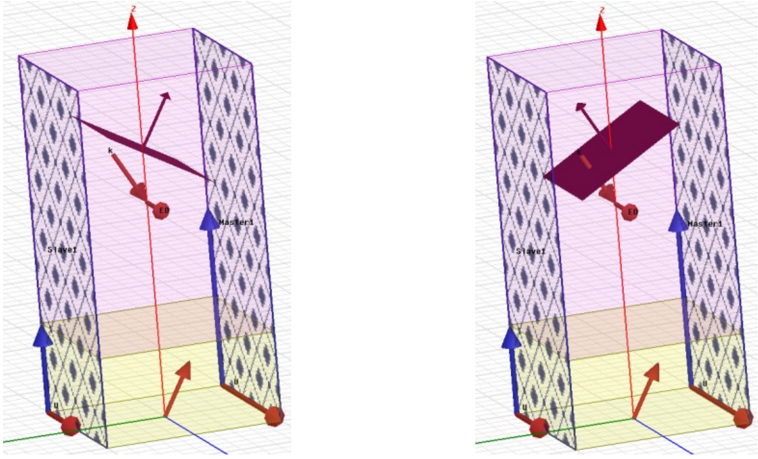

(a) (b)

Figure 1-11: (a) Diagram showing the model constructed for the calculation of the reflected power at an angle of incidence 30°. (b) Diagram showing the model constructed for the calculation of the incident power at an angle of incidence 30°.

Table 1-3: Bistatic Reflection Coefficient in Case of Horizontal and Vertical Polarizations for Air/Snow/Ground Three-Layered Model.

	Horizontal Polarization		**Vertical Polarization**	
Incidence Angle	$\|\rho_h\|_{HFSS}$	$\|\rho_h\|_{Theory}$	$\|\rho_v\|_{HFSS}$	$\|\rho_v\|_{Theory}$
0°	0.4699	0.4618	0.4699	0.4618
10°	0.4522	0.4495	0.4446	0.4421
20°	0.3984	0.4038	0.3763	0.3826
30°	0.3159	0.3131	0.3043	0.3078
40°	0.2971	0.2863	0.3006	0.3045
50°	0.5125	0.4948	0.3416	0.3461
60°	0.7064	0.6943	0.2936	0.3027
70°	0.8251	0.8081	0.095	0.1075
80°	0.9145	0.8948	0.2873	0.2793

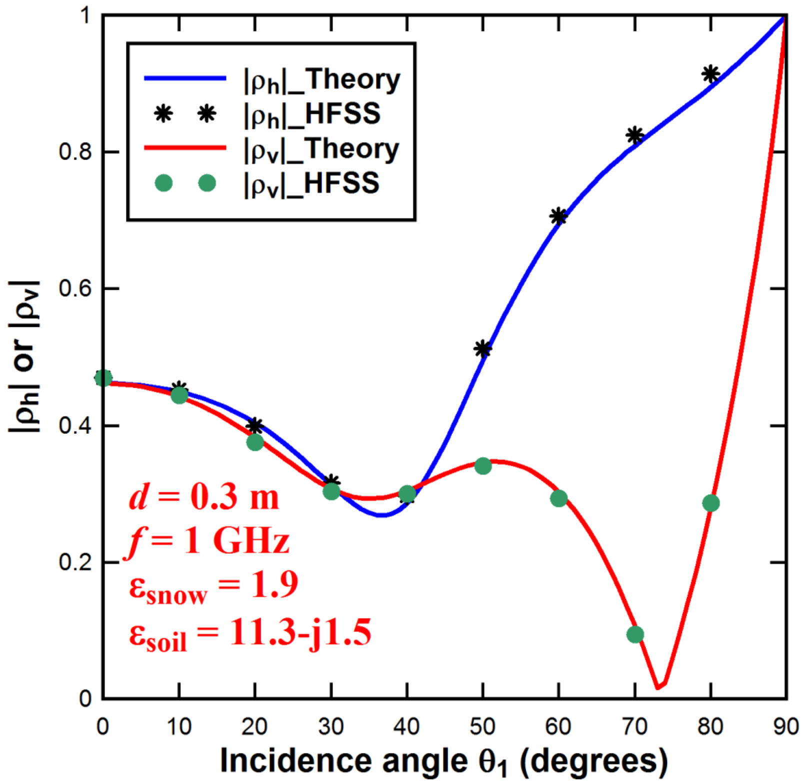

Figure 1-12: Plots for $|\rho_h|$ and $|\rho_v|$ as a function of incidence angle θ_1 for a 0.3 m snow layer over the ground.

Table 1-3 shows the calculated results (See Appendix A) using the previous procedure for horizontally and vertically polarized incident wave for a three-layered model of Air-Snow-Ground for a range of angle of incidence from 0° to 80°. The electrical properties of the layers are those summarized in Table 1-2 where the simulation is done for a depth of 0.3 m of snow.

The magnitude of the reflection coefficient ρ_h and ρ_v as a function of incidence angle for a 0.3 m snow layer over the ground is illustrated in Figure 1-12. As it can be seen from Figure 1-12, the calculated results of the reflection coefficient of the air-snow-ground system agree well with theoretical values in case of both a horizontally and vertically polarized incident wave. However, accuracy decreases for higher incidence angles and it can be compensated with more convergence if necessary.

1.9 CONCLUSION

In this chapter, the reflection coefficient of the air-snow-ground system was calculated using an electromagnetic simulator (HFSS) for both horizontally and vertically polarized incident waves. The results are in a well agreement with theoretical values. This reflection coefficient will be then used when calculating the backscattering coefficient in the presence of surface and volume scattering mechanisms since the backscattering coefficient is related to the to ρ_v and ρ_h of the surface.

Chapter 2: Effective Permittivity of Snow: Numerical Validation by the Finite Element Method

2.1 INTRODUCTION

In remote sensing applications, natural earth materials are often inhomogeneous and complicated in structure such as snow, sea ice, and soil. The concept of effective dielectric constant is an important tool in treating the interaction problem between electromagnetic waves and such complex materials. In theoretical microwave modelling of random media such as snow, the calculation of the effective permittivity is essential which describes propagation and attenuation. An accurate estimation of the effective permittivity of snow is important in recovering the snow depth from the reflected signal toward the radar. Of course, such a homogenization approach has limitations of which the user needs to be aware.

In this chapter, the effective permittivity of a fully 3-D mixture of snow is numerically calculated using the finite element method (FEM). In this work, the S-parameters will be extracted from HFSS. Then, the curve of the effective permittivity of snow is obtained from the transmission coefficient (S_{21}) which is related to the effective permittivity by a non-linear complex equation.

2.2 HISTORICAL BACKGROUND

Homogenization theories for dielectric properties have a long history. Significant studies regarding the dielectric permittivity of mixtures began in the 19th century by Mossotti [18], Clausius [19], Ludvig Valentin Lorenz [20, 21], Hendrik Antoon Lorenz [22], and Lord Rayleigh [23]. James Clerk Maxwell Garnett is a famous name that appears very commonly in present literatures related to dielectric mixing rules. Then, Dirk Anton George Bruggeman developed a new mixing approach that is qualitatively different from earlier homogenization principles.

The history of effective material properties in the context of electromagnetics has been told from several perspectives [24]. More detailed information about the historical developments of electromagnetic homogenization can be found in [25, 26].

Recent studies are interested in computational electromagnetics with efficient simulators to get a better understanding of heterogeneities. Numerical predictions for the electrical parameters of mixtures were done using the well-known Finite Difference (FD) method [27] and Finite Difference Time Domain (FDTD) method [28]. However, this chapter demonstrates an approach for solving numerically the characteristics of heterogeneous mixtures (dry and wet snow) by means of the Finite Element Method.

2.3 3-D DIELECTRIC MIXING RULES

Dielectric materials are such media that do not conduct electricity. A measure for their ability to store, not conduct, electrical energy is the permittivity or dielectric constant of the material. So, the permittivity is just an approximate to calculate the electric response of matter.

The concept of effective medium of an inhomogeneous material is to have an equivalent dielectric constant ε such that the mixture responds to an electromagnetic excitation as if it is homogeneous as shown in Figure 2-1. The mixing rules are often derived using static and quasi-static arguments assuming that the size of inclusions in the mixture is small with respect to the wavelength of the electromagnetic field that is used. However, the following estimate is often used: the size of an inclusion in the mixture must not exceed a tenth of the wavelength in the effective medium [24]. With such condition, the medium appears homogeneous to the wave. For remote sensing applications of snow, the wavelength of the signal is often much longer than the snow grain size which means that snow can act as a homogeneous dielectric layer with an effective permittivity.

The polarization is proportional to the electric field E for a linear isotropic dielectric material:

$$D = \varepsilon_0 E + P \tag{2.1}$$

$$P = \chi_e \varepsilon_0 E \tag{2.2}$$

where P is the response of matter to electric excitation. It is called the average polarization, the electric dipole moment density. χ_e is called the electric susceptibility and D is the flux density.

The permittivity ε is the relation between the flux density and the electric field:

$$D = \varepsilon E \tag{2.3}$$

Usually, a dimensionless parameter is used which is the relative permittivity ε':

$$\varepsilon = \varepsilon' \varepsilon_0 \tag{2.4}$$

$$\varepsilon' = 1 + \chi_e \tag{2.5}$$

Classical mixing rules for snow provides a scalar relation between D and E that is the isotropic case. Once the complex permittivity is known, it can be calculated how much the material attenuates electromagnetic waves that propagate through it [25]. The equivalent dielectric constant of a heterogeneous material (mixture) consisting of two or more substances is related to the dielectric constants of the individual substances, their volume fractions, their spatial distributions, and their orientations relative to the direction of the incident electric-field vector [25].

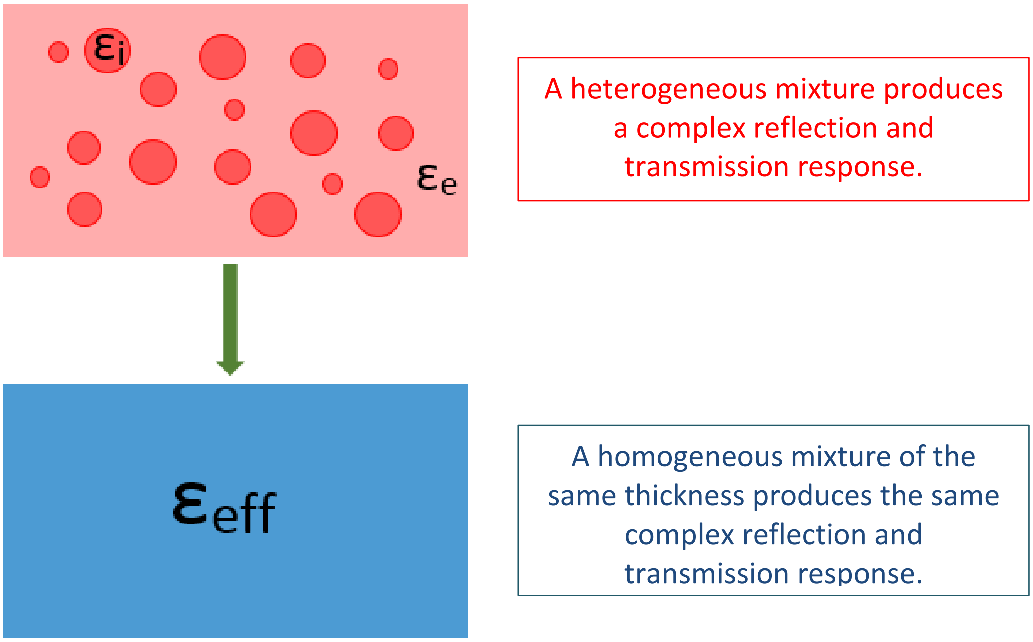

A heterogeneous mixture produces a complex reflection and transmission response.

A homogeneous mixture of the same thickness produces the same complex reflection and transmission response.

Figure 2-1: Effective medium approach.

2.3.1 Maxwell Garnett Formula

To begin with the simplest model for a dielectric mixture, isotropic dielectric spheres are embedded as inclusions (guest) in an isotropic dielectric environment (host). The dielectric relative permittivity of the background is ε_e and that of the guest is ε_i. The fraction volume occupied by the inclusions is v_i, and then the volume fraction left for the host is $(1- v_i)$. The effective permittivity (ε_{eff}) of the mixture is defined as the relation between the volume-average field and flux density:

$$\langle D \rangle = \varepsilon_{eff} \langle E \rangle \tag{2.6}$$

The average filed and flux density can be written by weighing the fields with the corresponding volume fractions [25]:

$$\langle D\rangle = f\varepsilon_i E_i + (1-f)\varepsilon_e E_e \tag{2.7}$$

$$\langle E\rangle = fE_i + (1-f)E_e \tag{2.8}$$

Then, the effective permittivity can be written as:

$$\varepsilon_{eff} = \frac{f\varepsilon_i A + (1-f)\varepsilon_e}{fA + (1-f)} \tag{2.9}$$

where A is the field ratio between the internal field and the external field: $E_i = A\ E_e$ and it is defined by: $A = 3\varepsilon_e / (\varepsilon_i + 2\varepsilon_e)$ [26]. So, the prediction of the effective permittivity of the mixture ε_{eff} according to the Maxwell-Garnett basic mixing rule reads [27-29]:

$$\varepsilon_{eff} = \varepsilon_e + 3v_i\varepsilon_e \frac{\varepsilon_i - \varepsilon_e}{\varepsilon_i + 2\varepsilon_e - v_i(\varepsilon_i - \varepsilon_e)} \tag{2.10}$$

where ε_e is the permittivity of the background, ε_i is the permittivity of the inclusions, ε_{eff} is the effective permittivity of the mixture, and v_i is the volume fraction of the inclusions. The Maxwell Garnett's formula is used in various fields of application. As $v_i \to 0$, $\varepsilon_{eff} \to \varepsilon_e$; however, as $v_i \to 1$, $\varepsilon_{eff} \to \varepsilon_i$. If the component phases are interchanged, that is a transformation is done by: $\varepsilon_i \to \varepsilon_e$, $\varepsilon_e \to \varepsilon_i$, $v_i \to 1 - v_i$, the effective permittivity will not be the same. So, Maxwell Garnett model is not symmetric.

2.3.2 Bruggeman Formula

Maxwell Garnett formula is inherently non-symmetric. So it is clear that the Maxwell Garnett model cannot remain the only mixing formula where its limitations are discussed in [25, Chapter 8]. Another famous mixing rule is the Bruggeman formula [27] based on the absolute equality between the phases in the mixture:

$$(1-v_i)\frac{\varepsilon_e - \varepsilon_{eff}}{\varepsilon_e + 2\varepsilon_{eff}} + v_i\frac{\varepsilon_i - \varepsilon_{eff}}{\varepsilon_i + 2\varepsilon_{eff}} = 0 \tag{2.11}$$

where spherical inclusions with volume fraction v_i are embedded in homogeneous background.

The Bruggeman rule is also known as the Polder–van Santen formula [27, 31] and de Loor formula in remote sensing science. Although this form is not explicit for the effective permittivity ε_{eff}, the Bruggeman formula has the appeal in the very property that it treats the inclusions and the environment symmetrically [25]. If the component phases are interchanged, that is a transformation is done by: $\varepsilon_i \to \varepsilon_e$, $\varepsilon_e \to \varepsilon_i$, $v_i \to 1 - v_i$, the effective permittivity will be the same. Bruggeman / Polder-van Santen formula has many applications on real-life materials especially geophysical media such as snow.

2.3.3 Coherent Potential Formula

One further formula which is relevant in the theoretical studies of wave propagation in random media is the so-called Coherent potential formula [20, 24]. It can be written in the form:

$$\varepsilon_{eff} = \varepsilon_e + v_i(\varepsilon_i - \varepsilon_e)\frac{3\varepsilon_{eff}}{3\varepsilon_{eff} + (1-v_i)(\varepsilon_i - \varepsilon_e)} \qquad (2.12)$$

2.3.4 Sihvola's Generalized Mixing Formula

The mixing approach presented in [25] collects dielectric mixing rules into one family. For a two-phase mixture such as dry snow with a homogenous background and spherical inclusions, the prediction of the effective permittivity according to Sihvola's generalized mixing formula is:

$$\frac{\varepsilon_{eff} - \varepsilon_e}{\varepsilon_{eff} + 2\varepsilon_e + \upsilon(\varepsilon_{eff} - \varepsilon_e)} = v_i \frac{\varepsilon_i - \varepsilon_e}{\varepsilon_i + 2\varepsilon_e + \upsilon(\varepsilon_{eff} - \varepsilon_e)} \qquad (2.13)$$

where υ is a dimensionless parameter. This general equation reduces to Maxwell Garnett formula when $\upsilon = 0$, Bruggeman formula when $\upsilon = 2$, and Coherent potential approximation when $\upsilon = 3$. For dilute mixtures ($v_i \ll 1$), all presented formulas predict the same results.

2.3.5 Multiphase Mixtures

Wet snow is a three phase mixture with two types of inclusions. So, the above dielectric mixing rule can be applied to dry snow only. Therefore, for multi-phase mixtures with spherical inclusions, Maxwell-Garnett formula and Bruggeman formula are (3.14) and (3.15) respectively [25]:

$$\frac{\varepsilon_{eff} - \varepsilon_e}{\varepsilon_{eff} + 2\varepsilon_e} = \sum_{k=1}^{K} v_k \frac{\varepsilon_k - \varepsilon_e}{\varepsilon_k + 2\varepsilon_e} \qquad (2.14)$$

$$\sum_{k=1}^{K} v_k \frac{\varepsilon_k - \varepsilon_{eff}}{\varepsilon_k + 2\varepsilon_{eff}} = 1 \qquad (2.15)$$

where v_k and ε_k are the fraction volume and the permittivity of the k-th phase respectively.

2.3.6 Effective Permittivity Limits

Different mixing models predict different effective permittivity values for a given dielectric mixture. However, there are theoretical bounds that limit the range of the predictions known as Wiener limits [32]. This is illustrated in Figure 2-2. The Wiener bounds give the maximum and minimum values for the effective permittivity defined as:

$$\varepsilon_{eff,\min} = \frac{\varepsilon_i \varepsilon_e}{f\varepsilon_e + (1-f)\varepsilon_i} \quad (2.16)$$

$$\varepsilon_{eff,\max} = f\varepsilon_i + (1-f)\varepsilon_e \quad (2.17)$$

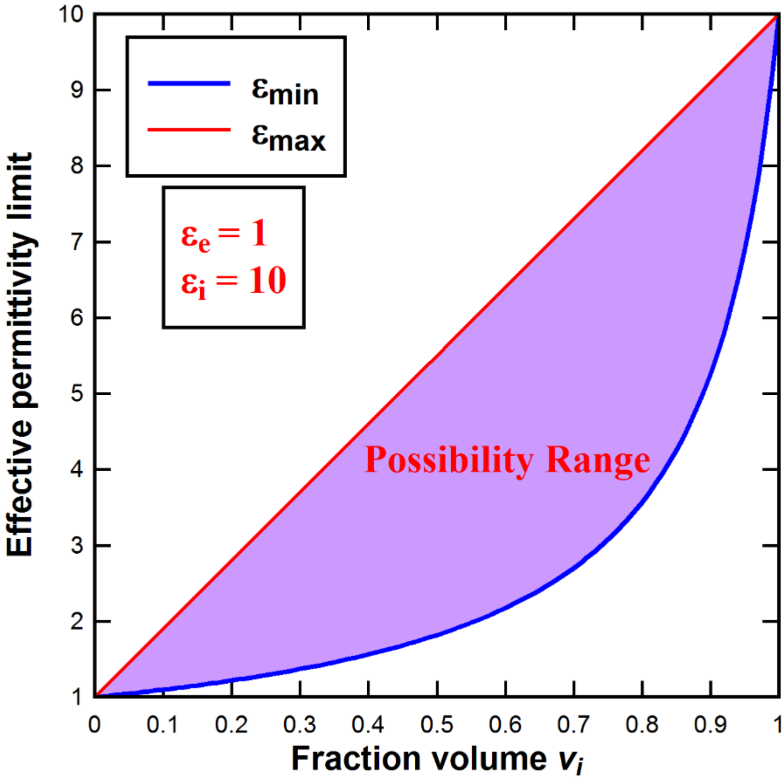

Figure 2-2: Wiener bounds for the relative effective permittivity of a mixture where ε_e =1 and ε_i =10.

2.4 DIELECTRIC CONSTANT OF SNOW

2.4.1 Permittivity of Dry Snow

Dry snow is a two-phase mixture consisting of ice particles embedded in an air background. The ice inclusions in natural snow usually have a diameter of 0.1-2 mm [33], so the quasi-static assumption can be valid throughout the microwave range of dry snow. The dielectric constant of dry snow ($\varepsilon_{ds} = \varepsilon_{ds}' - j\varepsilon_{ds}''$) depends on the permittivity of air (ε_{air}), the permittivity of ice ($\varepsilon_i = \varepsilon_i' - j\varepsilon_i''$), and the volume fraction of ice v_i. The volume fraction of ice v_i in snow is related to the snow density by:

$$v_i = \frac{\rho_s}{0.9167} \quad (2.18)$$

where 0.9167 g/cm^3 is the density of ice.

The real part of the permittivity of ice ε_i' is independent of frequency from 10 MHz to 300 GHz, and it exhibits a slight temperature dependence of the form [34]:

$$\varepsilon_i' = 3.1884 + 9.1\times 10^{-4} T \quad (-40°\mathrm{C} \le T \le 0) \tag{2.19}$$

where T is the temperature in °C. Ice is a low-loss material where its dielectric loss tangent is in the order of 10^{-4} (very low). The temperature sensitivity to ε_i' is very small and can be neglected; hence, the dielectric constant of dry snow ε_{ds}' is also independent of temperature and frequency in the microwave region. Applying Polder-Van Santen (PVS) model to dry snow where air is the background medium and ice spheres are in the inclusions give:

$$\frac{\varepsilon_{ds} - 1}{3\varepsilon_{ds}} = \frac{v_i(\varepsilon_i - 1)}{(\varepsilon_i + 2\varepsilon_{ds})} \tag{2.20}$$

This formula is a very important mixing rule in the remote sensing community. In the above equation, ε_{ds} and ε_i are complex quantities, but since $\varepsilon_i''/\varepsilon_i' \ll 1$, the imaginary parts of ε_{ds} and ε_i may be neglected when seeking and expressions for ε_{ds}'.

Another mixing formula for ice spheres in an air background is the Tinga-Voss-Blossey (TVB) two-phase formula which provides a good fit to the experimental data shown in [5].

$$\varepsilon_{ds} = 1 + \frac{3v_i(\varepsilon_i - 1)}{(2 + \varepsilon_i) - v_i(\varepsilon_i - 1)} \tag{2.21}$$

The advantage of Tinga model is that it does not have ε_{ds} on both sides of the equation.

Moreover, an equally good fit to the data is provided by the empirical expression (Matzler) [7, 35]:

$$\varepsilon'_{ds} = \begin{cases} 1 + 1.4667v_i + 1.435v_i^3 & for\ 0 \le v_i \le 0.45 \\ (1 + 0.4759v_i)^3 & for\ v_i \ge 0.45 \end{cases} \tag{2.22}$$

Unlike ε_{ds}', the loss factor of dry snow ε_{ds}'' is strongly dependent of both temperature and frequency having the same frequency and temperature behavior of ε_i''. Its expression is defined as in [7]. The dielectric properties of ice are summarized well in [34].

$$\varepsilon''_{ds} = \frac{0.34v_i\varepsilon''_i}{(1 - 0.42v_i)^2} \tag{2.23}$$

The applicability of the previous equations is limited to frequencies below about 15 GHz since these equations assume that the scattering losses in the snow medium are negligible in comparison to the absorption losses. Figure 2-3 and Figure 2-4 show a plot for the dry snow's permittivity and loss factor using the previous models as a function of dry snow density.

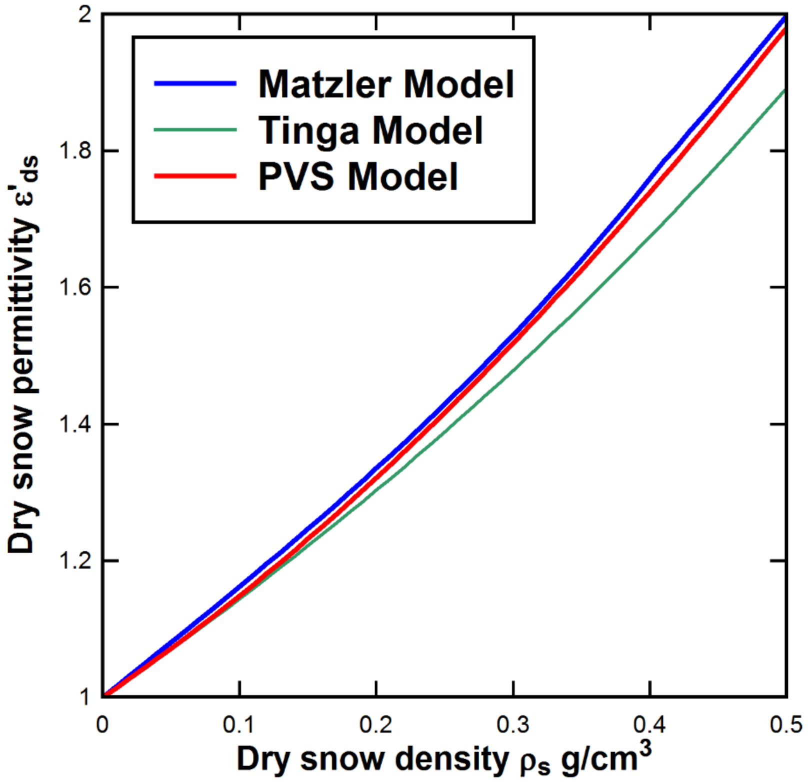

Figure 2-3: Permittivity of dry snow as a function of snow density.

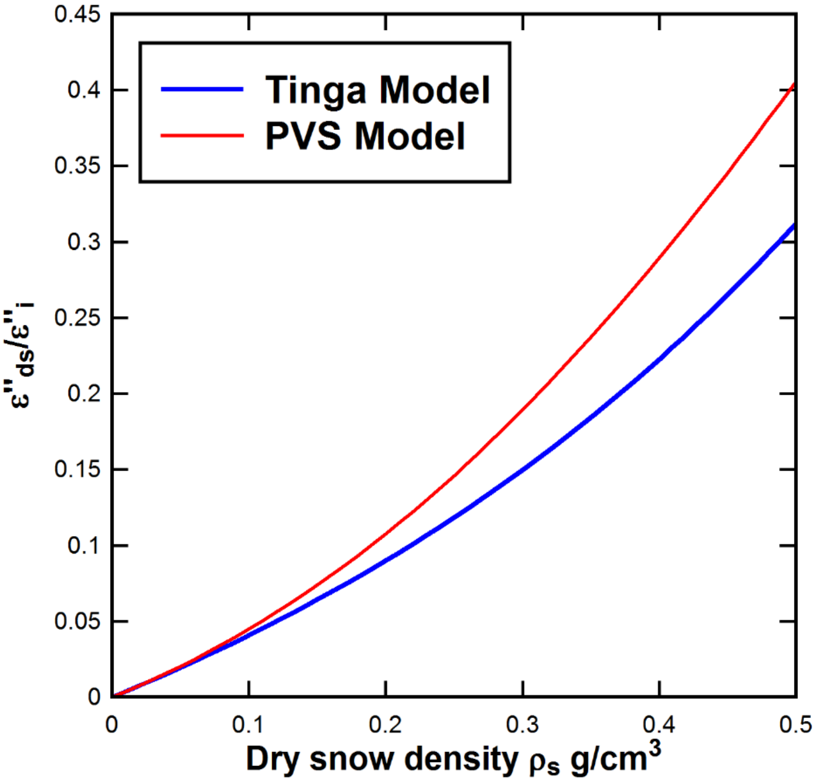

Figure 2-4: Loss factor of dry snow relative to that of ice as function of snow density.

2.4.2 Permittivity of Wet Snow

Electromagnetically, wet snow is a three-component dielectric mixture consisting of ice particles, air, and liquid water. Both ice and water exhibit dispersion spectra; however, the relaxation frequency of ice is in the kilohertz range, whereas that for water at 0°C is about 9 GHz [5]. Consequently, the dielectric constant of wet snow is in general a function of frequency, temperature, volumetric water content, snow density, ice and water inclusions shapes. Because of the high dielectric constant of liquid water compared to that of air and ice, the spectral behavior of the wet snow mixture is likely to be dominated by the dispersion behavior of water [5]. The modified Debye-like model is a simple empirical formula used to calculate the effective permittivity of wet snow.

$$\varepsilon_{ws}^{'} = A + \frac{Bm_v^x}{1+(f/f_0)^2} \tag{2.23}$$

$$\varepsilon_{ws}^{''} = \frac{C(f/f_0)m_v^x}{1+(f/f_0)^2} \tag{2.24}$$

where f_0 is the relaxation frequency, f is in GHz, m_v is the liquid water-content in % and:

$$A = 1.0 + 1.83\rho_{ds} + 0.02A_1 m_v^{1.015} + B_1$$
$$B = 0.0731A_1$$
$$C = 0.073A_2$$
$$x = 1.31$$
$$f_o = 9.07\ GHz$$
$$A_1 = 0.78 + 0.03f - 0.58\times10^{-3}f^2$$
$$A_2 = 0.97 - 0.39f\times10^{-2} + 0.39\times10^{-3}f^2$$
$$B_1 = 0.31 - 0.05f + 0.87\times10^{-3}f^2$$

For frequencies below 15 GHz, $A_1 = A_2 = 1$ and $B_1 = 0$. Typical liquid water content found in snow ranges between $m_v = 0$ % to $m_v = 12$ %. The curves shown in Figure 2-5 and Figure 2-6 were calculated using the modified Debye-like equations (2.23) and (2.24). The effect of liquid water content on the dielectric behavior of wet snow is well observed between 1 and 30 GHz. As said before, the relaxation frequency of water is 9 GHz and this is observed clearly from Figure 2-6 where the maximum value of ε''_{ws} is reached at 9 GHz. As the absorption losses increase strongly with increasing liquid water content, the penetration depth decreases strongly with increasing liquid water content. So, under wet conditions, extraction of snow depth is somehow not possible for high values of snow wetness.

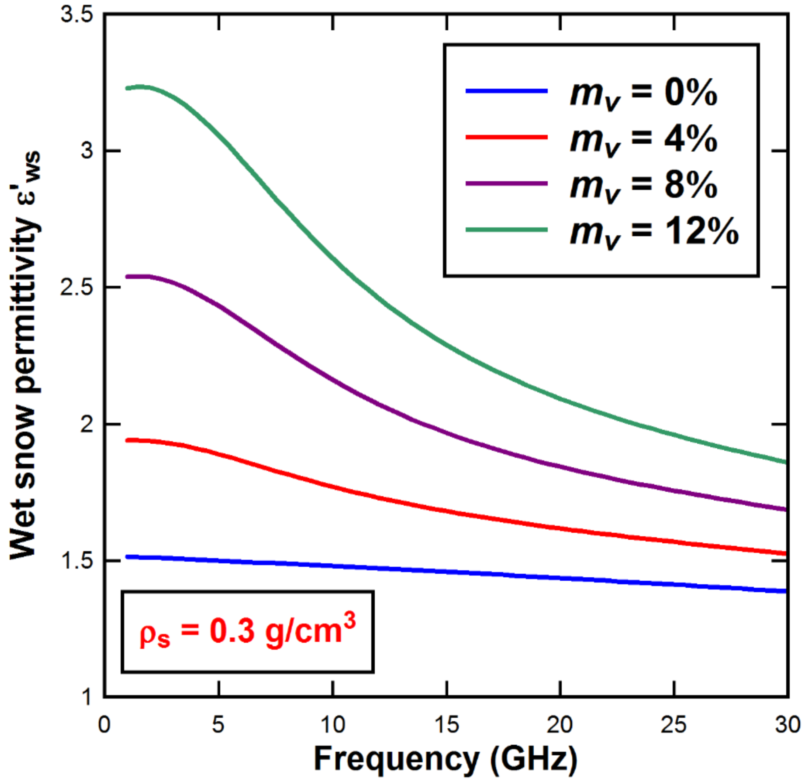

Figure 2-5: Spectral variation of the permittivity of wet snow with snow wetness.

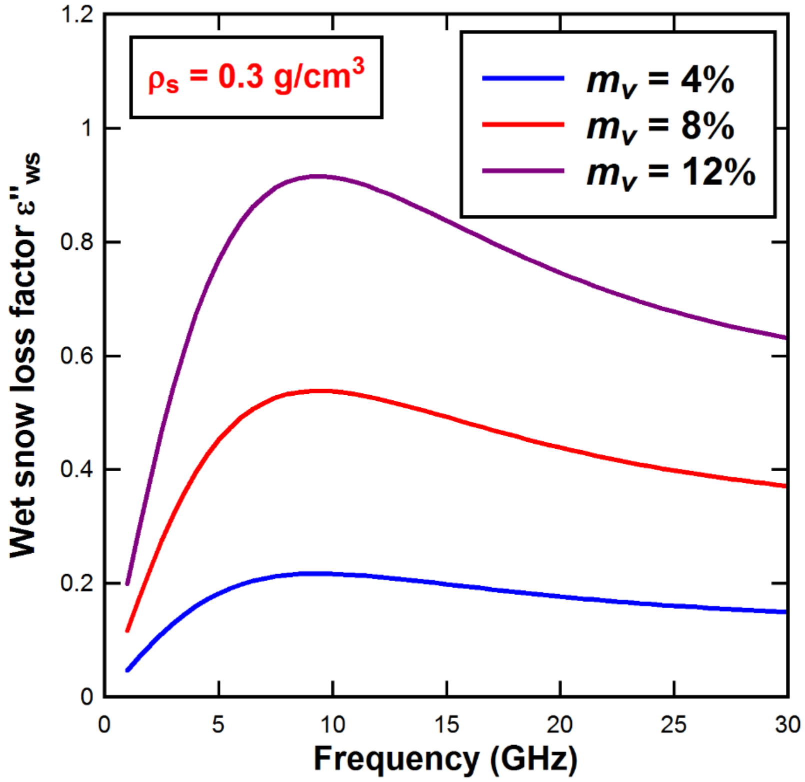

Figure 2-6: Spectral variation of the loss factor of wet snow with snow wetness.

2.5 NUMERICAL STUDY OF THE EFFECTIVE PERMITTIVITY OF SNOW

The history of the study of heterogeneous mixtures dates back to the 19th century, and several empirical and analytical models for the effective properties of mixtures have been proposed [28]. This section is intended to solve the direct problem in effective permittivity calculations of composite systems such as snow by means of the well-known electromagnetic simulator (Ansoft HFSS). This FEM solver is able to calculate the S-parameters of the simulated structure from which we can calculate the effective permittivity. However, FEM has not been applied in any way for solving properties of dielectric mixtures.

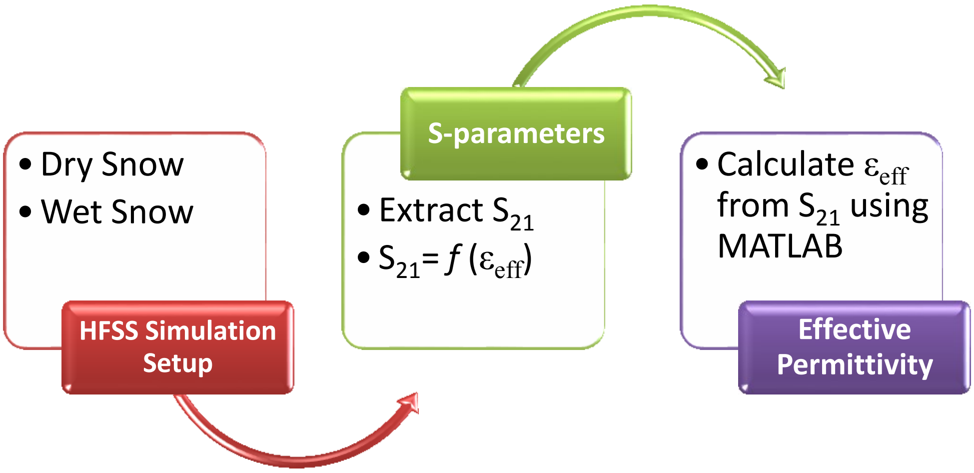

Figure 2-7: Flow chart of the numerical simulation used in the effective permittivity calculation.

In order to evaluate the reliability of the proposed solver, numerical results have been compared with theoretical dielectric mixing models and they show a moderate agreement with the Bruggeman rule rather than the Maxwell Garnett approach. The steps required in the effective permittivity calculation are summarized in a flow chart in Figure 2-7.

2.5.1 Dry Snow HFSS Setup

Ice is a low-loss material where its dielectric loss tangent is in the order of 10^{-4} (very low). To decrease the computation time and the used memory in the simulation, its value was taken to be zero so that no significant effect on the results.

The simulation setup of dry snow can be seen in Figure 2-8. It is a cubic background of air of length a = 100 mm and permittivity 1 ($\varepsilon_e = 1$) in which spherical ice inclusions ($\varepsilon_i' = 3.185$ and dielectric loss tangent = 0) are embedded in random positions occupying a volume fraction v_i. Periodic boundary conditions were chosen because infinitely random mixtures cannot be modelled. PEC (Perfect Electric Conductor) boundary conditions are assigned to the upper and lower surfaces of the structure in the z-direction as shown in Figure 2-8(a) while PMC (Perfect Magnetic Conductor) boundaries in the y-direction as shown in Figure 2-8(b). The simulated fraction volume of ice varies from 0.01 to 0.5 because the density of dry snow is mostly below 0.5g/cm^3. The combination of PE-PM boundary conditions is just to realize a periodic infinite structure of snow.

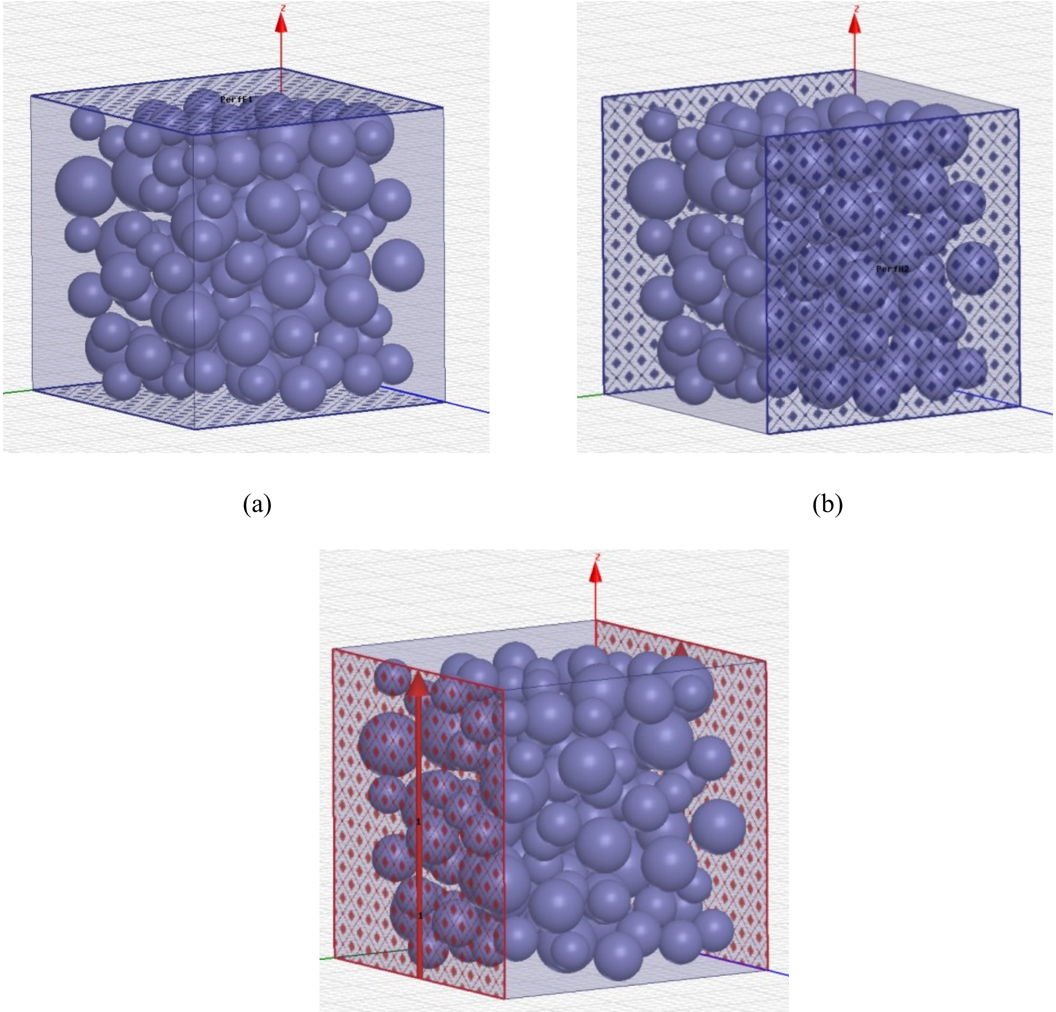

(a) (b)

(c)

Figure 2-8: Schematics of the simulation setup. (a) The simulation model of dry snow with perfect electric boundary conditions. (b) The simulation model of dry snow with perfect magnetic boundary conditions. (c) The structure's excitation: Wave Port.

This setup is done for about 100 simulations of dry snow structure. In every simulation, the fraction volume and the positioning of inclusions were randomly chosen. A MATLAB script is used to find the coordinates and the radii of a certain number of spheres inside a cube of 100 mm length to make sure that the drawn sphere is inside the cubic air background. Then, an HFSS script is written to import these spherical inclusions into HFSS (See Appendix B). Simulation is done for overlapped and non-overlapped spherical inclusions with a non-uniform size distribution respecting the quasi-static limit. Allowing spherical inclusions to overlap means that complex geometries can be formed.

The geometry is then terminated and excited by two wave ports which compute the S-parameters as shown in Figure 2-8(c). Once the boundary conditions and excitations are properly assigned to the structure, we need to add the analysis setup and choose an appropriate solution frequency. An operating frequency is chosen in the spectrum of frequencies [2-8] GHz which is capable of penetrating a deep snow layer. In this study, the operating frequency is 2 GHz. Since the size of the particles are small compared to the wavelength, only one polarization need to be considered.

2.5.2 Wet Snow HFSS Setup

Wet snow is a three-phase mixture of air, ice, and water. Debye model is assigned for the permittivity of water used in the wet snow simulation setup and imported into HFSS. Water inclusions have a permittivity which is about 40 times than that of dry snow. That's why the spectral behaviour of wet snow is strongly affected by the spectral behaviour of water.

Table 2-1: Input parameters for wet snow sample.

Operating frequency	2 GHz
Permittivity of water at 2 GHz	84.26
Dielectric loss tangent of water at 2 GHz	0.212
Liquid water content range	1.6% to 12.5%
Permittivity of Ice at T ≈ 4°C	3.185
Dielectric loss tangent of Ice	$\sim 10^{-4}$

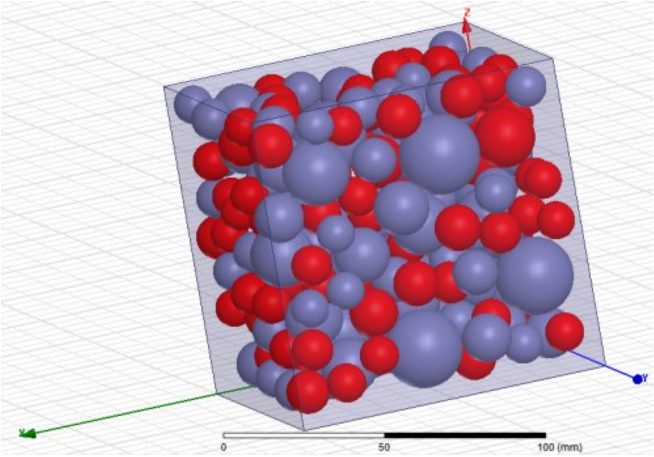

Figure 2-9: Wet snow mixture sample with ~12% liquid water content.

The simulation setup of wet snow is the same as that for dry snow but with ice (gray spheres) and water (red spheres) spherical inclusions as shown in Figure 2-9. In this study, the wet snow samples represent an upper limit of liquid water content ($m_v = 12\%$) and a lower limit ($m_v = 1.6\%$). Table 2-1 summarizes all input parameters to the wet snow structure.

2.6 RETRIEVAL METHOD

The inverse problem regarding the retrieval of the constitutive parameters of various complex materials is a classic issue, and has been extensively studied with both theoretical and experimental efforts [36]. Although different measurement systems are employed in various experimental approaches [37, 38], most of them aim at measuring the reflection and transmission data, from which the effective medium parameters can be retrieved [36]. This so-called S-parameter retrieval method was originally proposed by Nicolson and Ross in 1970. More importantly, if the composites are assumed nonmagnetic and treated effectively homogenous, the effective permittivity can then be analyzed using both S parameters, either one of them, or only some special reflection data [39].

In this work, the S_{21} retrieval method is used since snow is treated as a non-magnetic dielectric mixture where we can assume that $\mu_{eff} = 1$. Then, for a plane wave normally incident on a homogeneous slab with thickness d, the S_{21} parameter can be expressed as follows:

$$\mu_{eff} = 1 \quad and \quad n = \sqrt{\varepsilon_{eff}} \tag{2.25}$$

$$S_{21} = \frac{(1-R^2)e^{-j\sqrt{\varepsilon_{eff}}k_0 d}}{1-R^2 e^{-j2\sqrt{\varepsilon_{eff}}k_0 d}} \tag{2.26}$$

$$R = (1-\sqrt{\varepsilon_{eff}})/(1+\sqrt{\varepsilon_{eff}}) \tag{2.27}$$

where k_0 denotes the free space wave number. Note that (2.27) is just a function containing one variable ε_{eff}.

Once the S parameters are computed, the effective permittivity can be calculated by solving (2.27). This non-linear complex equation can be solved by separating the equation into real and imaginary parts, and then solve a system of two non-linear real equations by the help of MATLAB using the function fsolve. This procedure will be done for different values of volume fraction with hundreds of data points at $f = 2$ GHz and then a comparison is done with dielectric mixing rules.

2.7 RESULTS AND DISCUSSION

2.7.1 Effective Permittivity of Dry Snow

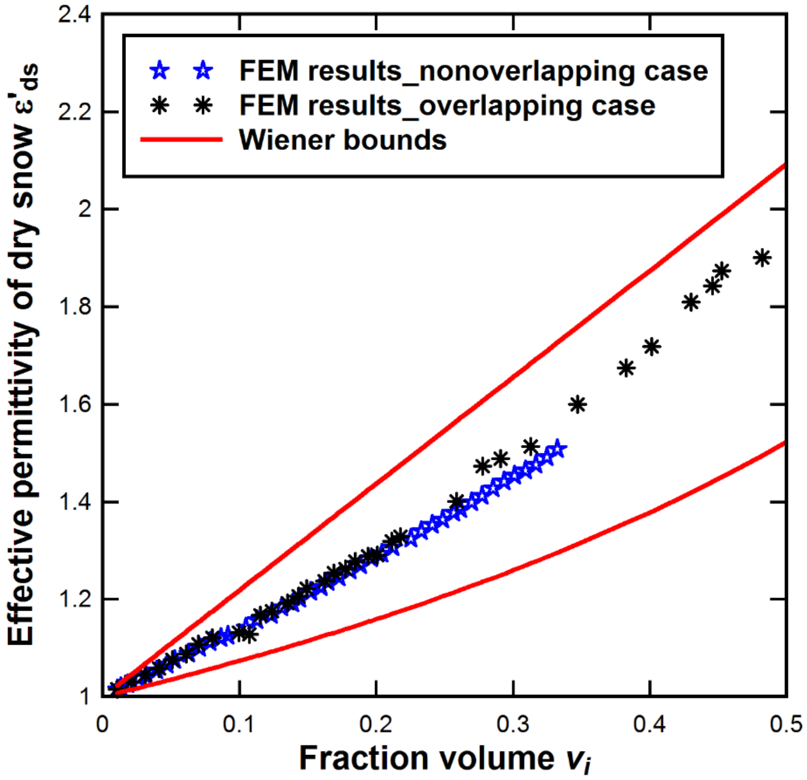

Figure 2-10: Effective permittivity of dry snow compared with theoretical bounds.

The effective permittivity for dry snow was studied for a range of the fraction volume of ice from 0 to 0.5. Figure 2-10 shows the effective permittivities achieved from 100 simulations from the FEM simulator for different volume fractions and positioning of inclusions. It is shown that the calculated permittivities are distributed in the area between the Wiener bounds. No sample falls outside those theoretical limits. Each mixture has its own effective permittivity which may differ from another mixture having the same volume fraction of ice because of their different microstructure. The calculated permittivity distribution is also compared with the two most famous theoretical mixing models: Maxwell Garnett and Bruggeman symmetric as shown in Figure 2-11. It is shown that in the case of overlapped inclusions, the Bruggeman model is more acceptable. However, if the inclusions in the mixture are non-overlapped, the results are closer to the Maxwell–Garnett model. Furthermore, the numerical results regarding the effective permittivity of dry snow are compared with dry snow permittivity models. It is shown from Figure 2-12 that Looyenga's model best fits the FEM simulated results in both cases: overlapped and non-overlapped inclusions. That's why Looyenga's model will be used in the snow density estimation method.

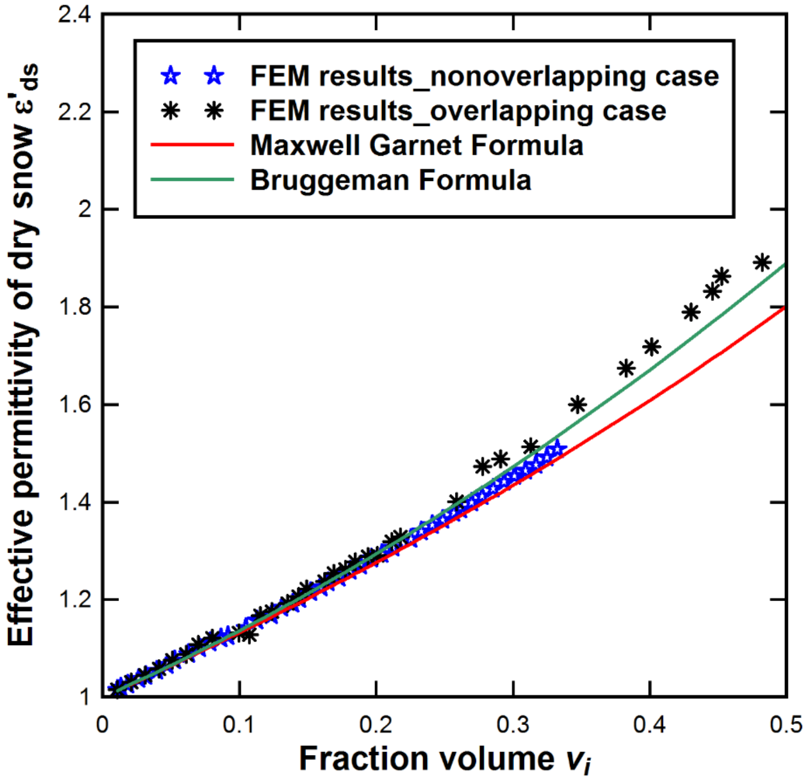

Figure 2-11: The calculated effective permittivity of dry snow compared with general theoretical models.

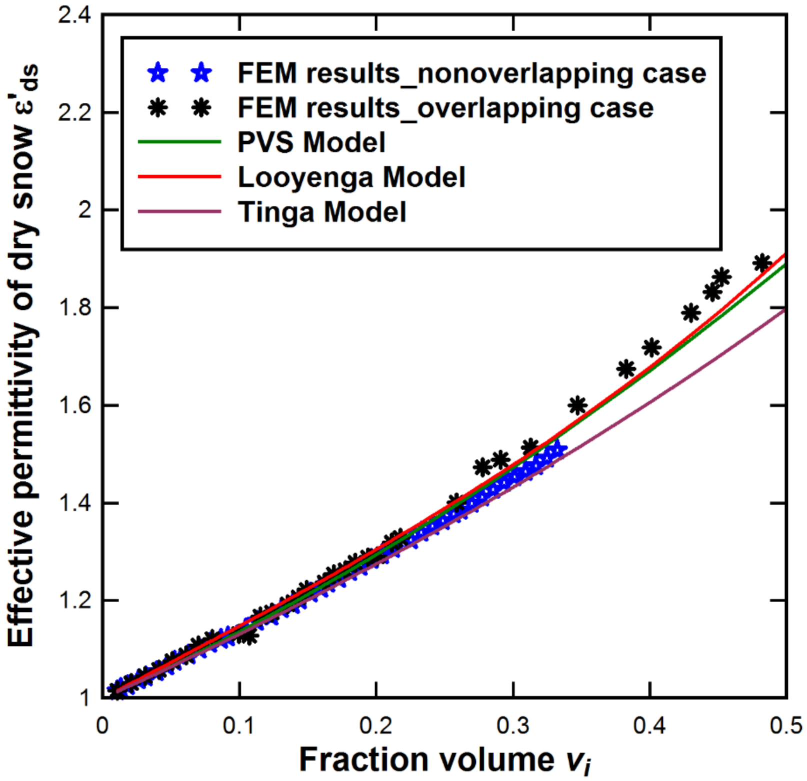

Figure 2-12: The calculated effective permittivity of dry snow compared with general dry snow permittivity models.

2.7.2 Effective Permittivity of Wet Snow

The effective permittivity for wet snow was studied for a range of liquid water content from 0% to 12.5%. Figure 2-13 shows the effective permittivities achieved from 100 simulations for different liquid content of water.

In microwave studies of snow, Polder-Van Santen model is often used. So, the calculated permittivity is compared to Polder-Van Santen model for a case of three-phase mixture since wet snow contains two types of inclusions. It is shown that the simulation results seem close to three-phase Polder-Van Santen model especially when the liquid water content increases (above 6%).

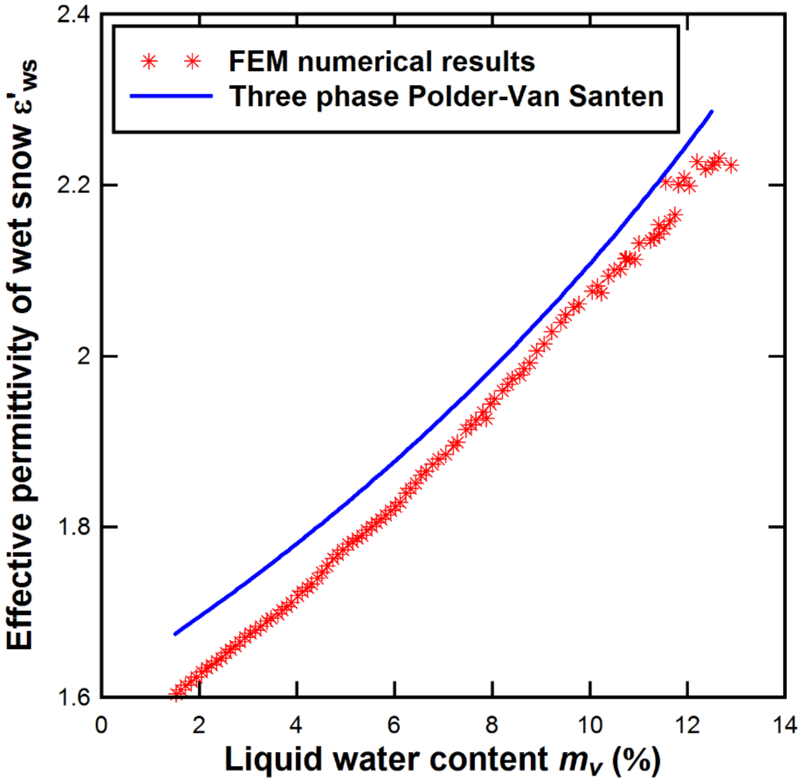

Figure 2-13: Effective permittivity of wet snow compared with the general theoretical model (Polder-Van Santen model).

2.8 CONCLUSION

In this chapter, hundreds of FEM simulations were done to test the FEM algorithm in finding the characteristics of a random dielectric mixture especially snow. No mixing model is able to predict the simulated results for the whole range of volume fraction. For dry snow, Looyenga's model is closer to the simulations when clustering is allowed. So, Looyenga's model will be used to relate the effective permittivity of snow with its density in the snow density estimation process in Chapter 4. For wet snow, a comparison was done with three-phase mixing rule and Polder-Van Santen was quite reasonable.

Chapter 3: Multilayer Numerical Model of Radar Backscattering from Air/ Snow/Ground System Based on the Finite Element Method

3.1 INTRODUCTION

It has been demonstrated that snow physical properties can be retrieved using active microwave sensors. This requires an understanding of how electromagnetic waves are scattered by point and distributed targets. The backscattered signal intercepted by a radar is a result of either surface scattering, volume scattering, or combination of both. Surface scattering occurs at a rough interface between two different dielectric media (snow-ground); however, volume scattering is caused by scatterers that are present in a homogeneous background (air).

The objective of this chapter is to study surface scattering phenomena in homogeneous layered media (air-snow-ground) with rough interfaces and volume scattering phenomena in case of heterogeneous snow mixture. This work is intended to solve the scattering calculations by means of the well-known electromagnetic simulator Ansoft's HFSS. For the first part, the goal is to illustrate the backscattering behavior of multi-layered homogeneous structure with non-planar interfaces; each layer with its own effective permittivity. Calculations were done for different incidence angles at frequency $f = 3$ GHz where the effect of the volume scatterers is neglected. Numerical results have been compared with theoretical models and they show a good agreement with the I^2EM model rather than the PRISM and SMART models. For the second part, the study is extended to treat snow as a heterogeneous mixture of air and ice to model the effect of volume scatterers in the snow volume which has a great impact on snow depth retrieval. The calculated backscattering coefficient at 9 GHz shows an excellent agreement with the S^2RT/R model where the volume contributions have a significant effect on the total backscatter.

3.2 RADAR SCATTERING

3.2.1 Radar Basics

The term RADAR is the contraction of the words: **Ra**dio **D**etection **a**nd **R**anging, i.e. finding and positioning a target and determining the distance between the target and the source by using a radio frequency [40]. Fundamentally, a radar is a system that uses electromagnetic radiation to detect the target's presence and determine its direction, distance, velocity, and radar scattering cross section. The scenario shown in Figure 3-1(a) is the case of a bistatic radar where the transmitter and receiver are separately located. In the monostatic radar configuration, the same antenna is used for both transmission and reception as shown in Figure 3-1(b). Due to different characteristics and applications, remote sensors can be divided into two categories: passive, known as radiometers, and active, known as radars as shown in Figure 3-2. Unlike radars, radiometers observe thermal emission radiated by the target. Active remote sensing is based on the theory of electromagnetism especially scattering; however, passive remote sensing is based on radiation theory.

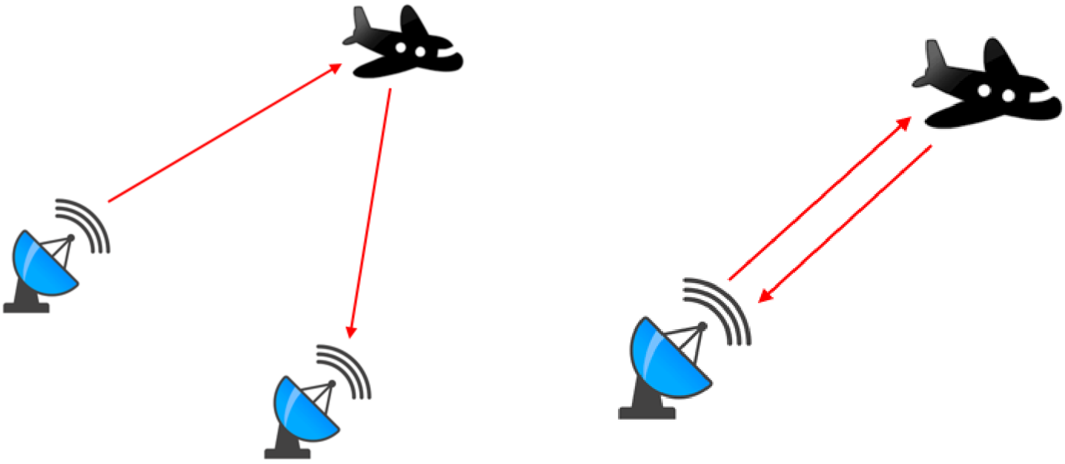

(a) (b)

Figure 3-1: (a) Monostatic radar (b) Bistatic radar.

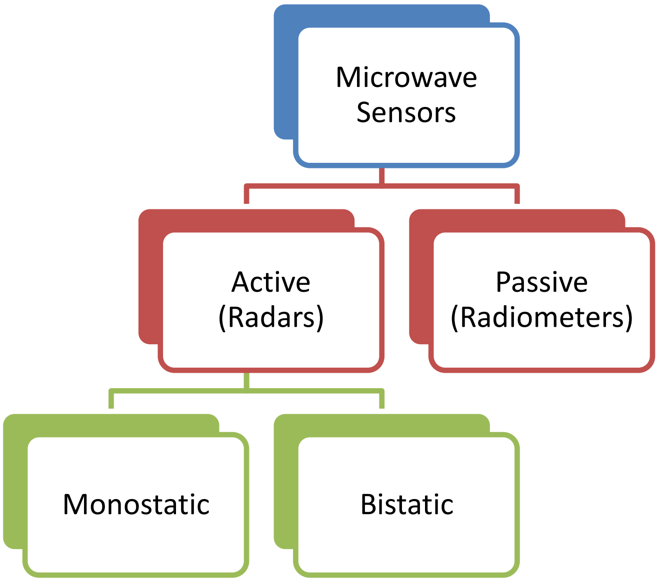

Figure 3-2: Microwave remote sensor classes.

3.2.2 Scattering Matrix

When modeling radar scattering from the earth's surface, it is more convenient to represent the earth's surface by the x-y plane and to represent the polarization vector E of waves incident upon or scattered from the surface in terms of the spherical angles θ and ϕ [7]. For a plane electromagnetic wave traveling in the k direction, its electric filed phasor E consists of a horizontal polarization component and a vertical polarization component:

$$E = (\hat{\ } \;\text{[illegible]}\;)e^{-jkk.R} \tag{3.1}$$

where $e^{-jkk.R}$ is the propagation phase factor. Scattering calculations involve four angles as illustrated in Figure 3-3:

- θ_i = incidence angle.
- θ_s = scattering angle.
- ϕ_i = azimuth angle.
- ϕ_s = azimuth angle.

The backscattering direction corresponds to $\theta_i = \theta_s$ and $\phi_s = \phi_i + \pi$.

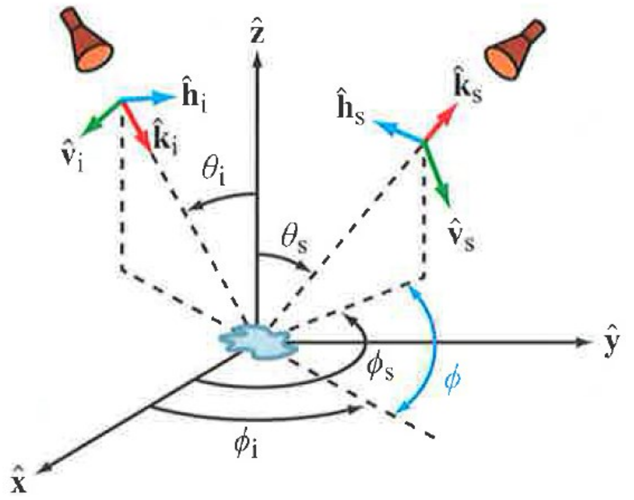

Figure 3-3: Scattering coordinate system [7].

The incident and the scattered wave may have both horizontal and vertical polarization components. So, the two fields are related by:

$$\begin{bmatrix} E_v^s \\ E_h^s \end{bmatrix} = (\frac{e^{-jkR_r}}{R_r}) \begin{bmatrix} S_{vv} & S_{vh} \\ S_{hv} & S_{hh} \end{bmatrix} \begin{bmatrix} E_v^i \\ E_h^i \end{bmatrix} \tag{3.2}$$

Where S_{pq} is called the scattering amplitude of the target where p and q may each be either v or h. The four scattering amplitudes characterizes the scattering behavior of the object for the four possible combinations of the v and h polarization orientations of the incident and scattered fields [41].

3.2.3 Radar Equation

The radar equation summarizes a relation between the characteristics of the radar, target, and the received signal. It is defined by:

$$\frac{P_p^r}{P_q^t} = \frac{G_t G_r \lambda^2}{(4\pi)^3 R_t^2 R_r^2} \sigma_{pq} \tag{3.3}$$

where P^r is the received power with polarization *p*, P^t is the transmitted power with polarization *q*, G_t is the gain of the transmit antenna in the direction of the target, G_r is the receive antenna gain, R_r is the range between the target and the receiver, R_t is the range between the target and transmitter, and σ_{pq} is the pq-polarized radar cross section (RCS).

In microwave remote sensing, the differential backscattering coefficient or radar reflectivity σ^0 is the main parameter of interest. It is defined by the average value of the radar cross section of the distributed target normalized with respect to the illumination area A of the antenna beam.

$$\sigma_{pq}^0 = \left\langle \frac{\sigma_{pq}}{A} \right\rangle \tag{3.4}$$

3.2.4 Bistatic Scattering Coefficient

In Chapter 2, we examined the Fresnel reflectivity of a three-layered media with perfectly flat surfaces where only a coherent component exists in the scattering pattern along the specular direction as shown in Figure 3-4(a). However, for a rough surface, the bistatic scattering coefficient contains a coherent component in the specular direction and non-coherent components in other directions as illustrated in Figure 3-4(b). It is defined by:

$$\sigma_{pq}^0 = \left(\frac{4\pi R_r^2}{A}\right) \frac{S_p^s}{S_q^i} \tag{3.5}$$

where S^s is the power density of the scattered wave and S^i is the power density of the incident wave. In electromagnetism, the degree of the surface roughness is defined by a parameter measured relative to the wavelength λ which is the electromagnetic roughness *ks* [7].

$$ks = \frac{2\pi}{\lambda} s \tag{3.6}$$

where *s* is the rms height of the surface.

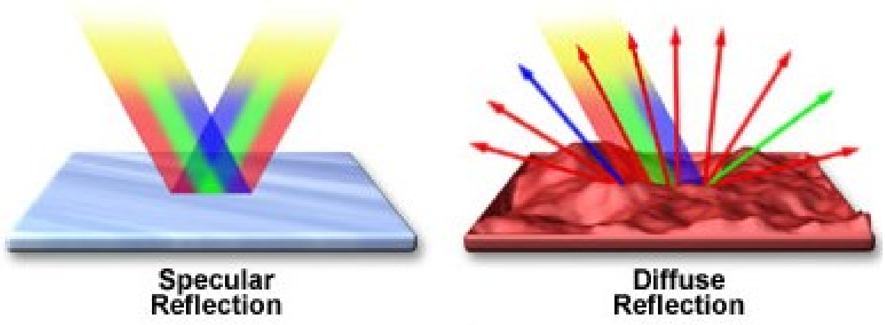

(a) (b)

Figure 3-4: (a) Specular Reflection (b) Diffuse Reflection [42].

For a slightly rough surface, *ks* is on the order of 0.1. However, for *ks* > 2, the surface is said to be very rough where the coherent component is negligible compared with the non-coherent components. Furthermore, the incoherent component contains not only waves with the same polarization as that of the incident wave, but also waves with the orthogonal polarization [7]. Roughness information about the interface is used to determine the scattering return. Surfaces of increasing roughness will tend to decrease the receive power as the signal is scattered over a wide range of angles [43]. Beckmann and Spizzichino [44] differentiate between a smooth and rough surface as follows: "*a surface will scatter energy of an incident plane wave into various directions, whereas a surface that reflects in a specular manner will be called smooth*."

In general, the total co-polarized bistatic-scattering coefficient σ^0_{pp} is composed of a coherent component $\sigma^0_{pp\text{-}coh}$ and an incoherent one $\sigma^0_{pp\text{-}inc}$ where the coherent component exists only along the specular direction. The cross-polarized component does not have a coherent component.

$$\sigma^0_{pp}(\theta_i,\phi_i;\theta_s,\phi_s)=\sigma^0_{pp-coh}(\theta_i)+\sigma^0_{pp-inc}(\theta_i,\phi_i;\theta_s,\phi_s) \tag{3.7}$$

3.2.5 Smooth Surface Criteria

Depending on the nature of the surface roughness, the interaction of the radar signal will be affected by the rms height and the correlation length of the surface relative to the wavelength of the electromagnetic radiation.

The Rayleigh roughness criteria states that the surface may be considered smooth if there is a phase difference of less than π/2 between two reflected rays. This corresponds to:

$$s<\frac{\lambda}{8\cos\theta_i} \quad \text{(Rayleigh criterion)} \tag{3.8}$$

where s is the rms height of the surface.

The Rayleigh condition is a first order classifier of surface roughness, but for scattering models in the microwave region, a more accurate condition is required where the wavelength is of the order of the rms height. Fraunhofer roughness criterion provides such requirement for the far-filed distance of an antenna. The Fraunhofer criterion is more consistent with experimental observations.

$$s < \frac{\lambda}{32\cos\theta_i} \quad \text{(Fraunhofer criterion)} \tag{3.9}$$

Beckmann and Spizzichino [44] state that: "*the same surface may be rough for some wavelengths and smooth for others; or for the same wavelength it may be either rough or smooth for different angles of incidence*."

3.3 SURFACE SCATTERING MODELS

A random rough surface is characterized by: rms height *(h)*, correlation length *(l)*, and auto correlation function *(ACF)*. The correlation length is defined as the distance over which the auto correlation function falls by 1/e [45]. Electromagnetic models for scattering by random rough surfaces involve the use of the two most common forms for the correlation function: Exponential Correlation Function (ECF) and Gaussian Correlation Function (GCF) represented by equations (4.10) and (4.11) respectively. For soil surfaces, the exponential correlation function is a more realistic choice and it has been shown that ECF can be used to match active remote sensing experimental data [46].

$$\rho_e = e^{-(\sqrt{x^2+y^2}/l)} \quad \text{(exponential)} \tag{3.10}$$

$$\rho_G = e^{-(x^2+y^2/l^2)} \quad \text{(Gaussian)} \tag{3.11}$$

The backscatter behavior is a function of the radar wave parameters and the surface's geometrical and dielectric properties: the wavelength, incidence angle, polarization configuration, dielectric constant, correlation length, and rms height of the surface. Surface scattering occurs at a rough interface between two different dielectric media. Scattering models of terrain are, at best, good approximations of the true scattering process experienced by a real radar observing a real terrain surface or volume [7]. They serve as guides to explain experimental observations and as predictors of how the radar scattering coefficient σ^0 is likely to behave as a function of a particular terrain parameter of interest [7].

The three-well establishes models are: Physical Optics (PO), Geometrical Optics (GO), and Improved Integral Equation Model (I^2EM). The integral equation model is built on the same basis as GO/PO, but it accounts also for multiple scattering contributions. It is also applicable to a wide range of roughness conditions and frequencies. That's why the I^{2}EM model was used in our simulations of σ^0 for soil surfaces.

3.3.1 Physics Optics (PO) Model (Medium-Rough to Rough Surfaces)

The PO model validity range is defined by the following conditions:

$$kl > 6 \quad \frac{1}{k} < s < 0.06kl^2 \tag{3.12}$$

where k is the wavenumber of the incident plane wave. The non-coherent surface scattering coefficient is then given as a function of the incidence angle θ by [47, 48]:

$$\begin{aligned}\sigma^0_{pp}(\theta) &= 2k^2\cos^2\theta\ \Gamma_{pp}(\theta)e^{-(2ks\cos\theta)^2}\\ &.\sum_{n=1}^{\infty}(4k^2s^2\cos^2\theta)^n / n!\int_0^{\infty}\rho^n(x)\,\mathrm{J}_0(2kx\sin\theta)x\,dx\end{aligned} \tag{3.13}$$

where J_0 is the zero-th order Bessel function of the first kind, Γ_{pp} is the Fresnel reflectivity, and ρ(x) is the surface autocorrelation function.

3.3.2 Geometric Optics (GO) Model (Very Rough Surfaces)

The GO model validity range is defined by the following conditions:

$$kl > 6 \quad (2ks\cos\theta)^2 > 10 \tag{3.14}$$

where the non-coherent surface scattering coefficient is then given as a function of the incidence angle θ_i by [48, 49]:

$$\sigma^0_{pp}(\theta) = \frac{\Gamma(0)e^{-\tan^2(\theta)/2m^2}}{2m^2\cos^4\theta} \tag{3.15}$$

where m = √2s/l is the rms slope of the surface and Γ(0) is the Fresnel reflectivity evaluated at normal incidence:

$$\Gamma(0) = \left|\frac{1-\sqrt{\varepsilon}}{1+\sqrt{\varepsilon}}\right|^2 \tag{3.16}$$

3.3.3 Improved Integral Equation Model (I^{2}EM) (Smooth to Rough)

The I^{2}EM is applicable on a wide range of surfaces, from smooth to rough. The I^{2}EM's validity range is given by [50, 51]:

$$ks < 3 \tag{3.17a}$$

$$(kl)(ks) < \mu_k \sqrt{|\varepsilon|} \tag{3.17b}$$

$$\cos^2\theta \frac{(ks)^2}{\sqrt{0.46kl}} \exp\left[-\sqrt{2\times 0.46kl(1-\sin\theta)}\right] \ll \tag{3.17c}$$

where μk is a constant and its Gaussian value, and the exponential ACFs are 1.6 and 1.2 respectively [50, 51, 52]. The co-polarized backscattering coefficient equation according to [7, 50, 51]:

$$\sigma_{pp}^{0}(\theta) = \frac{k^2}{4\pi} e^{-2k^2 s^2 \cos^2\theta} \sum_{n=1}^{\infty} \left|I_{pp}^{n}\right|^2 \frac{W^{(\mathrm{n})}(2k\sin\theta, 0)}{n!} \tag{3.18}$$

where

$$I_{pp}^{n} = (2ks\cos\theta) f_{pp} \exp(-k^2 s^2 \cos^2\theta) + (ks\cos\theta)^n F_{pp} \tag{3.19}$$

and pp is either the hh or vv polarizations; k stands for the radar wavenumber (k = 2π/λ, λ wavelength); s is the rms height; θ denotes the incidence angle; and $W^{(n)}$ is the Fourier transform of *n*th power of the ACF [50]. f_{hh}, f_{vv}, F_{hh}, and F_{vv} are approximated by the following equations:

$$f_{hh} = \frac{-2R_h}{\cos\theta} \tag{3.20a}$$

$$f_{vv} = \frac{2R_v}{\cos\theta} \tag{3.20b}$$

$$F_{hh} = 2\frac{\sin^2\theta}{\cos\theta}\left[4R_h - (1-\frac{1}{\varepsilon})(1+R_h)^2\right] \tag{3.20c}$$

$$F_{vv} = 2\frac{\sin^2\theta}{\cos\theta}\left[(1-\frac{\varepsilon\cos^2\theta}{\varepsilon-\sin^2\theta})(1-R_v)^2 - (1-\frac{1}{\varepsilon})(1+R_v)^2\right] \tag{3.20d}$$

where the horizontally and vertically polarized Fresnel reflection coefficients, R_h and R_v, are given by:

$$R_h = \frac{\cos\theta - \sqrt{\varepsilon - \sin^2\theta}}{\cos\theta + \sqrt{\varepsilon - \sin^2\theta}} \tag{3.21a}$$

$$R_v = \frac{\varepsilon\cos\theta - \sqrt{\varepsilon - \sin^2\theta}}{\varepsilon\cos\theta + \sqrt{\varepsilon - \sin^2\theta}} \tag{3.21b}$$

where ε is the ground relative dielectric constant.

Due to the nonlinearity of (3.18), the model inversion, i.e., solving the I^2EM for its parameters analytically, is almost impossible [50]. There are a few arithmetic methods which can be employed to calculate the surface parameters knowing the backscattering coefficient and the imaging parameters [50, 53]. In spite of the development of intelligent computation methods such as neural networks and the Bayesian method, one of the best and most direct methods in this respect is the Look-up table (LUT) [54, 55]. In the LUT method, the backscattering coefficient values for different values of the surface roughness parameters and dielectric constant are calculated using (3.18), and then, the surface parameters corresponding to the backscattering coefficients can be calculated by interpolation and reversed matching [50].

The input parameters for the I^2EM model are summarized in the block diagram of Figure 3-5. The I^2EM model can compute the backscattering or the bistatic scattering coefficient of a random surface with different types of correlation functions for any combination of receive and transmit wave polarizations.

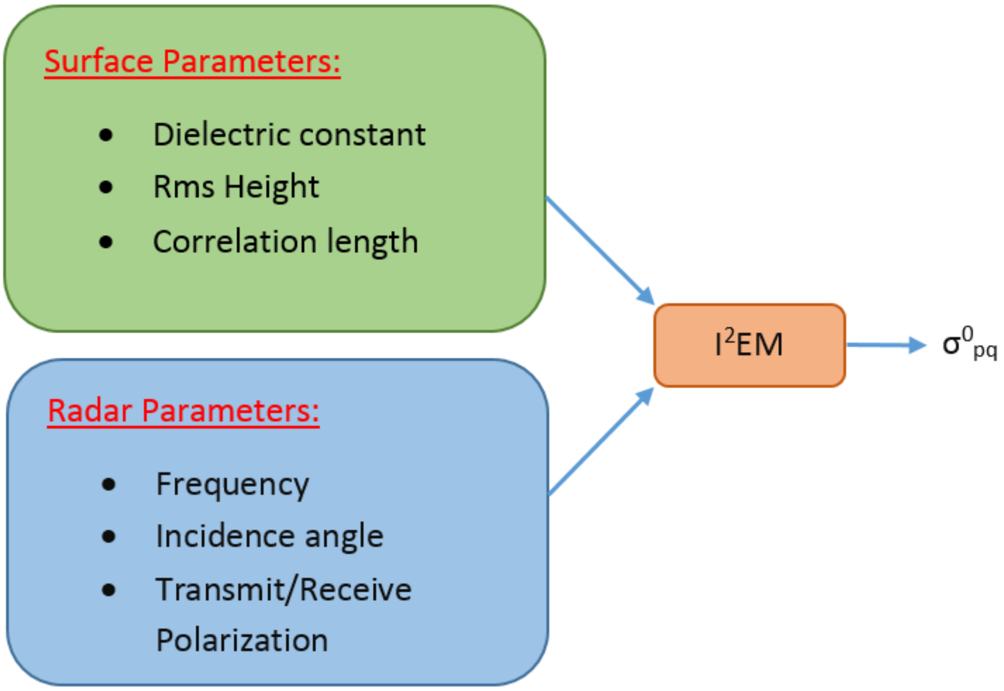

Figure 3-5: Block diagram representing the input parameters for the I^2EM model to calculate the backscattering coefficient.

3.4 NUMERICAL SIMULATION OF EM SCATTERING FROM ROUGH SURFACE

Numerical simulation of electromagnetic scattering from a randomly rough surface has been a topic of successive study for many years because of its broad applications such as terrain remote sensing, radar surveillance over oceanic surface and so on [56, 57]. Numerical methods can calculate the exact scattered field by solving Maxwell’s equations so that the bistatic scattering coefficient can be determined. It is impossible to model an infinite rough surface numerically, so a procedure to do that is summarized in [58] where the bistatic scattering coefficient is averaged over N different rough surfaces with the same length L and the same roughness conditions.

3.4.1 Procedure

The scattered electric field by each rough surface is calculated in the far field region at a range R_r from the surface as function of the scattering angle. This is done for N different rough surfaces with the same rms height *s* and correlation length *l*. Then, the bistatic scattering coefficient is averaged over the N surfaces for incident polarization *q* (H or V) and scattered polarization *p* (H or V):

$$\sigma^0_{pq} = \frac{4\pi R_r^2}{A\left|E^i_q(\theta_i,\phi_i)\right|^2}\frac{1}{N}\sum_{j=1}^{N}\left|E^s_{p,j}(\theta_s,\phi_s)\right|^2 \tag{3.22}$$

where E^i (θ_i, ϕ_i) is the incident electric field, E^s (θ_s, ϕ_s) is the scattered electric field, and *A* is the illuminated area. If *p* and *q* are the same, σ^0_{pq} is said to be the co-polarized backscattering coefficient; however, if *p* and *q* are different, σ^0_{pq} is the cross-polarized backscattering coefficient. For a rough surface being illuminated by a plane wave, the bistatic scattering coefficient for a single surface is defined as [41]:

$$\gamma^0_{pq}(\theta_s,\phi_s;\theta_i,\phi_i) = \lim_{r\to\infty}\frac{4\pi r^2\left|E^s_p\right|^2}{\left|E^i_q\right|^2 A\cos\theta_i} \tag{3.23}$$

In the backscattering direction $\theta_s = \theta_i$ and $\phi_s = \pi + \phi_i$, the monostatic backscattering coefficient is defined as:

$$\sigma^0_{pq}(\theta_i,\phi_i) = \cos\theta_i \gamma^0_{pq}(\theta_s = \theta_i, \phi_s = \pi + \phi_i; \theta_i, \phi_i) \tag{3.24}$$

In general, the total bistatic scattering coefficient σ^0_{pq} consists of a coherent component $\sigma^0_{pq\text{-coh}}$ and an incoherent component $\sigma^0_{pq\text{-inc}}$. The coherent component exists only along the specular direction, while the incoherent component exists in all directions. Because the coherent field is only in the specular direction, radar backscattering only receives the incoherent field [59].

In the numerical procedure, one uses a random rough surface of finite extent. So, the coherent field will be spread out over an angular width depending on the size of the rough surface. Then, the non-coherent backscattering coefficient can be calculated as:

$$\sigma_{pq}^{0} = \frac{4\pi R_r^2}{A\left|E_q^i(\theta_i,\phi_i)\right|^2}\left[\frac{1}{N}\sum_{j=1}^{N}\left|E_{p,j}^s(\theta_s,\phi_s)\right|^2 - \frac{1}{N^2}\sum_{j=1}^{N}\left|E_{p,j}^s(\theta_s,\phi_s)\right|^2\right] \tag{3.25}$$

In the averaging procedure, the choice of the surface length L is an important consideration in the numerical calculation. It is limited by conditions based on the wavelength λ and the correlation length *l*. The surface size must be large compared to the wavelength so that the surface can be considered macroscopic in its interaction with the incident beam where important interactions are not lost [60]. In [46], it was found that a surface size of 8λ is sufficiently large for convergence.

3.4.2 Incident Beam

The incident field of the transmitter being far from the terrain can be approximated to a plane wave. For a finite surface, the plane incident wave leads to an edge effect on the circumference of the calculation area so that the calculated scattered field accuracy is reduced. That's why tapered incident waves are applied in order to avoid artificial reflections from the edges of the illuminated finite surface by having a zero amplitude at the edges. So, the two important parameters that should be determined before setting up the HFSS simulation are the tapering parameter *g* and the finite surface length *L*. The tapering parameter *g* is a factor which controls the beamwidth of the wave which directly affects the validity of the scattering calculation.

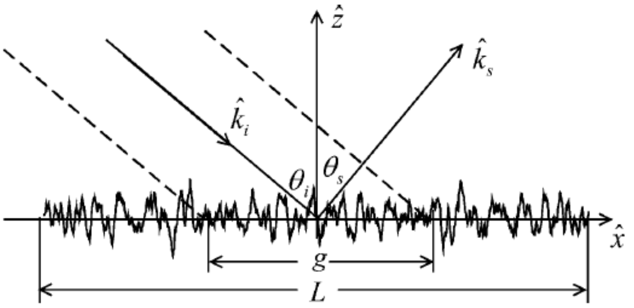

Figure 3-6: Geometry of the problem [57].

For a minimum error in the Helmholtz equation of 10^{-4}, a simple empirical formula is proposed:

$$g_{\min} = \frac{6}{(\cos\theta_i)^{1.5}}\lambda \tag{3.26}$$

A flexible choice of g is proposed by [40] depending on incident angle, but it cannot be used for low grazing incident angles:

$$g \in (\mathrm{L}/10, \mathrm{L}/4) \tag{3.27}$$

Considerations regarding the choice of *g* and *L* are summarized below:

- *g* should be large enough to make the wave equation in the range of an allowable error.
- Too small g not following the criterion significantly damage the specular direction pattern.
- Setting a maximum value of *g* is important for the calculation of the bistatic scattering coefficient which requires the illuminated surface area to be calculable ($A=\pi g^2/\cos^2\theta$ [61]).
- L should be larger than several correlation lengths of the rough surface and also be limited to make computation efficiency.
- L must be large enough so that important interactions are not lost.

Further increasing L does not significantly improve scattering computation because the larger the surface, the longer the computation time and memory.

3.5 RANDOM ROUGH SURFACE GENERATION

The ability to generate a random rough surface to build a complex multilayered structure such as (air-snow-ground) with non-planar surfaces can improve our understanding of how electromagnetic waves are scattered by targets. However, it is impossible to create directly a randomly rough surface with a certain autocorrelation function with HFSS. Therefore, Matlab was the key to generate such rough surface and then import it into HFSS.

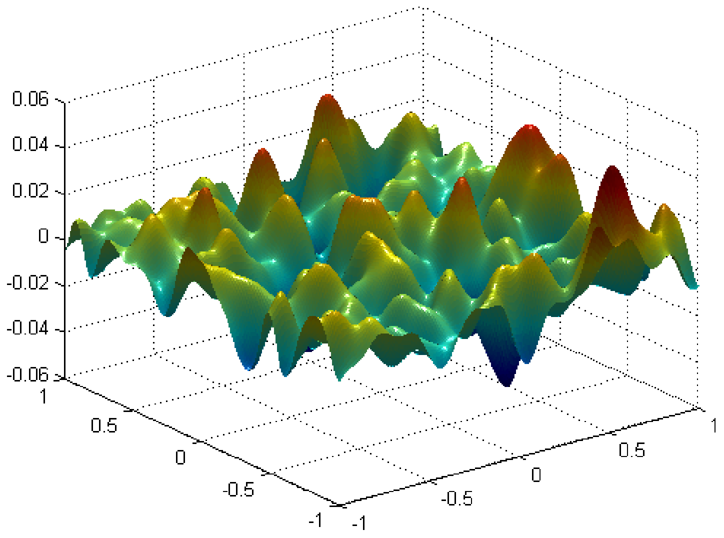

Rms height = 1.12 cm
Correlation length = 8.4 cm

Figure 3-7: 2D rough surface generated in MATLAB for a length of 2 m with 1.12 cm rms height and 8.4 cm correlation length using a Gaussian correlation function.

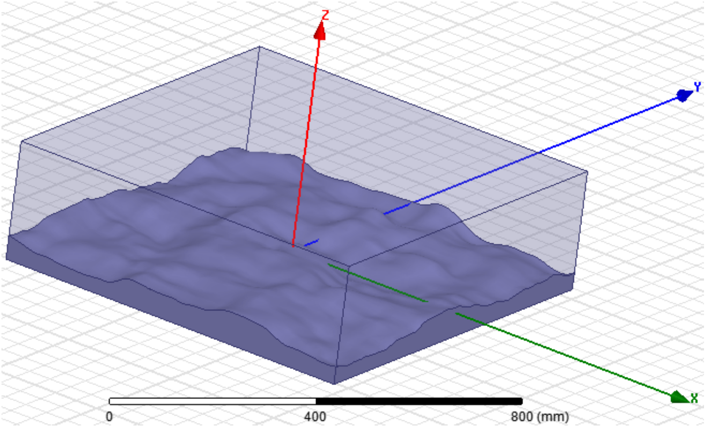

Figure 3-8: Two layered 3D structure with a rough interface in HFSS.

The two-dimensional random rough surface generation is solved in Matlab [62]. A set of uncorrelated random numbers with zero mean and standard deviation *h* is created using the command *randn*. The Fourier transform of these generated random numbers is multiplied by the Fourier transform of the ACF. An inverse Fourier transformation of the multiplication result yields the random rough surface followed by normalization as shown in Figure 3-7. Then, a stereolithographic (STL) file is written from the obtained surface coordinates which is imported into a CAD software to create the volume to be studied in an electromagnetic simulator. The final structure is imported into HFSS as shown in Figure 3-8. This procedure was developed because it is more flexible to use MATLAB generation instead of HFSS.

3.6 SURFACE SCATTERING NUMERICAL APPROACH OF AIR/SOIL MEDIA USING HFSS

The backscattered signal received by a radar is a result of either surface scattering, volume scattering, or combination of both. As a first step, the scattering coefficient of a two layered media (air-soil) with a rough interface is calculated for H polarization at different incidence angles for different values of soil moisture. The simulated results are compared with some theoretical scattering models. The steps involved in the calculation of the scattering coefficient throughout this chapter is shown in Figure 3-9.

Table 3-1: Permittivity of soil as function of soil moisture.

Soil Moisture (%)	**Permittivity (ε_{soil})**
m_s=5%	4.5 - j3.0
m_s=20%	11.3 - j1.5
m_s=35%	20.6 - j3.0

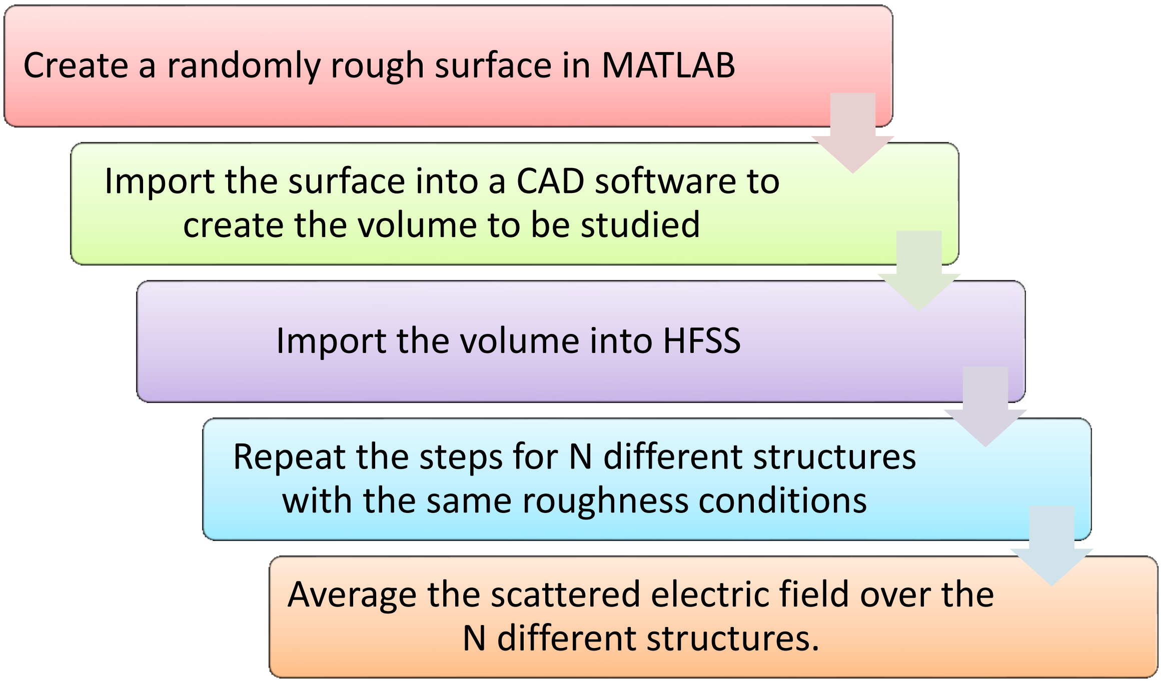

Figure 3-9: Different steps involved in the numerical simulation.

Table 3-1 summarizes some values of soil permittivity as function of liquid water content in the soil. These values were taken from [7, page 434] and will be used in the simulation when defining the material properties of soil in HFSS. The set up required for a two-layered study in HFSS with the boundary conditions used in the simulation is illustrated in Figure 3-10. This figure shows the model constructed for a single rough surface in the averaging process with an exponential autocorrelation function where the surface size is 8λ, the rms height is 1.12 cm, and the correlation length is 8.4 cm.

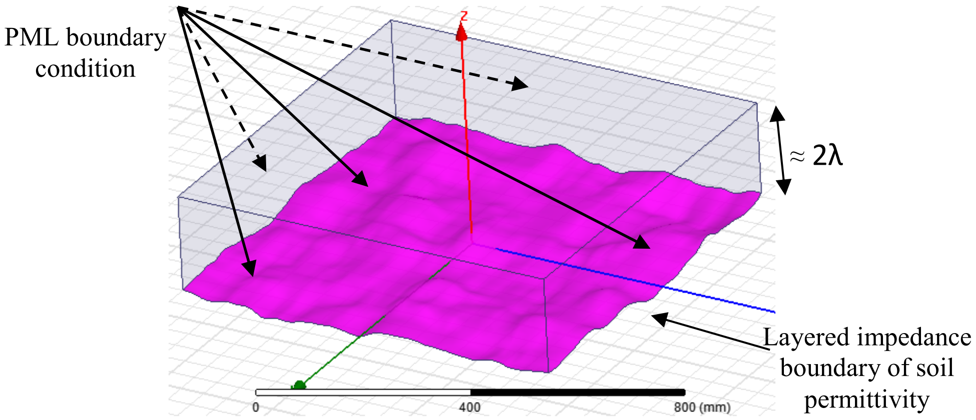

Figure 3-10: Diagram showing the model constructed for a single rough surface for 0.8 m length, 1.12 cm rms height, and 8.4 cm correlation length.

3.6.1 Air/Soil Backscattering Coefficient for a Rough Surface with a GCF

The operating frequency ($f = 4.75$GHz) as well as the roughness information ($s = 1.12$ cm; $l = 8.4$ cm) used in the simulation were taken from experimental data found in [7, page 436]. Bistatic scattering involves four angles: incidence and scattering angles (θ_i and θ_s) and azimuth angles (φ_i and φ_s). The tested incidence angle range are (0°, 10°, 20°, 30°) and the azimuth angle is fixed at 0°. The scattered electric field is calculated by the simulator inside the geometry. However, HFSS can perform a near to far field calculation from the boundary radiation surfaces by inserting a far field sphere. Such scattered field is averaged over N different surfaces with the same rms height and correlation length to achieve convergence in the solution. This solution could be taken as the value obtained in case of an infinite rough surface. Figure 3-11 shows the calculated backscattering coefficient as function of the number of surfaces N with parameter values summarized in Table 3-2. In most literatures, a value of $g = L/4$ is the most chosen choice in the averaging process.

It is observed from Figure 3-11 that the expected convergence happened for $N = 15$, where a variation of less than 1 dB occurs when averaging on higher number of surfaces ($N > 15$). Figure 3-12 shows the result obtained for the co-polarized bistatic scattering coefficient after averaging over a high number of surfaces. This graph is obtained for a high soil moisture with permittivity $20.6 - j\,3$ where the incident beam is H-polarized and roughness conditions are as those found in Table 3-2. The co-polarized bistatic scattering coefficient calculated using the finite element method is compared with the I^{2}EM (Integral Equation Method) theoretical model where a good agreement is seen.

Table 3-2: Parameter Values Used in the HFSS Simulation for a Surface with a Gaussian Autocorrelation Function.

Parameter	**Value**
Operating Frequency, f	4.75 GHz
RMS Height, s	1.12 cm
Correlation Length, l	8.4 cm
Incidence Angle, θ_i	20°
Surface Size, L	8λ
Polarization, pq	HH-pol
Soil Moisture m_s	35%

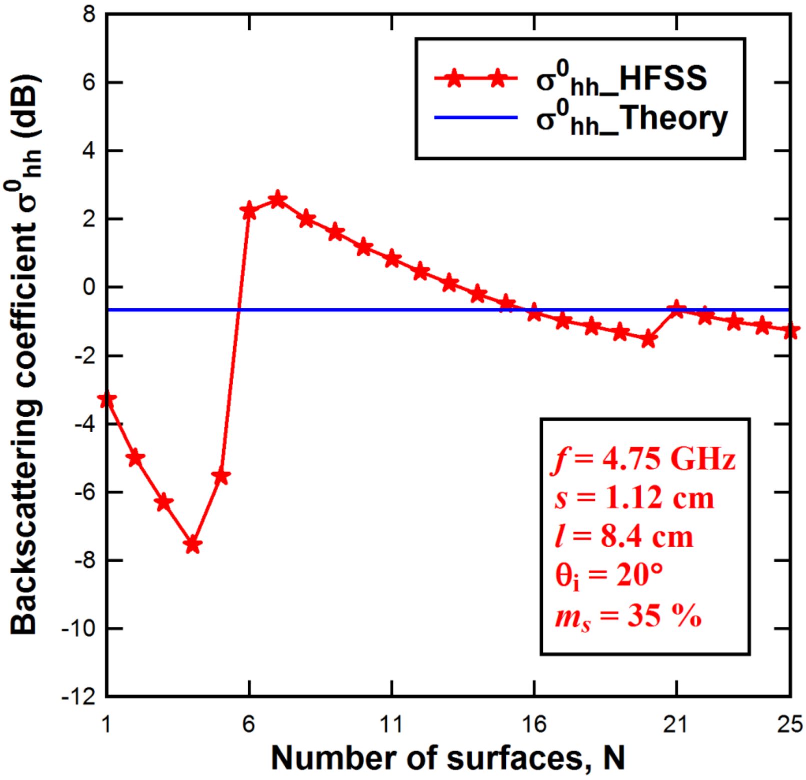

Figure 3-11: The calculated backscattering coefficient as function of the number of surfaces with Gaussian correlation function for parameter values found in Table 3-2.

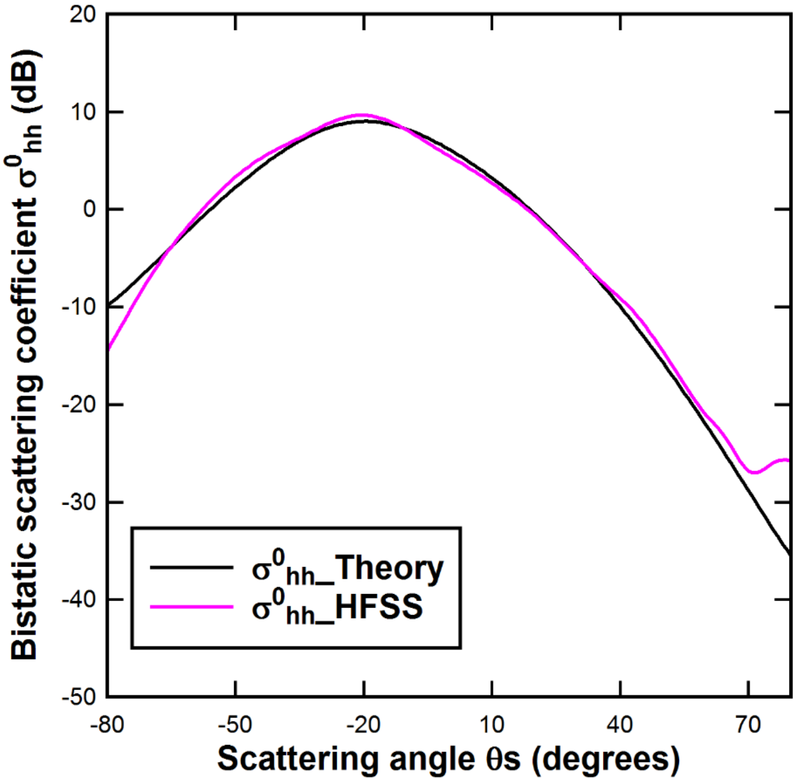

Figure 3-12: The bistatic scattering coefficient as function of the scattering angle for the same parameter values found in Table 3-2.

3.6.2 Air/Soil Backscattering Coefficient for a Rough Surface with a ECF

Another setup is done for a rough surface with an exponential correlation function keeping the parameter values the same but with a different operating frequency ($f = 3$ GHz). Changing the frequency leads to a change in the surface size to a 0.8 m (8λ). A variety of incidence angles and soil moisture were tested.

Figure 3-13 shows the results obtained of the co-polarized backscattering coefficient using the averaging process for a high soil moisture with permittivity $\varepsilon_{soil} = 20.6 - j\,3$ as function of the incidence angle where the incident beam is H-polarized and roughness conditions are as those found in Table 3-2. The theoretical and simulation values are in a close agreement. The backscattering coefficient as well as the bistatic scattering coefficient in the specular direction is shown in Figure 3-14 as function of soil moisture where the incident angle is fixed at 20° and the beam is H-polarized. All results for all ranges of incidences angles and soil moisture agree well with the famous scattering model I^{2}EM.

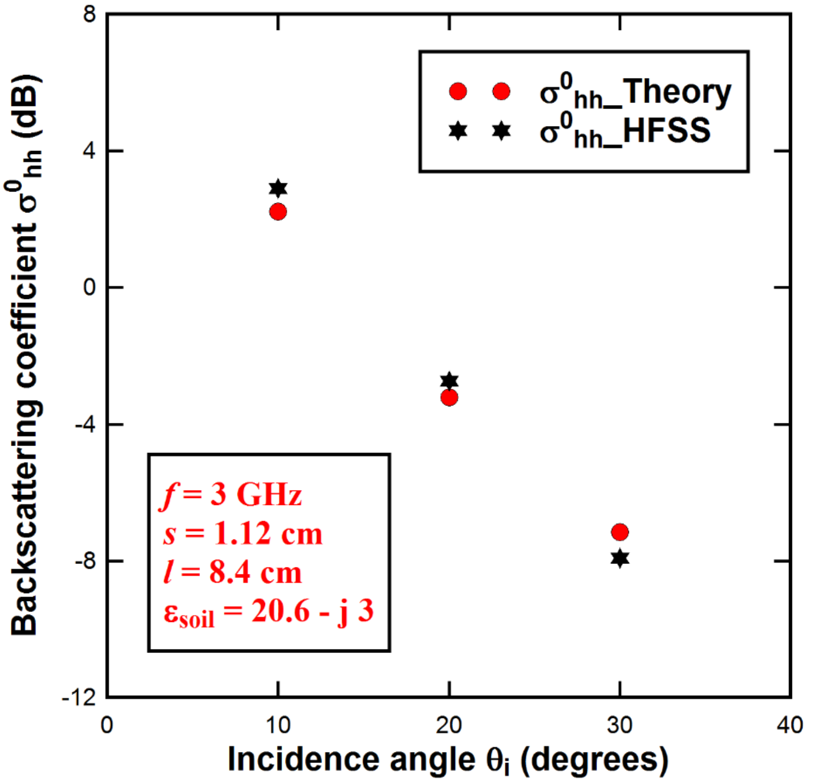

Figure 3-13: The backscattering coefficient as function of the incidence angle θ_i.

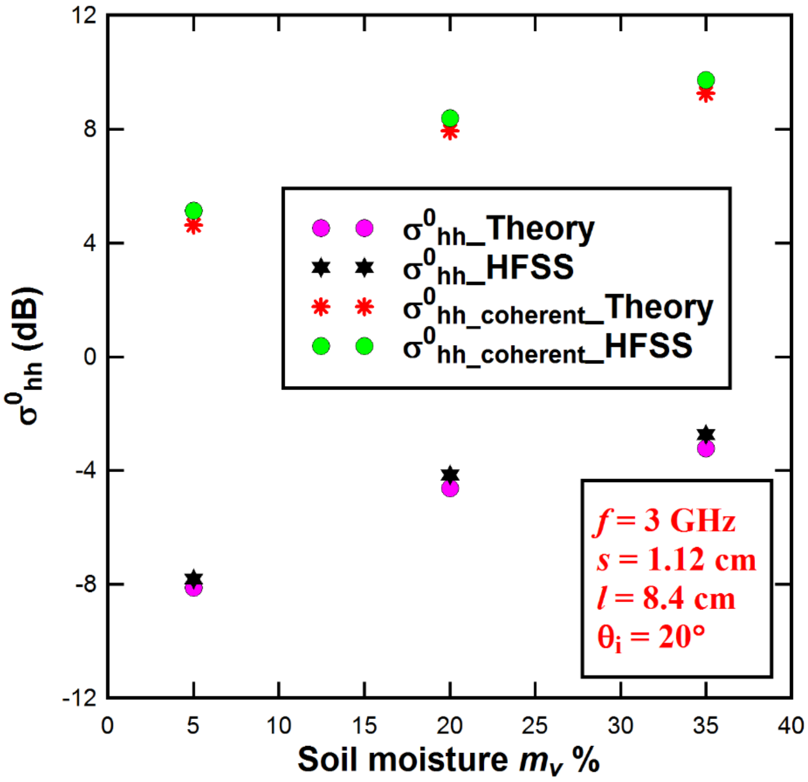

Figure 3-14: The backscattering coefficient and the bistatic scattering coefficient as function of the soil moisture for the parameter values shown on the figure.

3.7 SURFACE SCATTERING EFFECT IN THREE-LAYERED MEDIA WITH ROUGH INTERFACES

Our main objective of this thesis is to retrieve snow depth over ground. In this section, the numerical study of air-snow-ground system is studied considering snow as a homogeneous media; hence, scattering is only influenced by the surface boundary. Experimental measurements of σ^0 for soil surfaces with comparable surface conditions (rms height s, correlation length (*l*), and dielectric constant (ε) are much closer in level to the predictions of the I^2EM for a surface with an exponential correlation function than for a Gaussian [7]. In this part of the numerical simulation, comparison was done with empirical models based on measurement data known as: PRISM model and SMART model.

Both theoretical models and experimental observations indicate that for a random surface observed by a radar at an incidence angle θ and microwave frequency *f* [7]:

a) The magnitudes of the surface backscattering coefficients are governed primarily by the rms height (*s*) and moisture content (m_s), and secondarily by the correlation length (*l*).

b) At incidence away from nadir, the co-pol ratio p = $\sigma^0_{hh}/ \sigma^0_{vv}$ of a relatively smooth surface (with $ks \approx 0.1$) is on the order of 0.1 to 0.4 (depending on θ and m_s), and increases with ks to 1 as ks increases to beyond 2.

c) For a perfectly smooth surface, $\sigma^0_{vh} = 0$. Increasing surface roughness causes the cross-pol ratio q = $\sigma^0_{hv} / \sigma^0_{vv}$ to increase monotonically with ks, reaching a plateau as ks exceeds 2.

3.7.1 Polarimetric Radar Inversion for Soil Moisture (PRISM) model

These considerations suggest that an empirical model could be developed to measure the dielectric constant and moisture content of the soil medium. This is was done by the University of Michigan team by Yisok Oh (1992) [63] who developed the following empirical model:

$$p = \sigma^0_{hh} \ / \ \sigma^0_{vv} = \left[1 - \left(\frac{2\theta}{\pi} \right)^{\alpha} e^{-ks} \right]^2 \tag{3.28}$$

where θ is the incidence angle in radians, k is the wavenumber, s is the rms height, and:

$$\alpha = \frac{1}{\Gamma_0} \tag{3.29}$$

with Γ_0 representing the surface Fresnel reflectivity at normal incidence,

$$\Gamma_0 = \left| \frac{1-\sqrt{\varepsilon}}{1+\sqrt{\varepsilon}} \right|^2 \tag{3.30}$$

The cross-polarized ratio is defined as:

$$q = \sigma^0_{hv} \ / \ \sigma^0_{vv} = 0.23\Gamma_0^{1/2} \left[1 - e^{-ks} \right] \tag{3.31}$$

Using the empirical models developed for p and q, the following models were developed for σ^0_{vv}, σ^0_{hh}, and σ^0_{hv}:

$$\sigma^0_{vv} = 0.7[1 - e^{-0.65(ks)^{1.8}}] \frac{\cos^3 \theta}{\sqrt{p}} [\Gamma_v(\theta) + \Gamma_h(\theta)] \tag{3.32}$$

$$\sigma^0_{hh} = p \ \sigma^0_{vv} \tag{3.33}$$

$$\sigma^0_{hv} = q \ \sigma^0_{vv} \tag{3.34}$$

The inversion process for the estimation of s and m_v using the inverse model of PRISM is based first on a good estimator of σ^0_{vv}, σ^0_{hh}, and σ^0_{hv}. From these measurements, we compute the co-polarized and cross-polarized ratios p and q. By eliminating ks from (4.28) and (4.31), we obtain the following nonlinear equation for Γ_0:

$$\left(\frac{2\theta}{\pi}\right)^{1/3\Gamma_0}.\left[1-\frac{q}{0.23\sqrt{\Gamma_0}}\right]+\sqrt{p}-1=0 \tag{3.35}$$

where θ is in radians and Γ_0 is solved using an iterative method where the permittivity can be calculated using (4.30) by neglecting the imaginary part of the dielectric constant which is a valid approximation for a soil material. This technique cannot estimate *ks* for very rough surfaces (*ks* > 3) because *p* and *q* are not sensitive to such surfaces.

3.7.2 Soil Moisture Assessment Radar Technique (SMART) model

Dubois et al. (1995) [64] developed a semi-empirical approach for modelling σ^0_{vv} and σ^0_{hh} named Soil Moisture Assessment Radar Technique (SMART) for soil moisture inversion. The algorithm is optimized for bare soils with $ks \leq 2.5$, $m_s \leq 35\%$ and $\theta \geq 30°$.

$$\sigma^0_{hh}=10^{-2.75}.\frac{\cos^{1.5}\theta}{\sin^5\theta}.10^{0.028\varepsilon'\tan\theta}(ks\sin\theta)^{1.4}\lambda^{0.7} \tag{3.36}$$

$$\sigma^0_{vv}=10^{-2.35}.\frac{\cos^{3}\theta}{\sin^3\theta}.10^{0.046\varepsilon'\tan\theta}(ks\sin\theta)^{1.1}\lambda^{0.7} \tag{3.37}$$

where ε' is the real part of the soil dielectric constant. The inversion equations are given by [65]:

$$\begin{aligned}\varepsilon'=\frac{1}{3.36\tan\theta}&[14\sigma^0_{vv}(\mathrm{dB})-11\sigma^0_{hh}(\mathrm{dB})\\&+26.5-255\log_{10}(\cos\theta)\\&-130\log_{10}(\sin\theta)-21\log_{10}(\lambda)]\end{aligned} \tag{3.38}$$

$$\begin{aligned}\log_{10}(ks)=-0.083\sigma^0_{vv}(\mathrm{dB})&+0.137\sigma^0_{hh}(\mathrm{dB})+1.807\\&+0.446\log_{10}(\cos\theta)+3.345\log_{10}(\sin\theta)\\&-0.375\log_{10}(\lambda)\end{aligned} \tag{3.39}$$

with λ in cm.

The SMART model has several attractive features [7]: its expressions are straightforward and easy to use; it relies on only hh and vv polarizations; and it provides estimates of m_v and *s* with good accuracies.

3.7.3 Results

The same numerical procedure as in section 3.6 is done to calculate the HH-polarized backscattering coefficient of a three-layered media (air-snow-soil) where snow-soil interface is rough as shown in Figure 3-15. PML boundary conditions were used at the sides of the calculation area to prevent reflections. The air-snow interface was chosen to be planar because the backscattering coefficient at the air-dry snow interface is neglected with respect to the total backscatter due to the small dielectric contrast between air and snow. The simulated results are compared with the most famous theoretical scattering models. Table 3-3 shows the parameter values used in the simulation setup.

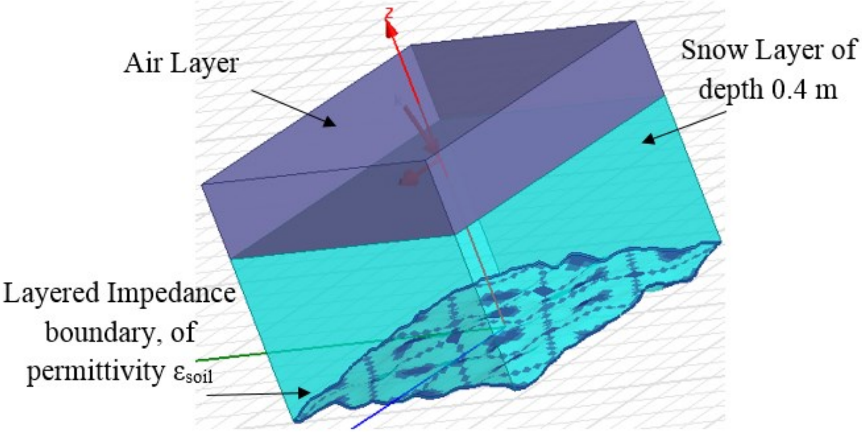

Figure 3-15: Three-layered structure setup in HFSS with the snow-ground interface being rough.

Table 3-3: Parameter Values Used in the HFSS Simulation for a Three-Layered Structure with a Rough Snow-Ground Interface.

Parameter	**Value**
Operating frequency f	3 GHz
Incidence angle θ_i	0°,10°,20°,30°,40°,50°
Surface size L	0.8 m = 8λ
Polarization pq	HH
Soil moisture m_v	35% (ε_{soil} = 20.6 - j3.0)
RMS height s	1.12 cm
Correlation length cL	8.4 cm
Correlation function	ECF
Snow depth	0.4 m
Snow density	0.45 g/cm^3

Figure 3-16 shows the results obtained of the co-polarized backscattering coefficient using the averaging process for a high soil moisture of permittivity $\varepsilon_{soil} = 20.6 - j\,3$ where the incident beam is H-polarized and roughness conditions are as those found in Table 3-3. The co-polarized backscattering coefficient calculated using the FEM is compared with I^{2}EM (Improved Integral Equation Method) theoretical model, PRSIM and SMART models. Results are in a good agreement with the I^{2}EM model for incidence angles less than 30°; however for higher incidence angle, FEM results are in a closer agreement with the SMART model. The memory required and the CPU time for the simulations done are shown in Table 3-4.

Table 3-4: Memory and CPU Time.

Number of Layers	CPU Time for 1 surface	CPU Time for N surfaces	Memory Requirement for 1 surface
2 layers	10 min	3 hours	8 GB
3 layers	30 min	10 hours	16 GB

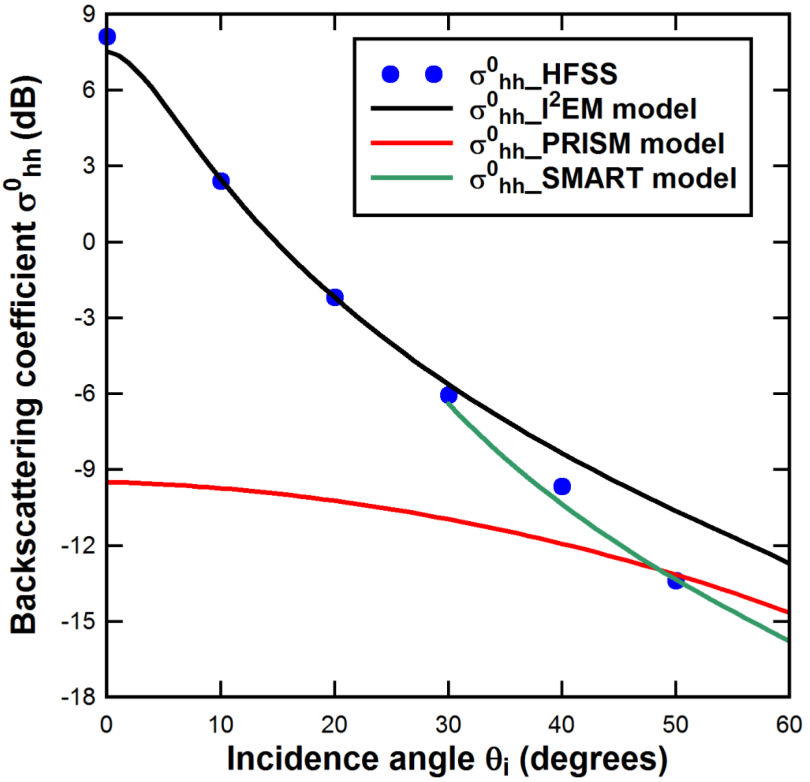

Figure 3-16: The backscattering coefficient as function of the incidence angle for the parameter values shown in Table 4-3 with a comparison with theoretical models.

3.8 VOLUME SCATTERING EFFECT IN LAYERED MEDIA WITH PLANAR INTERFACES

In contrast with surface scattering, which occurs at a rough interface between two different dielectric media, snow volume scattering is caused by ice crystals that are present in an air background. The following factors are important in analyzing volume scattering by scatterers is a certain homogeneous background:

- The size of the scatterers with respect to the wavelength.

- The shape and orientation of the scatterers in the medium.
- The dielectric constant of the scatterers.

These factors mainly determine the scattering pattern because small scatterers obey the Rayleigh phase function regardless of their shapes. Moreover, it could be known if the extinction coefficient is dominated by absorption or scattering losses.

As illustrated in Figure 3-17, the total backscatter σ^0_{total} received from snow above ground includes four scattering components:

$$\sigma^0_{total} = \sigma^0_{as} + \sigma^0_{v} + \sigma^0_{gv} + \sigma^0_{g} \qquad (3.40)$$

where σ^0_{as} is the surface scattering component by the air/snow interface, σ^0_{v} is the snow volume scattering due to ice inclusions, σ^0_{gv} is the multiple scattering component involving both surface and volume scattering mechanisms, and σ^0_{g} is the surface scattering by the snow/soil interface.

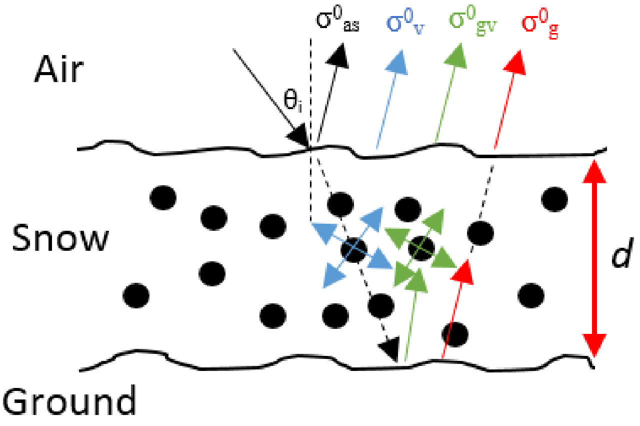

Figure 3-17: Scattering contributions for air-snow-ground multi-layered structure with rough interfaces and heterogeneous snow mixture.

The backscattering coefficient is affected by several physical parameters of the snow and soil layer. These parameters are:

- Volumetric liquid water content in snow m_v %.
- Snow depth d.
- Snow density ρ_s.
- Snow temperature T °C.
- Snow grain size r.
- Surface roughness (air-snow and snow-soil boundary).

The ground surface backscattering coefficient is approximated by the I^{2}EM model while the volume backscattering coefficient obeys the Rayleigh approximation for layers with small dielectric constant.

3.8.1 Single-Scattering Radiative Transfer Model (S^{2}RT/R)

This section describes the theoretical forward model for the calculation of the backscattering coefficient from air-snow-ground multilayered structure. The ground surface contribution, the snow volume contribution, and the snow-ground contributions are defined as in (3.41), (3.42), and (3.43) respectively:

$$\sigma_g^0 = \mathrm{T}_{pq}^2(\theta_i)\Upsilon_{pq}^2\sigma^0{}_{g,pq}(\theta_r) \tag{3.41}$$

$$\sigma_v^0 = \mathrm{T}_{pq}^2(\theta_i)0.75a\cos\theta_r(1-\Upsilon_{pq}^2)(1+\Gamma_g^2(\theta_r)\Upsilon_{pq}^2) \tag{3.42}$$

$$\sigma_{sg}^0 = \mathrm{T}_{pq}^2(\theta_i)[6\kappa_s d\Gamma_g(\theta_r)\Upsilon_{pq}^2] \tag{3.43}$$

The formulation given by (3.44) is the total backscattering coefficient which is the *S^{2}RT/R* model for a layer with a distinct upper boundary at polarization *pq* [7].

$$\begin{aligned}\sigma^0{}_{total,pq} &= \mathrm{T}_{pq}^2(\theta_i)[\Upsilon_{pq}^2\sigma^0{}_{g,pq}(\theta_r) + 0.75a\cos\theta_r(1-\Upsilon_{pq}^2)(1+\Gamma_g^2(\theta_r)\Upsilon_{pq}^2) \\ &\quad + 6\kappa_s d\Gamma_g(\theta_r)\Upsilon_{pq}^2] + \sigma^0{}_{as,pq}(\theta_i)\end{aligned} \tag{3.44}$$

where T_{pq} is the transmission from air to snow across the air-snow boundary, Υ_{pq} is the transmissivity throughout the snow volume, *a* is the albedo, θ_r is the refraction angle, Γ_g is the ground surface reflectivity, κ_s is the scattering losses, and *d* is the snow depth. The transmissivity of the snow layer can be expressed as:

$$\Upsilon_{pq} = \exp(-\frac{\kappa_e d}{\cos\theta_r}) \tag{3.45}$$

where κ_e is the extinction coefficient of the snow volume. The extinction coefficient accounts for absorption and scattering losses within the snow as seen in (4.46).

$$\kappa_e = \kappa_a + \kappa_s \tag{3.46}$$

The scattering albedo is defined as:

$$a = \kappa_s / \kappa_e \tag{3.47}$$

The volume absorption coefficient κ_a is defined in terms of the effective permittivity ε_{eff} of the medium and the wave number k_0 as shown in (3.48). In the case where the size of inclusions is much smaller than the wavelength, κ_s is much smaller than κ_a ($\kappa_e = \kappa_a$).

$$\kappa_a = -2k_0 \operatorname{Im}\left\{\sqrt{\varepsilon_{eff}}\right\} = \frac{2\pi\varepsilon''}{\lambda\sqrt{\varepsilon'}} \qquad (3.48)$$

where ε' and ε" are the real and imaginary parts of the complex dielectric constant of snow, and quantify the electromagnetic energy stored and energy loss in the medium respectively.

3.8.2 HFSS Calculation Setup

The simulation setup for the calculation of the backscattering coefficient due to volume scatterers is shown in Figure 3-18. It consists of a dry snow layer of depth $d = 0.1$ m. This layer is treated as a heterogeneous mixture where uniformly distributed scatterers (ice crystals of $r =$ 6 mm) are embedded in an air background.

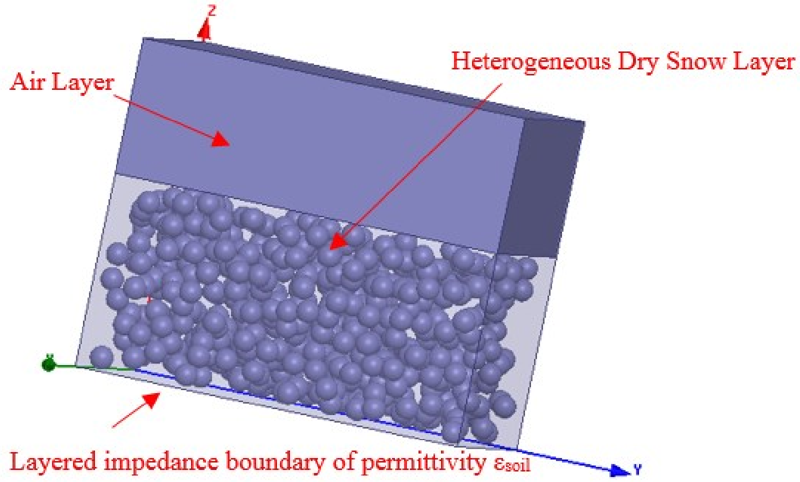

Figure 3-18: Three-layered structure setup in HFSS with planar interfaces and a heterogeneous snow volume.

The size distribution of the scatterers relative to the wavelength is an important factor in modeling radar scattering by a snow volume. Due to the assumption that Rayleigh approximation provides reasonably accurate results up to 15 GHz for much larger particles (r = 5 mm) [7], the numerical study is done on a sample of dry snow of density 0.1 g/cm^3 with a 6 mm ice particle radius at an operating frequency of 9 GHz. These chosen specifications for the snow sample are just a compromise between the available memory and the limited range of the applicability of Rayleigh approximation. All calculations were performed on an HPC of 24 cores with a systems memory of 192 GB RAM. Note that the study of surface and volume scattering effects were done separately due to the calculation CPU time as well as the required memory.

Table 3-5: Memory and CPU Time.

Snow density	**CPU Time for 1 surface**	**CPU Time for N surfaces**	**Memory Requirement**
0.1 g/cm^3	30 minutes	3 hours	150 GB

The procedure for calculating the bistatic scattering coefficient is the same as in (3.22) where the averaging process is done for mixtures with the same volume fraction of ice but with different positioning of inclusions. The calculation time for each sample is approximately 3 hours with 150 GB used memory. So, decreasing the size of the ice radius or increasing the snow density and depth requires much more CPU time and memory. Table 3-5 summarizes the values of the parameters used in the simulation setup.

Table 3-6: Parameter Values Used in the HFSS Simulation for a Three-Layered Structure with a Heterogeneous Snow Medium.

Parameter	**Value**
Operating frequency, f	9 GHz
Snow depth, d	0.1 m
Snow density, ρ_s	0.1 g/cm^3
Ice radius, r	6 mm
Permittivity of soil, ε_{soil}	5
Incident wave	Plane wave
N	20
Surface size, L	0.2 m
Polarization	HH
Incidence angle, θ_i	10°,20°,30°,40°,50°,60°

3.8.3 Results

First, the co-polarized backscattering coefficient is calculated as function of the number of snow samples for parameter values found in Table 3-4. It is observed from Figure 3-19 that the expected convergence occurred for N = 20, where a variation of less than 1 dB appears when averaging over a higher number of samples. So, averaging was done over 20 samples of snow at all incidence angles where the calculated value is the value that would be obtained for air-snow-ground multilayered structure of infinite size.

The calculated numerical results of the co-polarized backscattering coefficient using the averaging process are shown in Figure 3-20 at different incidence angles with an H-polarized incident beam. A comparison was done with S^2RT/R model where a good agreement is observed. Based on the obtained results, a conclusion can be drawn concerning the backscattering from dry snow. The backscattering coefficient decreases with increasing incidence angle and that's clear in Figure 3-20.

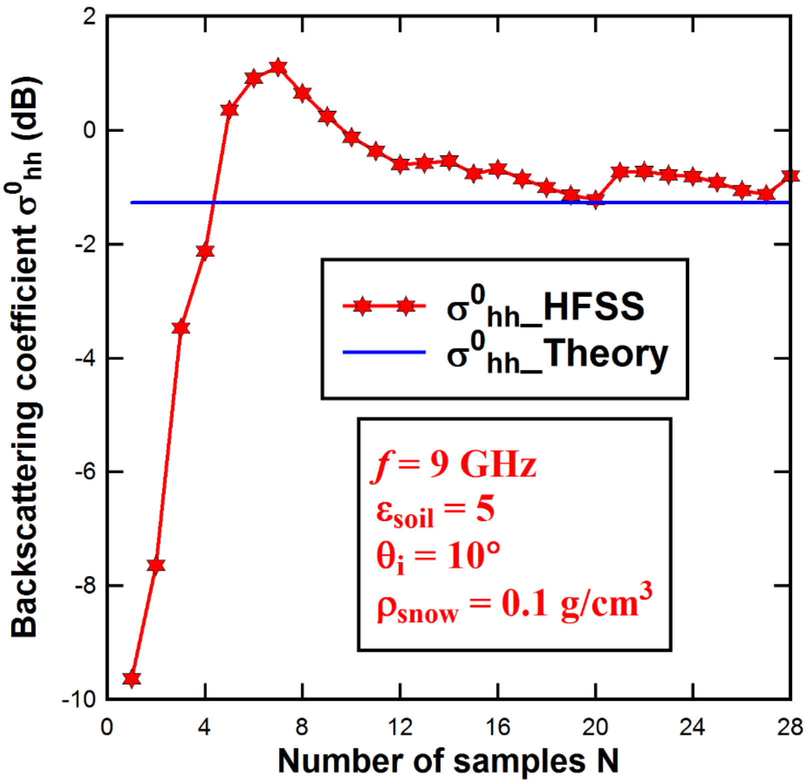

Figure 3-19: The calculated backscattering coefficient as a function of the number of samples at H-polarization and 10° incidence angle.

As a conclusion for dry snow, the backscattering coefficient is dominated by the scattering from the snow volume as well as the snow-ground interface. This is in contrast to the wet snow case because of the high dielectric losses of liquid water. This case was not illustrated numerically due to the heavy required memory and CPU time.

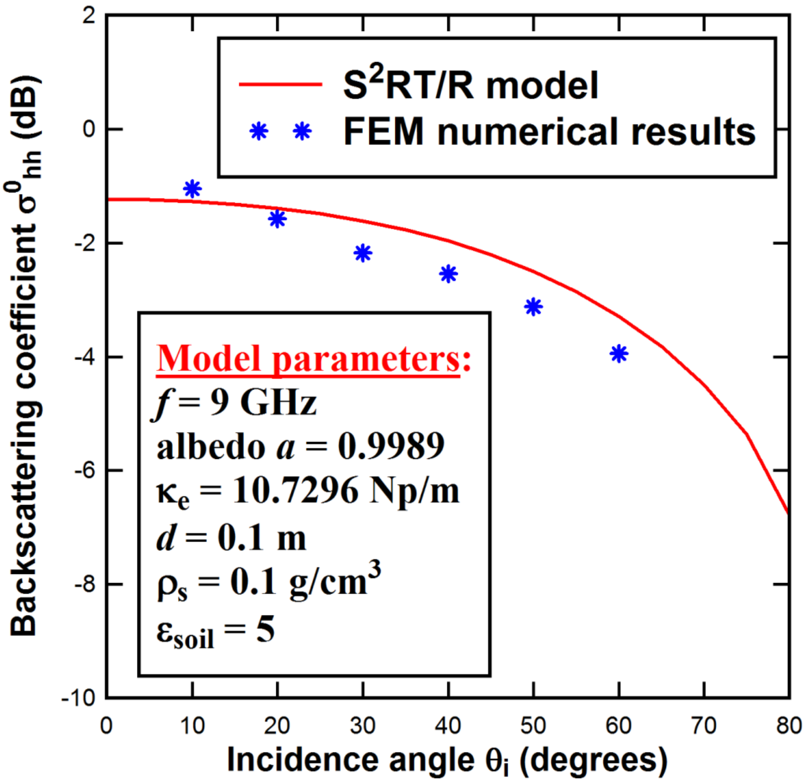

Figure 3-20: The calculated backscattering coefficient as a function of the incidence angle at H-polarization.

3.9 CONCLUSION

In this work, a multilayer numerical model formulation of radar backscattering from air-snow-ground system based on the finite element method is done. A good agreement is achieved between simulated data and theoretical ones. Results are in a good agreement with the I2EM model so that it can be applicable in our snow depth retrieval algorithm for the calculation of the backscattering contribution due the ground layer. The interest of our next study is to estimate snow depth from the provided backscattering coefficients for different frequencies and incidence angles using multiple antennas.

Chapter 4: Snow Depth Retrieval Algorithm using L- and X- Band Radar Backscattering Measurements

4.1 INTRODUCTION

An accurate measurement of snow layer thickness over ground is a crucial process for snow water equivalent (SWE) estimation. It has been demonstrated that active microwave sensors are valuable tools in retrieving snow parameters. Previous inversion algorithm studies were mainly based on the analysis of multi-frequency and multi-polarization backscattering coefficients. The development of a new inversion algorithm to retrieve snow depth from L- and X-band (2 and 10 GHz) active microwave sensors at different incidence angles is the subject of this chapter. The return signal from the medium is due to the ground roughness, the snow volume, and the noise from the radar system. So, surface and volume scattering effects are modeled from physical forward models, and noise effects are modeled by including a white Gaussian noise (WGN) into the simulation.

This inverse scattering problem involves two steps. The first is the estimation of snow density using L-band co-polarized backscattering measurement at normal incidence. The second is the recovery of the snow depth from X-band radar backscattering coefficients using two different incidence angles (10° and 30°). For a 0.02 noise variance, all retrieved values have an error less than 2% for a snow depth range of [50-300] cm.

4.2 HISTORICAL BACKGROUND

The study of snow depth retrieval has a long history. The main methods available for determining snow depth over an area are: direct measurements using a fixed snow stake, and predictions based on physical models. Frequency Modulated Continuous Wave (FMCW) radars have been used extensively for the purpose of snow thickness estimation [66, 67], where the objective of the FMCW radar is to gather two returns, one from the air - snow interface and the other from the snow - ground interface, with each producing its own unique beat frequency. The difference between the two represents the additional time delay associated with the transmitted signal traveling through the snow and reflecting off from the ground back toward the radar. Thus, the snow depth can be calculated. This method is based on how the system is able to resolve the air - snow and the snow - ground interfaces and how it can solve the problems related to the linearity of the chirp signal.

Another studies regarding snow physical properties retrieval methods are based on radar backscattering observations at different frequencies and polarizations. For example, an inversion algorithm of SWE using multi-frequency (L, C, X bands) and multi-polarization (*VV* and *HH*) microwave backscattering coefficients is represented by Shi and Dozier (2000) [3]. This inversion algorithm uses co- and cross- polarized channels for the separation of surface and volume scattering contributions and needs five measurements to estimate SWE. However, sensitivity analysis showed that backscattering signals at X-band or higher frequency bands is more sensitive to snow parameters than that at C-band. Hence, retrieving snow physical parameters at higher bands is more efficient.

High frequency Synthetic Aperture Radar (SAR) (X and Ku band) with multi-polarization is proposed by the snow observation programs: the European space agency CoReH2O space borne synthetic aperture radar, and Snow and Cold Land Processes (SCLP) of NASA. SWE inversion algorithm under this configuration is done by [68, 69]. Note that for Ku band frequencies, numerical techniques are needed because the first-order solutions of the radiative transfer (RT) equation for modeling the backscatter behavior from a snow layer is not applicable. However, Ku-band is more sensitive to shallow snow only. So, the frequency choice is a compromise between how much it is capable to penetrate a deep snow layer meeting our requirements and how much it is sensitive to snow parameters. That's why an operating frequency in the X-band spectrum (10 GHz) was chosen in our retrieval method where a typical value of penetration depth into dry snow is around 8 m at such wavelength.

4.3 PROPAGATION PROPERTIES OF SNOW

Snow depth (d) and density (ρ_s) are two important parameters used to find out the SWE. The snow water equivalent is a measure of the amount of water contained in a snowpack. This term is used in hydrology studies to predict snowmelt run-off. It is defined as:

$$SWE = d\,\frac{\rho_s}{\rho_w} \tag{4.1}$$

where d is the snow depth (m), ρ_s is the snow density (kg/m^3), and ρ_w is the density of water (kg/m^3) which is constant for a specific temperature.

As seen earlier, the total derived backscattering coefficient (σ°_{total}) for a layer with a distinct upper boundary at polarization "*pq*" is given by (4.2). This formulation which is known as the S^2RT/R model will be used to simulate the surface and the volume backscattering coefficients of snow over ground. Volume scattering is created by ice grains at the wavelengths comparable to the grain size.

$$\begin{aligned}\sigma^0{}_{total,pq} = {} & \mathrm{T}^2_{pq}(\theta_i)[\Upsilon^2_{pq}\sigma^0{}_{g,pq}(\theta_r) \\ & + 0.75a\cos\theta_r(1-\Upsilon^2_{pq})(1+\Gamma^2_g(\theta_r)\Upsilon^2_{pq}) \\ & + 6\kappa_s d\Gamma_g(\theta_r)\Upsilon^2_{pq}] + \sigma^0{}_{as,pq}(\theta_i)\end{aligned} \tag{4.2}$$

The I^{2}EM model is applied to simulate the ground surface backscattering coefficients under snow cover. Ground (soil) surface parameters such as surface rms height (s), correlation length (l), soil moisture (m_s), and autocorrelation function are used to compute the soil surface backscattering value ($\sigma^0_{g,\,pq}$).

The dielectric properties of snow are quite complex depending on several parameters such as frequency, temperature, snow density, and water content [70]. Snow density and wetness (m_v) will determine the penetration depth of the radar signal. In the retrieval method, we consider dry snow only. As we stated before, a layer of dry snow is a dielectric medium consisting of ice crystals in an air background. Wet snow is somewhat more complicated. Although most scatterers are non-spherical, when they are randomly oriented and distributed within a layer, they act like spherical scatterers.

4.3.1 Effect of Snow Wetness and Frequency

Penetration is a very important parameter for the remote sensing of snow. The possibility of information retrieval from the backscattered measured waves is dependent on how the EM wave is capable to penetrate a snow layer. It depends on the frequency of the incident EM wave as well as the dielectric constant of snow; that’s the liquid water content in snow. The more the liquid water content, the higher the dielectric constant, and therefore bigger absorption which means less penetration. That’s why wet snow attenuates the microwaves in a very short distance. The penetration depth (δ_p) is defined as [71]:

$$\delta_p = \frac{4\pi}{\lambda}\left(\frac{\varepsilon'}{2}[[1+(\frac{\varepsilon''}{\varepsilon'})^2]^{1/2}-1]\right)^{-1/2} \quad \text{(cm)} \tag{4.3}$$

If $\varepsilon''/\varepsilon' \ll 1$, (4.3) becomes:

$$\delta_p \approx \frac{\lambda\sqrt{\varepsilon'}}{2\pi\varepsilon''} \tag{4.4}$$

which can be used for dry snow and wet snow where the liquid water volume content is less than 2% [71, 72, and 73]. Figure 4-1 shows the variation of the penetration depth (δ_p) for a snow layer (ρ_s = 0.4 g/cm^3; r = 0.5 mm) as a function of liquid water content (m_v %) for frequencies in the microwave range. Snow physical parameters inversion algorithm at higher bands is more efficient, but Ku- band is more sensitive to shallow snow only, with a typical penetration depth of 3-4 m in case of dry snow. However, X-band provides greater penetration for deeper snow where the penetration depth is around 10 m.

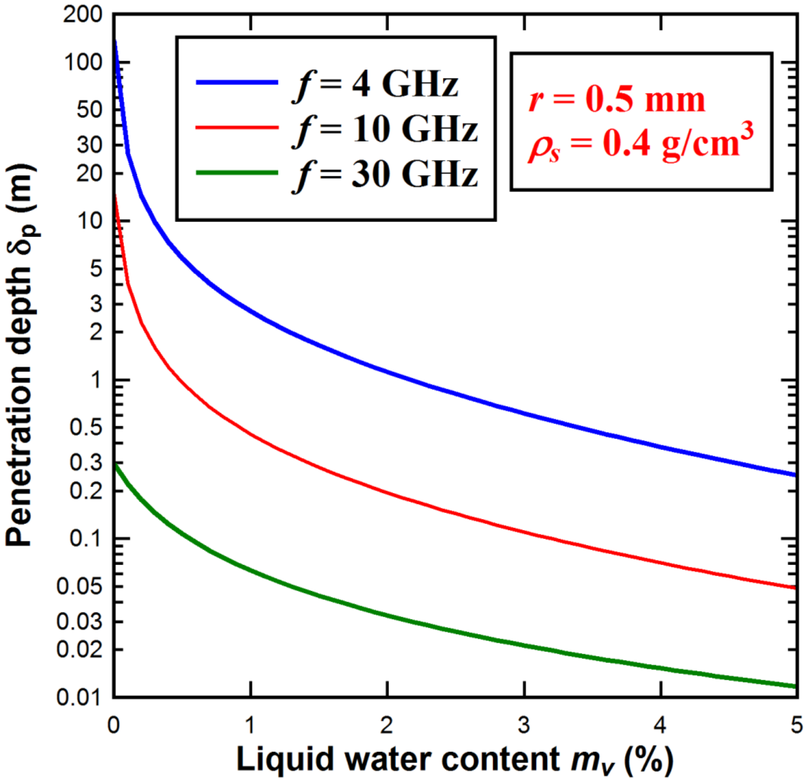

Figure 4-1: Penetration depth changes with the amount of liquid water content (m_v) at 4 GHz, 10 GHz, and 30 GHz for a 0.4 g/cm^3 snow density and 0.5 mm snow particle radius.

4.3.2 Absorption, Scattering, and Extinction Losses

The absorption (κ_a), scattering (κ_s), and extinction (κ_e) coefficients can be calculated in terms of the ice particle radius (r), frequency (f), temperature (T), and snow density (ρ_s). In the case where the size of inclusions is much smaller than the wavelength (λ), κ_s is much smaller than κ_a so that $\kappa_e \approx \kappa_a$. This is illustrated in Figure 4-2 where the plots of κ_s, κ_a, and κ_e are shown as a function of frequency for a dry snow medium with a density 0.476 g/cm^3 and spherical ice inclusions (r = 0.75 mm). This chosen density will be used in the application of the snow depth inversion algorithm because the median seasonal snow density over the 2-year period (2014-

2016) was 0.476 g/cm3 in Lebanon [74]. The absorption and scattering coefficients are basic parameters used in the radiative transfer model to compute the backscattering coefficient of a layer of snow over ground. The plots in Figure 4-2 are computed using MIE solution. The volume absorption coefficient increases as water content in snow increases, thereby no power is reflected, and hence the snow layer is not resolvable. This was illustrated well in Figure 4-1 which shows that a wet snow pack degrades the resolution of the radar by preventing reflection at higher frequencies.

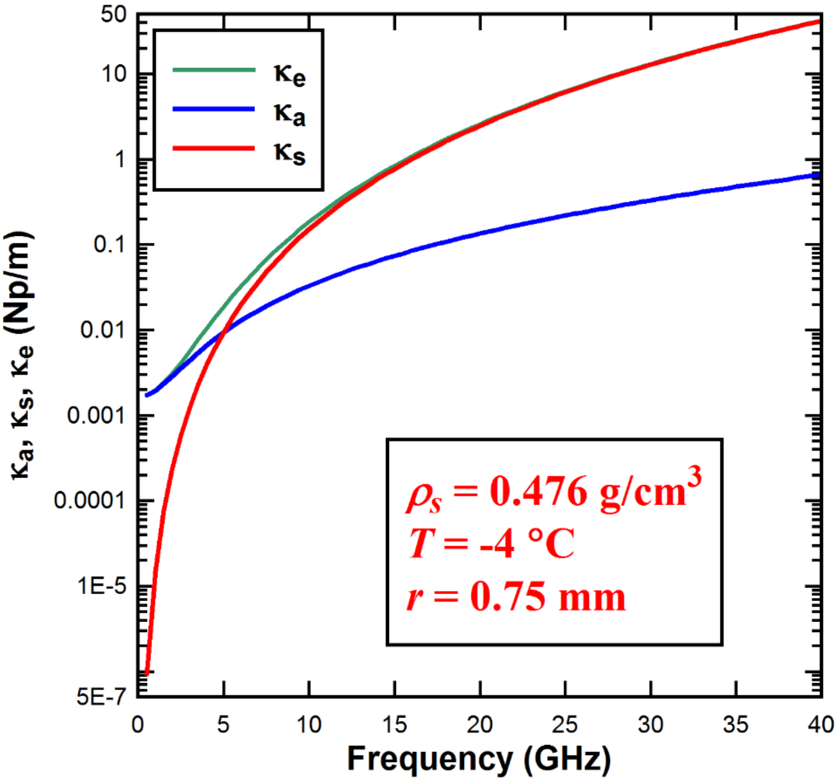

Figure 4-2: The MIE computed absorption, scattering and extinction coefficients for dry snow of density 0.476 g/cm^3 containing spherical ice particles with radius r = 0.75 mm.

Moreover, one of the most important parameters that influences the scattering calculations is the scattering albedo (a). The two most important factors that the albedo varies with are: the frequency (f) and the ice particle radius (r). Figure 4-3 shows the variation of the snow albedo as a function of frequency for two sizes of ice spheres. The albedo increases rapidly with increasing frequency for r = 2 mm and increases slowly for r = 0.75 mm. This is due to the fact that scattering losses are negligible at frequencies below 5 GHz (Refer to Figure 4-2); hence the albedo will be very small ($a = \kappa_s / \kappa_e$). On the other hand, at higher frequencies, scattering losses will dominate the absorption losses of the snow medium resulting in a higher albedo. When snow melts, the amount of liquid water in the mixture reduces the magnitude of the scattering albedo to a very small value ($\kappa_a > \kappa_s$). That's why wet snow is considered as a non-scattering medium.

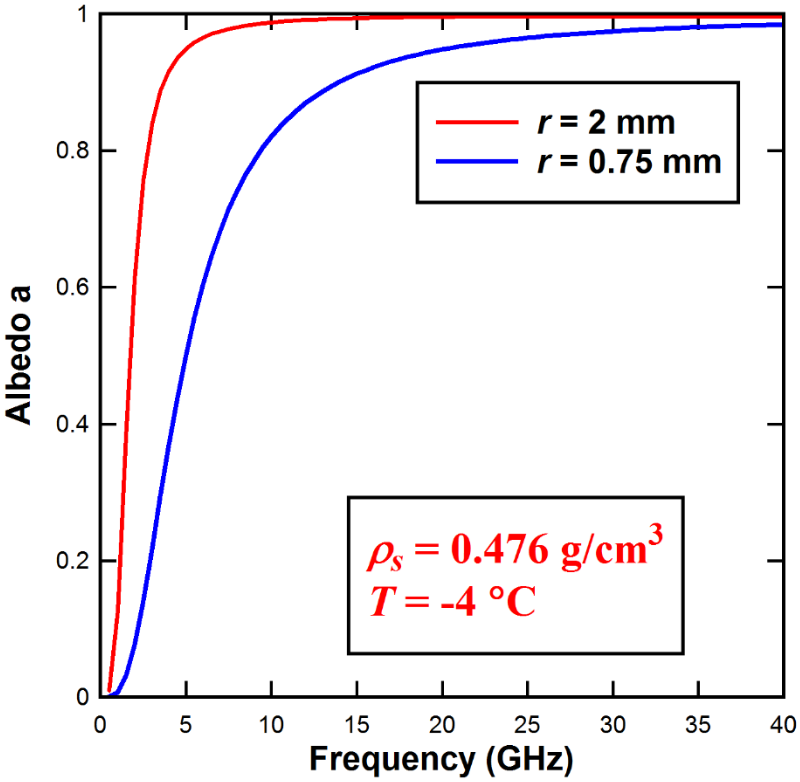

Figure 4-3: The calculated albedo (*a*) of dry snow as a function of frequency for two inclusion sizes.

4.3.3 Backscattering Behavior of Dry Snow

It can be useful to study the backscattering behavior of dry snow before the inversion process. The surface roughness of dry snow has almost no effect on the total backscattering coefficient due to the small dielectric contrast between air and dry snow ($\varepsilon_{air} = 1$ and $\varepsilon_{dry\_snow} = 1.9$ for a density of 0.45 g/cm^3). That's why $\sigma°_{as}$ could be neglected in the formulation given in (4.2). This is in contrast to the wet snow case because of the high dielectric losses of liquid water. Furthermore, it is necessary to study the angular dependence of the total backscattering coefficient because the retrieval algorithm is based on the variation of the incidence angle. As it can be seen from Figure 4-4, the backscattering coefficient decreases with increasing incidence angle. This is due to the decreasing backscatter from the ground under snow. For small incidence angles, surface scattering is the dominating contribution. For bigger incidence angles, volume scattering contribution becomes more significant. This is illustrated in Figure 4-5 where the total co-polarized backscattering coefficient is equal to the ground backscattering coefficient at angles less than 15°. As incidence angle increases, the ground backscattering coefficient decreases and the total backscatter reflects the volume contributions.

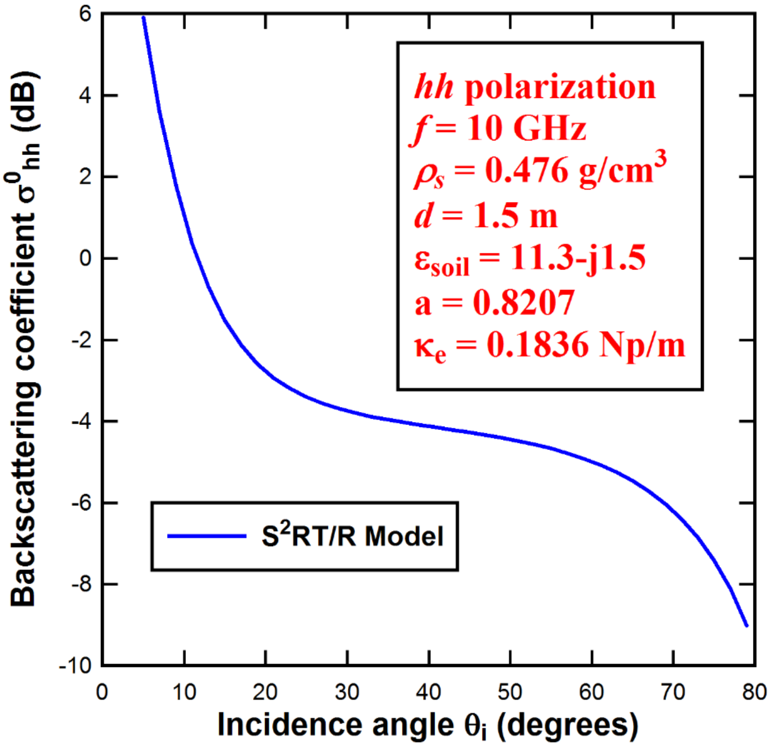

Figure 4-4: The calculated backscattering coefficient using the S^{2}RT/R model as a function of the incidence angle at H-polarization.

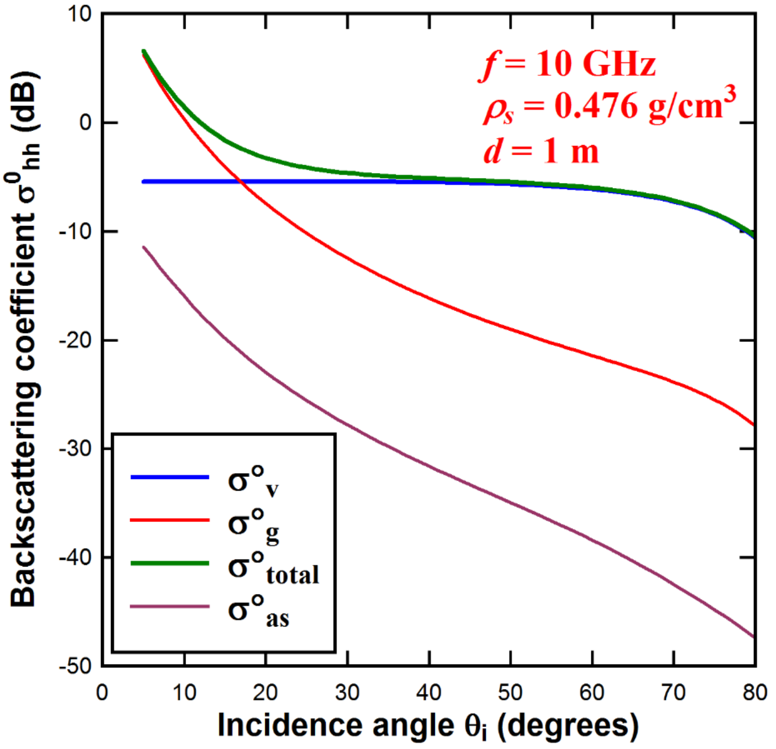

Figure 4-5: Computations of the co-polarized volume, soil, and total backscattering coefficients separately.

4.4 SIMULATION OF WHITE GAUSSIAN NOISE IN MATLAB

A zero-mean Gaussian noise with variance σ^2 is added to the theoretical values to form a statistical variation similar to that collected from a real radar. A white noise signal is generated using a random number generator where all samples follow a Gaussian distribution. A simulated White Gaussian Noise (WGN) with a mean (*mu*) and variance σ^2 is defined as:

$$Y = mu + \sigma * randn(1,L) \qquad (4.5)$$

where L is the sample length of the random signal. To choose a logic value of the noise variance so that our work would reflect real value measurements, the power spectral density (PSD) function of a sinc wave is plotted and compared with the PSD of a WGN. The variance is varied so that a value is chosen when there is a difference of more than 10 dB in the power between the two obtained PSD functions. This is illustrated in Figure 4-6 for a 0.02 noise variance.

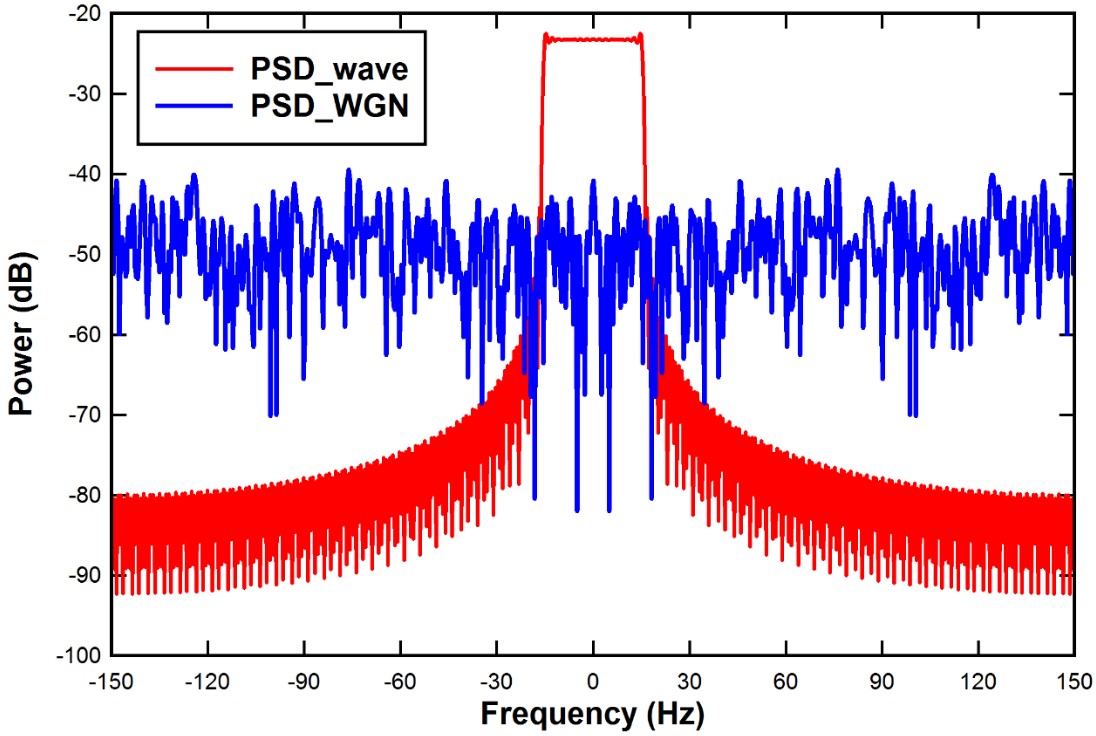

Figure 4-6: The power spectral densities of a sinc wave and a WGN with a variance of 0.02.

4.5 RETRIEVAL ALGORITHM

Now, by measuring the radar backscattering coefficients at different incidence angles and frequencies, it is possible to retrieve the snow parameters provided that we have forward microwave scattering models that relates the snow parameters to the microwave observations. This procedure is summarized in Figure 4-7.

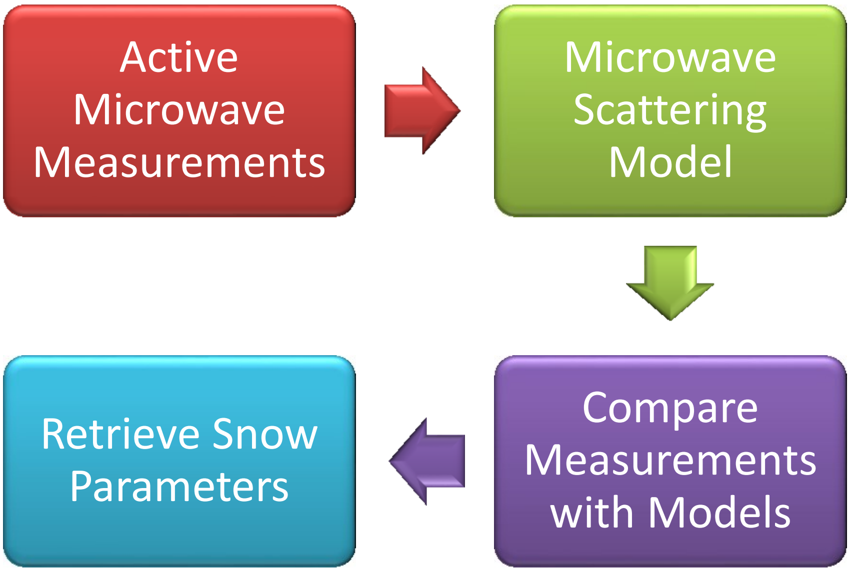

Figure 4-7: Flow chart of microwave remote sensing of snow.

Microwave snow scattering models are divided into three categories: semi-empirical models, physical based scattering models and numerical models. Semi empirical models have some limitations to snow conditions and are derived from measurement data. Physical models relate the backscattering coefficient with the geometrical structure of the snow: density, ice particle radius, depth, and liquid water content for various frequencies and polarizations. Numerical solution is called at high frequencies (above 12 GHz), and for snowpacks with large ice particles because the iterative solution method that solves the radiative transfer equation has an unreasonably accuracy.

4.5.1 Snow Density Estimation

The microwave response of snow covered ground is highly related to the snow grain size. Should these ice grains be too small, then the volumetric scattering drops to negligible in microwave; should these ice grains be too large, then the volumetric scattering will be too large for the microwave to effectively penetrate into the snowpack to provide information proportional to snow volume [75]. At L-band, volume scattering contributions have no significant effect on the total received signal. In this case, the total backscattering coefficient can be simplified to:

$$\sigma^0_{total} = \mathrm{T}^2_{pq}(\theta_i)\ \sigma^0_{g,pq}(\theta_r) \qquad (4.6)$$

where T_{pq} is the transmission from air to snow across the air-snow boundary and σ^0_g is the surface backscattering contribution from the snow-soil interface. For a horizontally polarized incident wave, T_{pq} is defined as:

$$\mathrm{T}_{hh} = 1 - \left| \frac{\cos\theta_i - \sqrt{\varepsilon'_{snow}} \cos\theta_r}{\cos\theta_i + \sqrt{\varepsilon'_{snow}} \cos\theta_r} \right|^2 \tag{4.7}$$

where θ_i denotes the incidence angle and θ_r denotes the refraction angle in the snow layer. Note that the expression of the I^{2}EM model assumes backscattering from an air - soil random rough surface. However, in our work, the ground is covered by a snow layer. That's why $\varepsilon_{soil}/\varepsilon_{snow}$ should be used instead of ε_{soil} and θ_r should be used instead of θ_i when calculating the snow - soil interface backscattering coefficient (σ^0_g).

Snell's law states that:

$$\sin\theta_r = \sin\theta_i / \sqrt{\varepsilon_{snow}} \tag{4.8}$$

Note that the snow density is related empirically to the effective permittivity of snow by Looyenga's semi-empirical dielectric formula [3, 76]:

$$\varepsilon_{snow} = 1 + 1.5995\rho_s + 1.861\rho_s^3 \tag{4.9}$$

At microwave frequencies, the absorption coefficient (the imaginary part of the dielectric constant) of ice is small, and snow grains are also small compared to an incident L-Band wavelength [3]. That's why snow is considered as a homogeneous mixture over a soil surface at L-band frequencies. So, the input variables used to find σ^0_{total} at L-band are:

- Frequency *(f)*
- Polarization *(pq)*
- Incidence angle *(θ_i)*
- Snow density *(ρ_s)* or *(ε_{snow})*
- Dielectric constant of the ground *(ε_{soil})*
- Rms height of the ground surface roughness *(s)*
- ACF of the ground surface roughness
- Correlation length of the ground surface roughness *(l)*

Measurements before snow fall can be done so that the dielectric properties of the ground as well as its roughness information can be retrieved. Many semi-empirical models were done to recover the values of the ground surface properties or they could be measured using a laser profilometer. After that, the only remaining unknown is ε_{snow} which is related to the snow density by an empirical formula. So, in our work, the parameters related to the ground surface are well known before snow fall. The values that were chosen in our forward theoretical simulation are summarized in Table 4-1. They are based on experimental data found in [7]. Then, the snow permittivity is solved using the non-linear equations (4.6), (4.7), and (4.8) by means of MATLAB. Then, the snow density is calculated using (4.9). Inversion approaches solve the inverse problem in a way that a priori information is taken into account. In snow permittivity inverse calculation, an initial guess of 1 is chosen because dry snow permittivity varies between 1 (permittivity of air) and 3.15 (permittivity of ice).

Table 4-1: Parameter Values Used in the Forward Theoretical Simulation at L-band.

Parameter	**Value**
Operating frequency f	2 GHz
Incidence angle θ_i	0°
Polarization pq	HH
Soil permittivity	$\varepsilon_{soil} = 11.3 - j\ 1.5$
RMS height s	0.6 cm
Correlation length l	25 cm
Autocorrelation function	ECF
Snow density range study	[0.25-0.5] g/cm^3 Interval: 0.05

A variance of 0.02 was tested for the addition of the noise due to the system measurement. The study was done over a range of snow densities from 0.25 to 0.5 g/cm^3. For each snow density, the HH-polarized backscattering coefficient is calculated and a Gaussian noise is added to the theoretical value to form a statistical variation as that in Figure 4-8. Then, the permittivity is solved using (4.3) and (4.4) for each value from the obtained histogram of the backscattering coefficient. Therefore, an estimate of the snow permittivity for a specific density is obtained by averaging the values of the new obtained histogram as shown in Figure 4-9. This procedure is done for all density values in Table 4-1 and a comparison is shown between simulated theoretical values and estimated values in Table 4-2. The percentage error histogram is presented in Figure 4-10.

Table 4-2: Comparison Between Forward Theoretical Values and Estimated Values at L-band.

Snow density (g/cm^3)	**ε_{snow}_theory**	**ε_{snow}_retrieved**	**ρ_s_retrieved**	**Density error in %**
0.25	1.4291	1.4236	0.2472	1.12 %
0.3	1.5303	1.5311	0.3004	0.13 %
0.35	1.6399	1.6416	0.3509	0.26 %
0.4	1.7592	1.7632	0.4016	0.4 %
0.45	1.8773	1.8763	0.4496	0.09 %
0.5	1.9983	2.001	0.5011	0.22 %

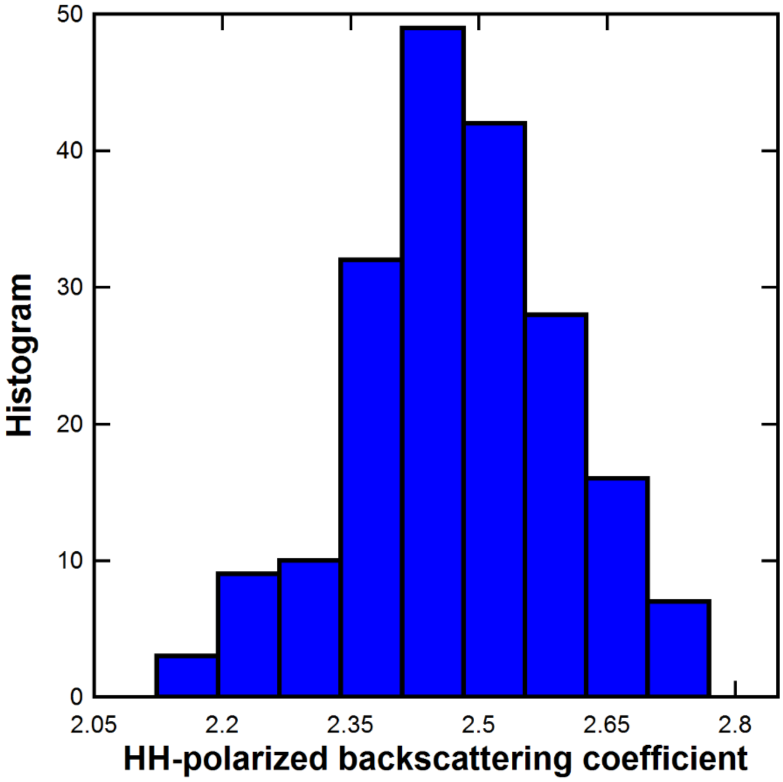

Figure 4-8: Statistical distribution of the HH-polarized backscattering coefficient for air-snow-ground for a snow density = 0.5 g/cm^3 with parameter values found in Table 4-1.

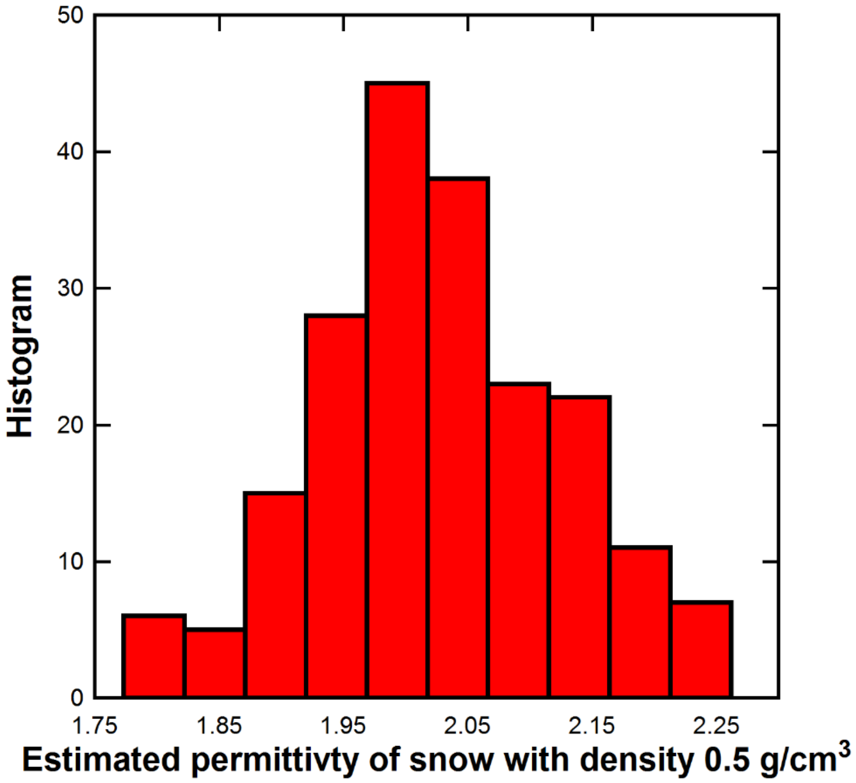

Figure 4-9: Histogram of the retrieved permittivity of snow with density = 0.5 g/cm^3 using the statistical distribution of the HH-polarized backscattering coefficient in Figure 4-8.

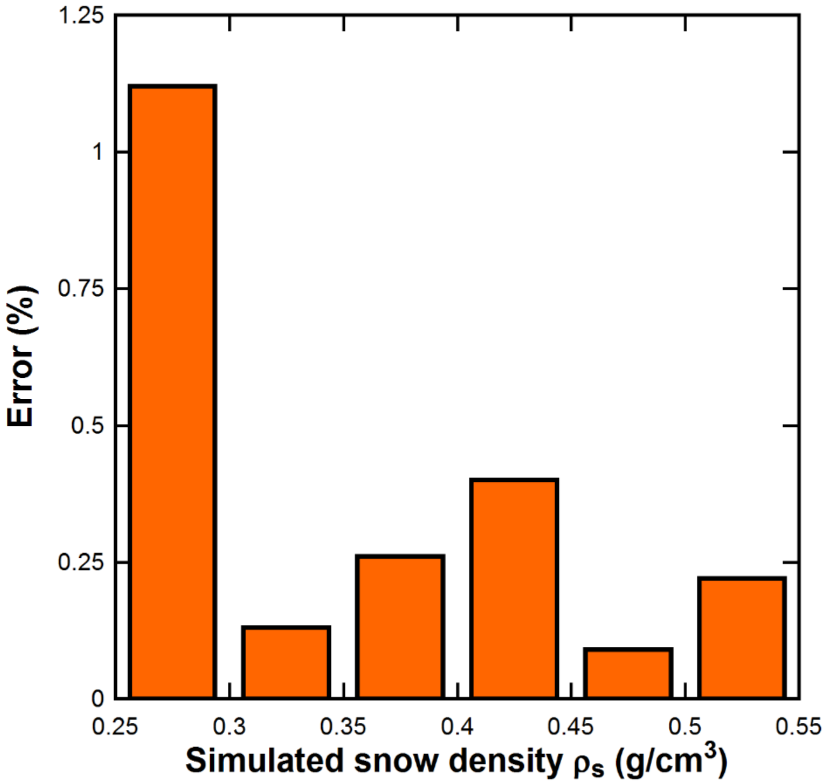

Figure 4-10: The error in % between estimated snow densities and simulated ones at L-band.

4.5.2 Snow Depth Estimation

As already said, volume scattering in the snow medium is mainly governed by the size of the ice crystals with respect to the wavelength. The bigger the snow particles, the higher the interaction of the EM wave with snow grains; hence the higher the volume scattering contribution. Therefore, increasing frequency makes the volume scattering coefficient more significant. In this section, the snow depth is retrieved using two different incidence angles from radar backscattering measurements at X-band. For higher frequency bands, parametrized models are used that have a simple form physically consistent with first-order model and outputs that include multiple scattering contributions. However, at X band, we have less effects of multiple scattering. So backscattering enhancement is of less importance at our chosen frequency.

Table 4-3: Parameter Values Used in the Forward Theoretical Simulation at X-band

Parameter	Value
Operating frequency f	10 GHz
Incidence angle θ_i	10° and 30°
Polarization	HH
Soil permittivity	$\varepsilon_{soil} = 11.3 - j\ 1.5$
RMS height s	0.6 cm
Correlation length cL	25 cm
Autocorrelation function	ECF
Snow density ρ_{snow}	0.476 g/cm^3
ε_{snow}	1.9396-j 2.5567e-04
Temperature T	-4°C
Snow depth d	[50-300] cm
Albedo a	0.8207
Extinction Coefficient κ_e	0.1836 Np/m
Ice particle radius r	0.75 mm

The backscattering signals at X-band or higher frequency band is more sensitive to snow parameters so the snow parameters inversion algorithm at these bands is more effective [77]. The frequency choice was based to meet Lebanon requirements where the snow height range study was [0 – 4] m in [74]. In our retrieval algorithm, the two chosen incidence angles were 10° and 30°. These two incidence angles were chosen so that there is a much difference between their output values for parameter values shown in Figure 4-4. This is can be easily observed when calculating σ^0_g at 10 GHz for the obtained snow density and soil surface parameters.

Typically, in real measurements, a variety of incidence angles could be observed so that the collected experimental backscattered data could be all tested in the snow parameters retrieval. This algorithm performs best at 10° and 30° for such ground properties. Table 4-3 summarizes all the values chosen in the forward theoretical calculation at X-band.

To retrieve snow depth, the density is calculated first using the previous procedure. Knowing the density, the refraction angle θ_r can be easily calculated from Snell's law and then T_{pq}, Υ_{pq}, and Γ_g can be computed. After replacing κ_s with $a \times \kappa_e$, the remaining unknowns in (4.2) are: the albedo (a) and the snow optical depth (τ) which is the product of the extinction coefficient (κ_e) and the snow depth (d):

$$\tau = \kappa_e d \tag{4.10}$$

The extinction coefficient is related to the albedo by:

$$\kappa_e = \kappa_a / (1 - \mathrm{a}) \tag{4.11}$$

where the volume absorption coefficient is defined empirically by:

$$\kappa_a = v_i k_0 \frac{\varepsilon_{ice}^{"}}{\varepsilon_{air}} \left| \frac{3\varepsilon_{air}}{\varepsilon_{ice} + 2\varepsilon_{air}} \right|^2 \tag{4.12}$$

where v_i is the volume fraction of ice ($v_i = \rho_s / 0.917$), ε_{air} is the permittivity of air which is close to 1 under all conditions, ε_{ice} is the permittivity of ice ($\varepsilon_{ice} = 3.15$), and ε''_{ice} is the imaginary part of the permittivity of ice and it is determined from snow temperature. The retrieval process can be summarized as follows:

1. Using dual incidence angles, the albedo and the snow optical thickness can be calculated using the non-linear relationship between the backscatter values and the snow parameters in (4.2) by means of MATLAB.
2. Calculate κ_a using (4.12).
3. Calculate κ_e using (4.11) with the estimated value of the albedo in step 1.
4. Finally, snow depth can be easily retrieved using (4.10).

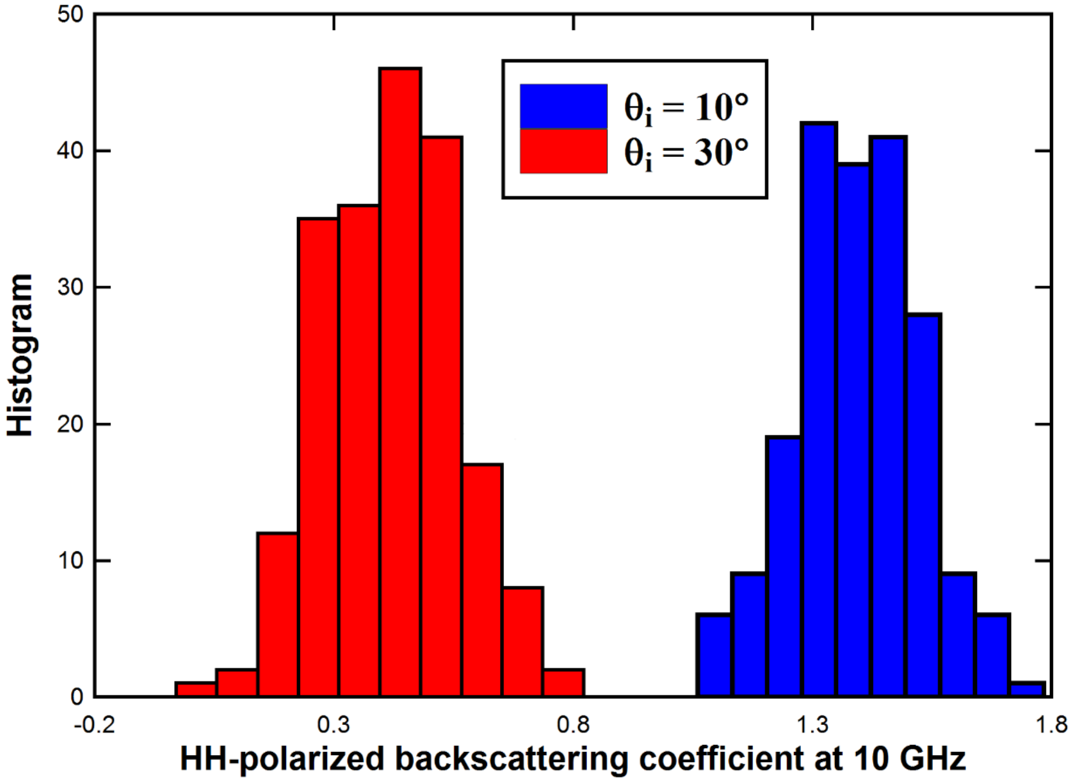

Figure 4-11: Statistical distribution of the HH-polarized backscattering coefficient from air-snow-ground for a snow density = 0.476 g/cm^3 and snow depth =1 m with parameter values found in Table III at θ_i=10 (Blue) and θ_i=30 (Red).

The previous procedure is done again where the HH-polarized backscattering coefficient is calculated for each snow depth value for two incidence angles, and a Gaussian noise is added to the theoretical value forming a statistical variation of σ^0_{total} as shown in Figure 4-11. Then, the albedo (*a*) and the snow optical depth (τ) are solved for each value from the obtained two histograms of σ^0_{total}. So, another two histograms will be obtained for '*a*' and 'τ' where their averages are just the estimated values of '*a*' and 'τ'. Finally, continuing in the procedure, snow depth can be easily estimated and a comparison is shown between simulated theoretical values and estimated values in Table 4-4. As it can be seen from Table 4-4, all retrieved snow depth values are in a well agreement with the simulated ones. Inversion approaches solve the inverse problem in a way that a priori information is taken into account. In the snow albedo and optical depth (a, τ) calculation, an initial guess of (0.9, 0) is chosen because dry snow albedo cannot exceed 1 and the optical depth is strictly greater than zero. The optimization flow chart is shown in Figure 4-12. Note that increasing the noise variance is just an increase in the error. Figure 4-13 represents the error between simulated and retrieved values where the error is less than 2% for all simulated snow depth values.

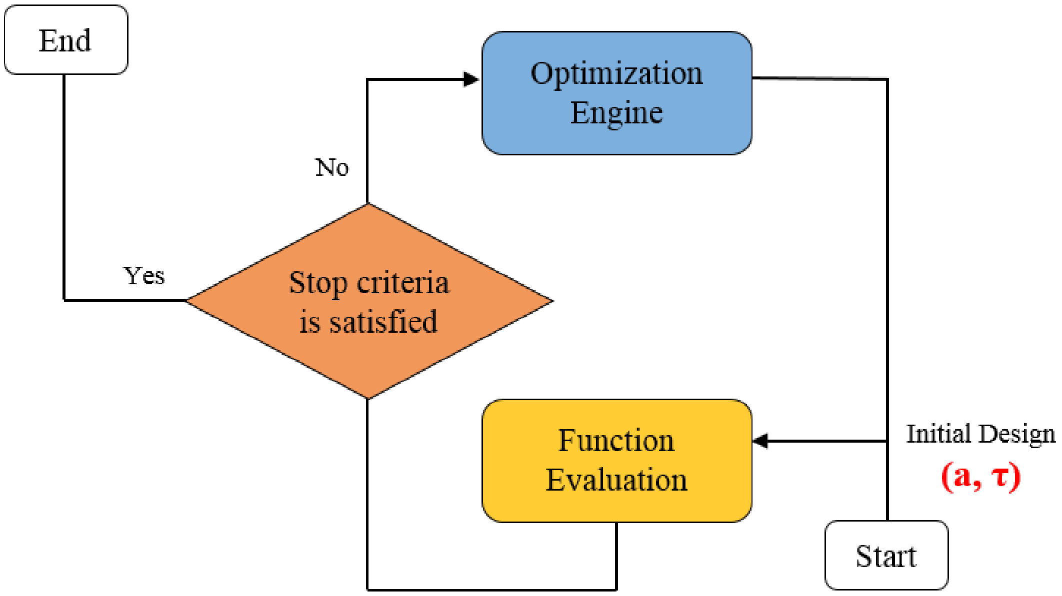

Figure 4-12: Optimization flow chart for the calculation of the albedo and the optical snow depth.

Table 4-4: Comparison between Forward Theoretical Values and Estimated Values at X-band

d (cm)	albedo 'a'	d-retrieved (cm)	a-retrieved
50	0.8207	48.91	0.8426
75	0.8207	74.59	0.8416
100	0.8207	100.61	0.8303
125	0.8207	125.30	0.8317
150	0.8207	150.97	0.8255
175	0.8207	176.45	0.8272
200	0.8207	203.59	0.8224
225	0.8207	223.46	0.8364
250	0.8207	248.34	0.8393
275	0.8207	276.42	0.8336
300	0.8207	302.56	0.8361

A graphical comparison between input data and estimated snow depth is shown in Figure 4-14. Table 4-5 lists the basic physical parameters required to retrieve snow depth with some basic explanations regarding the snowpack state and how each input parameter is obtained before the inversion process starts.

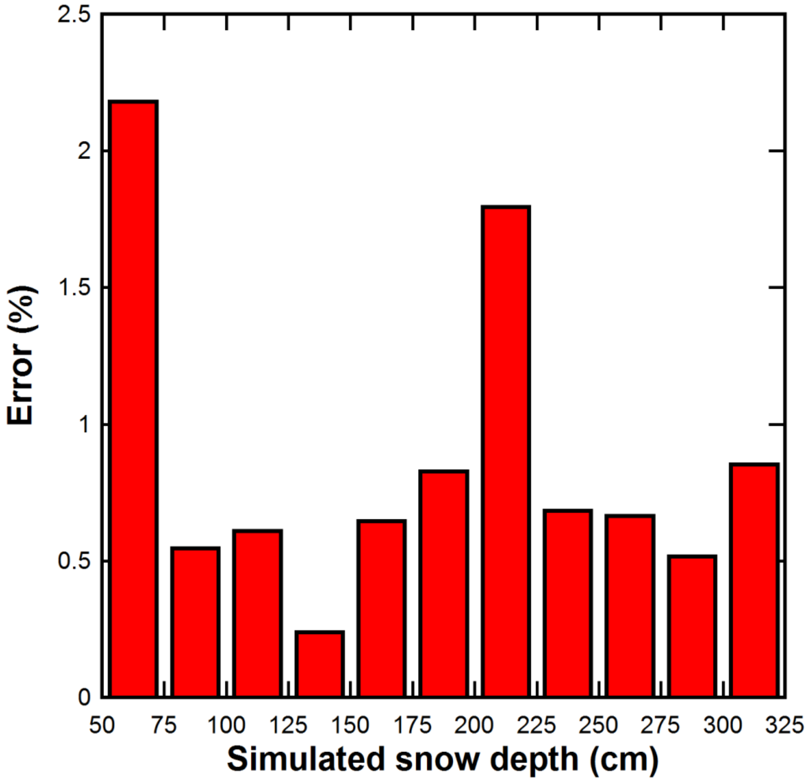

Figure 4-13: The error in % between estimated snow depths and simulated ones at X-band.

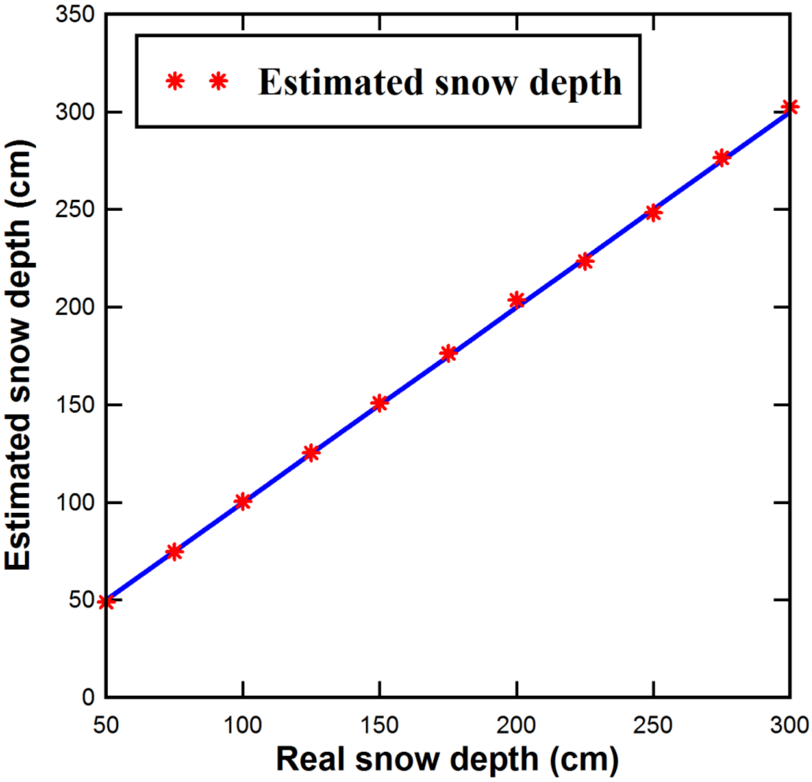

Figure 4-14: Comparison of the estimated snow depth using the previous algorithm with a 0.02 noise variance with real input data.

Table 4-5: Technical Information Regarding Snow Depth Retrieval

Parameter	**Name**	**Role in the Retrieval Method**	**Computation Way**
d	Snow Depth	Variable	Estimated from X-band backscattering observations
T °C	Snow Temperature	Used to compute the dielectric losses ε"	Estimated from weather station data
ρ_s	Snow density	Used to compute the dielectric constant ε'	Estimated from L-band backscattering observation
s_2, l_2	Roughness conditions of snow-ground interface	Used to compute σ^0_g	Laser Profilometer
κ_a	Absorption losses	Used to compute the extinction losses	Depends on frequency and temperature in a theoretical relation
κ_s	Scattering losses	Used to compute the albedo	Rayleigh scattering approximation
a	Scattering albedo	κ_s / κ_e	Estimated from X-band backscattering observations

4.6 SENSITIVITY OF SNOW THICKNESS ESTIMATES TO ERRORS IN SNOW DENSITY

Provided with a 10 GHz operating radar, the measured backscattering coefficient depends mainly on the snow density. Knowledge of the effective permittivity of snow is essential to accurately derive the snow layer thickness, hence it is necessary to measure the sensitivity of the radar to errors in estimates of the snow density.

Table 4-6 shows that there is an increasing error made in distance calculations as the error in the density estimation increases. The values in Table 4-6 show that for a dry snow pack a 20% error in density contributes approximately a 13.85 % error to snow thickness (for example, if the snow thickness is 100 cm, this is gives a 13.85 cm error in snow thickness).

Table 4-6: Error in Snow Pack Thickness Calculations as a Function of Error in Density for Dry Snow.

$\rho_s = 0.3$ g/cm^3	ρ_s	ρ_s + 10%	ρ_s – 10%	ρ_s + 20%	ρ_s – 20 %
ε_{eff} of snow	1.5303	1.6285	1.4389	1.7345	1.3532
Error in distance (%)	0	7.31 %	10.93 %	13.85 %	23.97 %

4.7 BACKSCATTERING BEHAVIOR OF WET SNOW

It is true that the air - snow interface roughness has a negligible effect on the total backscattering coefficient from snow covered ground when the snow layer is dry, but it has a significant impact on $\sigma°$ when the snow is wet. This is due to the fact that the dielectric permittivity of snow increases as liquid water increases in the snow medium. So, the Fresnel reflectivity of wet snow is larger than that of dry snow. Consequently, when constructing a backscattering model for wet snow, the upper snow boundary is treated as a rough surface, in contrast to the dry snow case in which it was regarded as a planar interface [7].

Moreover, the presence of liquid water in the snow medium causes an increase in the dielectric loss factor of the snow layer, ε''_{WS}. This increase in the dielectric loss factor causes an increase in the absorption coefficient; thus reducing the importance the scattering contribution from the ground surface. So, in case of wet snow, the snow-ground interface is assumed planar. These facts are illustrated in Figure 4-15 and Figure 4-16. The backscattering behavior of dry snow, snow-free ground, and wet snow for different amounts of liquid water content are shown in Figure 4-15. It is well significant to distinguish between dry and wet snow especially for high incidence angles because there is a large difference (≈ 10 dB) in the backscattering coefficient between dry and wet snow. As it was shown that the backscattering coefficient from the air - snow interface has no effect on the total backscatter from a dry snow layer, it is shown in Figure 4-16 that the total backscatter from snow covered ground is dominated by $\sigma°_{as}$ in case of wet snow for $m_v = 3\%$. Furthermore, the ground contribution $\sigma°_g$ is less than -40 dB and has no effect on the total microwave signature from the radar.

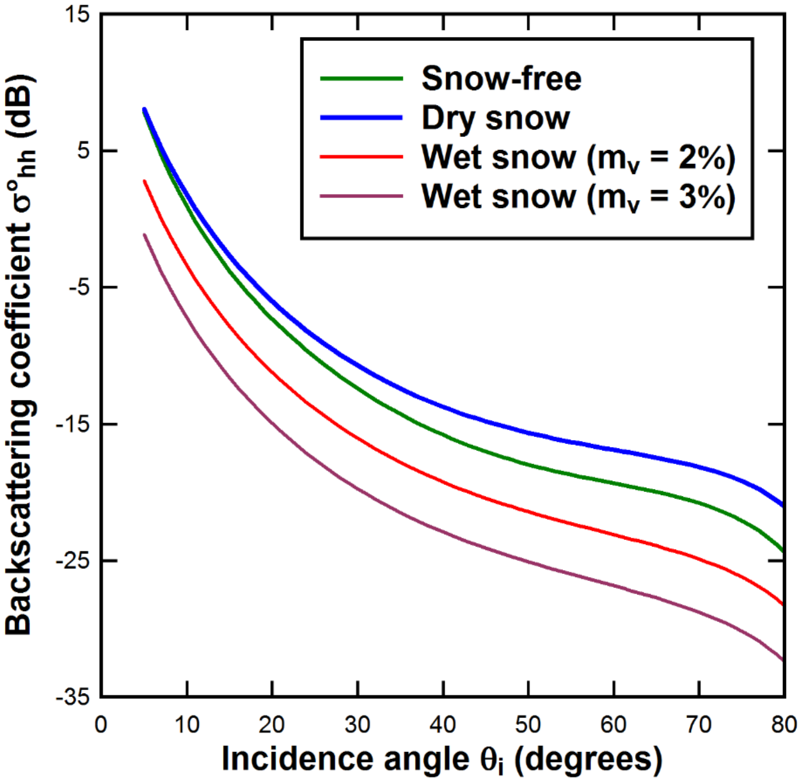

Figure 4-15: The hh-polarized backscattering coefficient in case of dry and wet snow.

Table 4-7: Model Parameters Used for Wet Snow Backscatter Study

Parameter	**Value**
Operating frequency f	10 GHz
Polarization pq	HH
Soil permittivity	$\varepsilon_{soil} = 11.3 - j\,1.5$
Snow wetness m_v	3%
RMS height of air-snow interface	$s_1 = 0.6$ cm
RMS height of snow-soil interface	$s_2 = 0.1$ cm
Correlation length of air-snow interface	$l_1 = 25$ cm
Correlation length of snow-soil interface	$l_2 = 2$ cm
Snow depth	0.1 m
Extinction Coefficient κ_e	10.8 Np/m
Dielectric losses ε''	0.1486
Dielectric constant ε'	1.6844

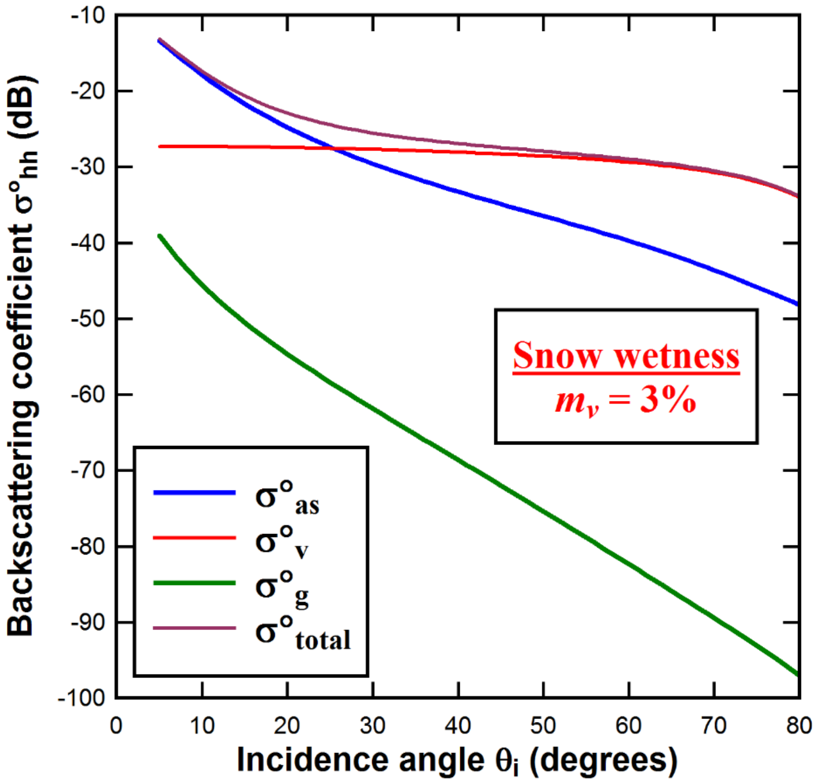

Figure 4-16: Computations of the co-polarized volume, snow-soil, air-snow, and total backscattering coefficient separately.

4.8 CLASSIFICATION OF WET SNOW AND DRY SNOW

When temperature increases, snow starts to melt resulting in a three-phase mixture of air, ice, and water. So, it is important for hydrological studies to detect snow melt. The best way to distinguish between dry and wet snow is summarized in the flow chart of Figure 4-17. It was verified in Figure 4-15 that there is a large difference between the backscattering coefficient between the bare ground and wet snow. Furthermore, a verification of this hypothesis should be done for different roughness conditions of the soil under the snow layer. All roughness conditions are summarized in Table 4-8.

Table 4-8: Parameter Values for the Ground Properties

Parameter	Range Values	Interval
Rms height	[0.1-0.6] cm	0.1
Correlation length	[5-25] cm	5

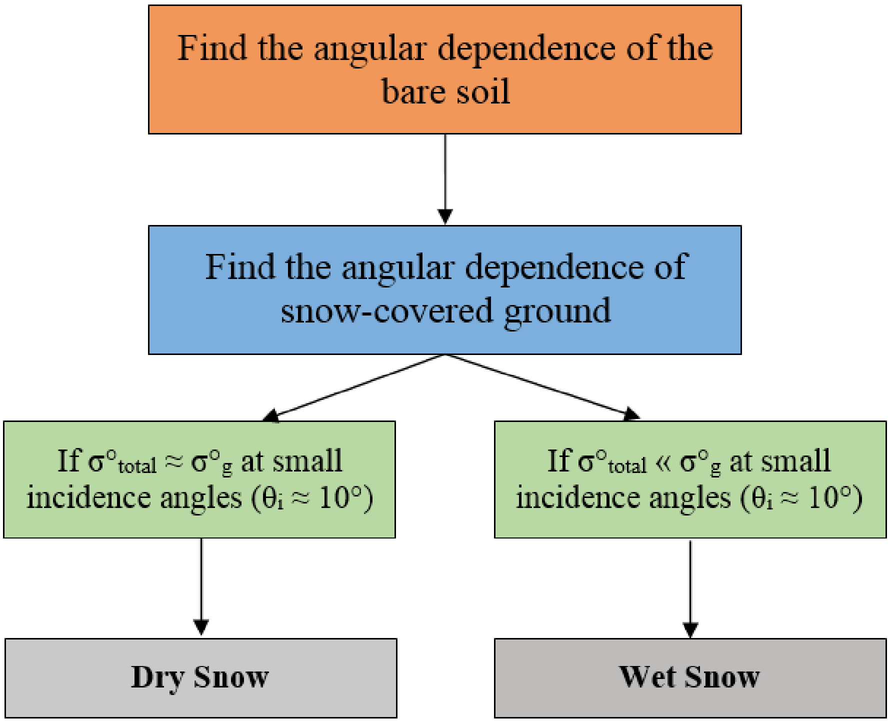

Figure 4-17: Flow chart used to discriminate between dry and wet snow.

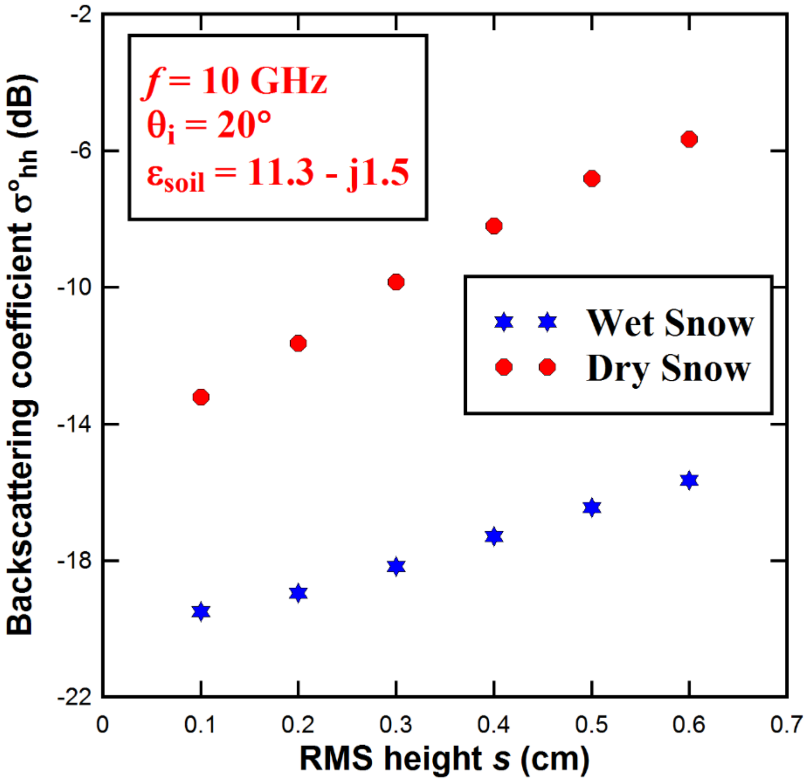

Figure 4-18: Comparison between the behavior of dry and wet snow for different values of the rms height of the ground surface.

As it can be seen from Figure 4-18 and Figure 4-19, the large difference between the backscatter behavior of dry and wet snow is still achieved for different values of rms heights and correlation lengths at incidence angle $\theta_i = 20°$ so that the discrimination between them can be well defined.

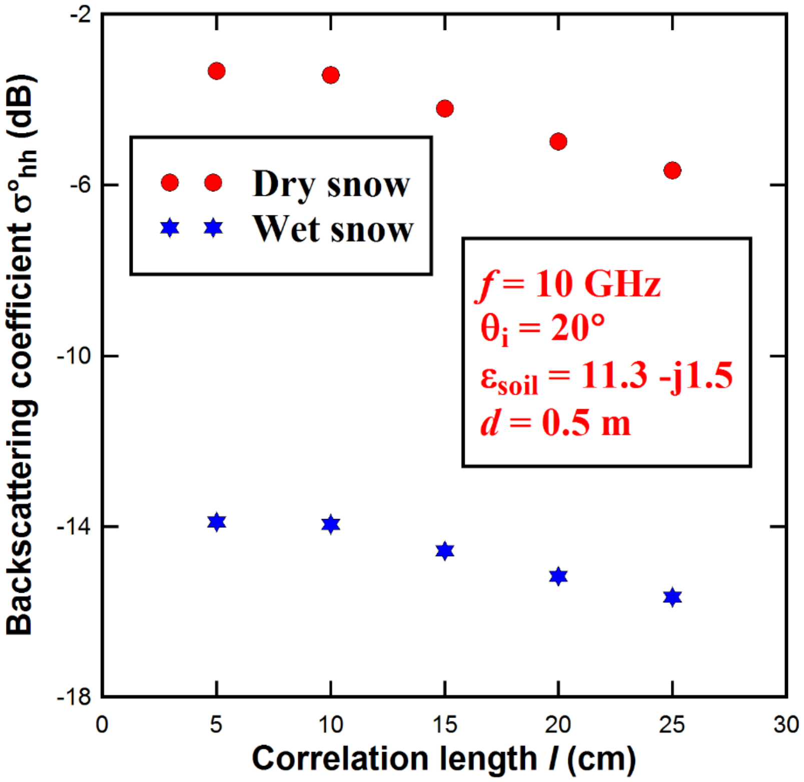

Figure 4-19: Comparison between the behavior of dry and wet snow for different values of the correlation lengths of the ground surface.

4.9 RADAR DESIGN AND VERIFICATION IN SYSTEMVUE

Modern radar systems that operate in environments with strong clutter, noise and jamming require advanced digital signal processing techniques [78]. Direct analysis techniques often fail when designing such complex systems. Although simulation is often used, most simulation tools do not have enough models and integration capability to handle modern radar systems [78]. SystemVue provides an effective and efficient environment for algorithm creation.

SystemVue is a multi-domain modeling implementation and verification cockpit for electronic system-level (ESL) design [79]. It is the shortest path from imagination to verified hardware for radar system designs by allowing the creative modeling of a radar system from transmitter to receiver including jamming and added clutter as shown in Figure 4-20. An extensive radar function library exists with models for transmit signal generation, the transmit antenna, the target, the receiver channel and antenna, enabling the investigation of various systems. SystemVue is a time domain simulator, however, the powerful sink calculator of SystemVue allows frequency domain analysis of the signals.

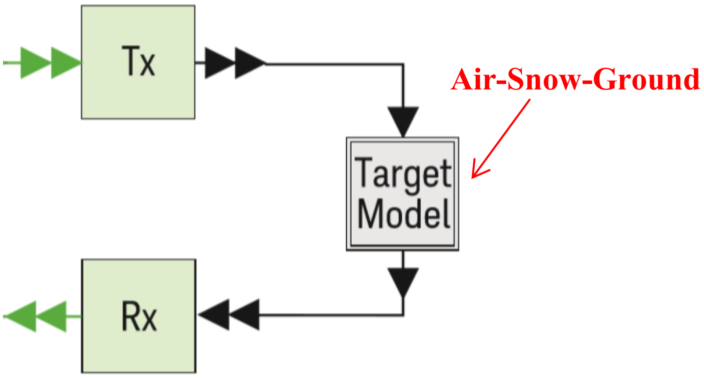

Figure 4-20: Stages for simulation in SystemVue.

Agilent SystemVue provides a very flexible platform for implementing complex aerospace and defense systems such as radar. With its unique “Envelope” simulation technology, for example, all aspects of system design, including RF and digital sub-systems, can be handled easily. Some of the other key benefits of SystemVue for the design and test of complex aerospace and defense systems are [80]:

- Its RF architecture capability allows for quick and accurate RF system design, while its budget analysis capability helps fine tune and optimize the RF system performance.
- A unique Real-Time Tuning and Sweep feature allow any parameter to be varied and its effect on system performance quickly analyzed.
- It enables a complete fixed-point digital implementation, whereby real DSP (Digital Signal Processing) systems can be designed and bit-true and cycle accurate fixed-point VHDL or Verilog codes can be generated automatically for FPGA implementations.
- It provides a seamless integration with instruments like signal analyzers, scopes, and logic analyzers that can be used to create and download standard or custom test vectors for complex system verification. Data from the device-under-test can also be captured and brought into software to design the system’s signal processing section or for RF system design and optimization.
- It provides direct integration with third-party digital/DSP tools such as ModelSim, Matlab and C++. Integrating such tools/third-party IP into one platform enables complete system design and validation.

4.9.1 SystemVue as a Platform for Simulation

The top-level system platform structure is shown in Figure 4-21. From the block diagram, the main models include signal source, transmitter, antenna, Matlab script model, receiver, signal processors, and measurements.

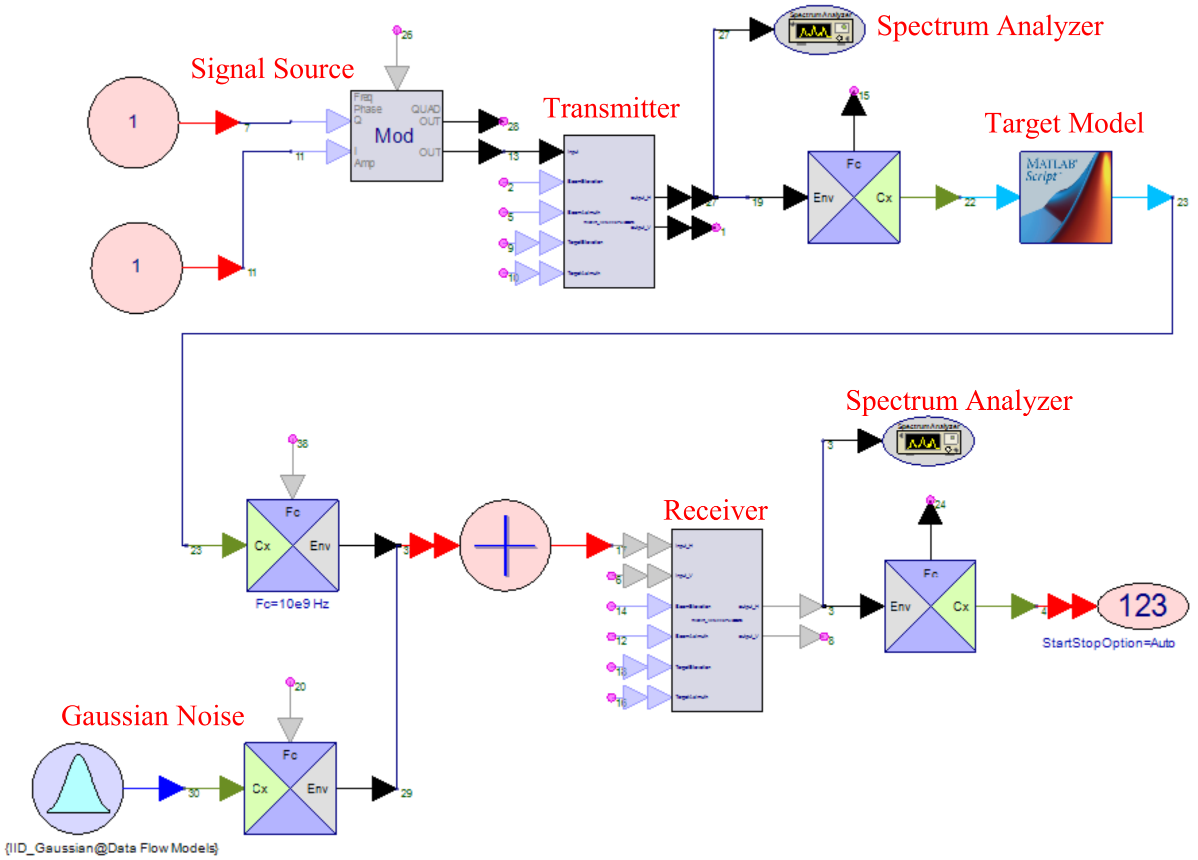

Figure 4-21: SystemVue scenario simulation.

4.9.2 Signal Generation

A dataflow design is shown in Figure 4-22 consisting of an input voltage and a modulation scheme. Once the data has been received on the "Mod's" input, the block performs its intended function on the data (modulation in this case) and outputs to its output node where the data will travel to the transmitter antenna.

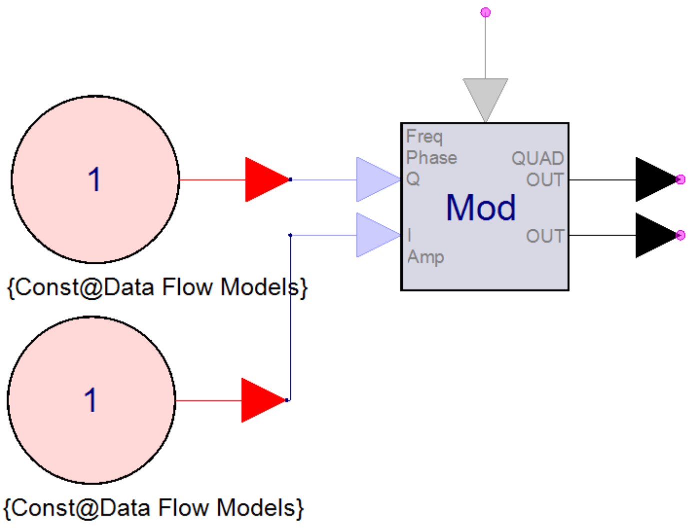

Figure 4-22: Signal generation in SystemVue.

4.9.3 Antenna Transmitter Setup

A transmitter is a radio system that converts baseband data into an RF signal and then transmits it through a communication channel, commonly using an antenna. An antenna Tx model is used to specify antenna beam angles, as well as target direction (in degrees) for both azimuth and elevation angles as seen in Figure 4-23.

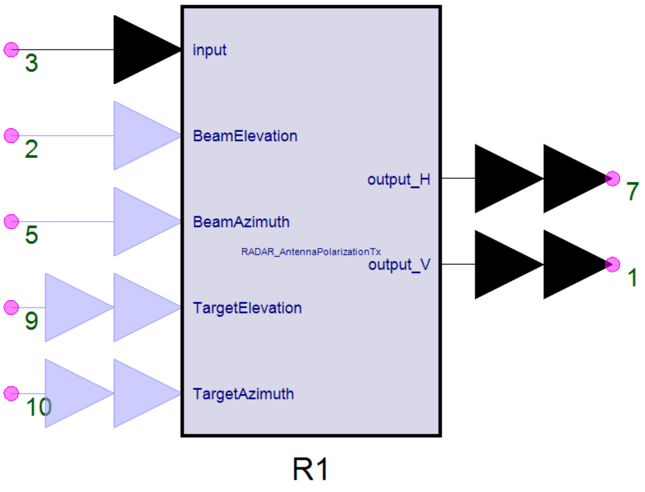

Figure 4-23: Radar_AntennaPolarizationTx

This model is aimed to load Antenna pattern from EMPro 3D EM Simulation Software and use it for antenna simulation, and it supports two working modes: search and tracking. The output_H is the horizontal polarization output signal of antenna in the Tx chain and the output_V is the vertical polarization output signal of antenna in the Tx chain. The User defined antenna pattern supports two file formats: one is Keysight EMPro file format and the other is Ansys HFSS file format. Figure 4-24 shows how to generate the antenna pattern with

Radar_AntennaPolarizationTx model. (Radar_AntennaPolarizationRx is another model which is used at the receiver).

Keysight's SystemVue is a data flow modeling software designed for baseband and high frequency simulations [81]. SystemVue includes an "envelope" datatype that requires a center/carrier frequency and the frequency components around the center frequency [82, 83]. The generated antenna RF signal needs a down conversion to form the complex signal to create the communication channel model. RF signal in SystemVue is defined as an envelope signal, whereas a baseband signal is considered a complex signal.

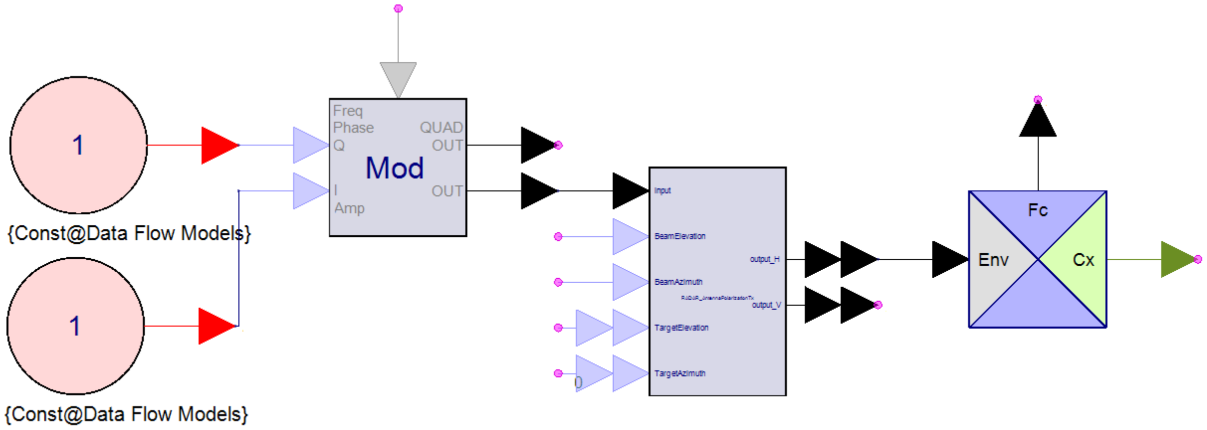

Figure 4-24: Transmitter design in SystemVue.

4.9.4 Communication Channel Model

SystemVue provide users the option to create custom models by using the built-in MATLAB interface. Users can use the SystemVue Radar Target model to specify target range, velocity and radar cross section models. However, modeling snow in this simulator is much more complex. The propagation medium is characterized by a MATLAB model as shown in Figure 4-25. A function is written in the simulator that represents the properties of air – snow - ground multilayered media concerning the snow albedo, snow density, snow depth, extinction coefficient, and the properties of ground (dielectric properties and roughness). It relates the input power to the output power using the model parameters so that this function will be used to represent the snow model. This developed medium depends on the electromagnetic frequency, Beam Elevation, and Beam Azimuth of the transmitter antenna as well as the snow properties. This simulation attempts to simulate the real behaviour of the snow and ground characteristics. The output of the target model needs an up conversion to form the RF signal for the receiver. The CxToEnvelope component defines the complex waveform as an RF Envelope waveform where the carrier frequency is defined.

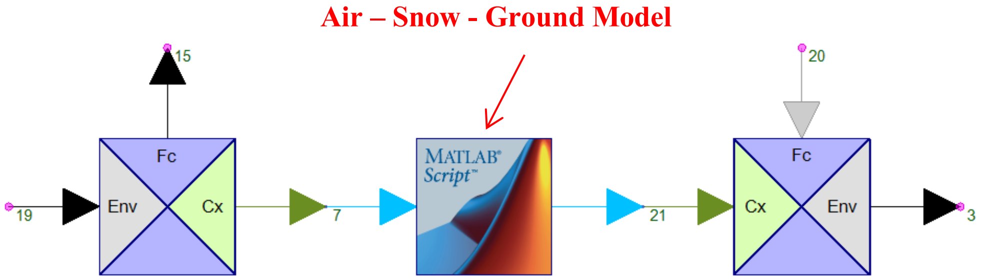

Figure 4-25: Snow target model in SystemVue.

4.9.5 Antenna Receiver Setup

The receiver signal can be used to test radar receiver detection algorithm. A Radar_AntennaPolarizationRx is a model used at the receiver as shown in Figure 4-26. At each point where the signal will be observed, a sink needs to be added. In the case of the radar, the signal is down-converted.

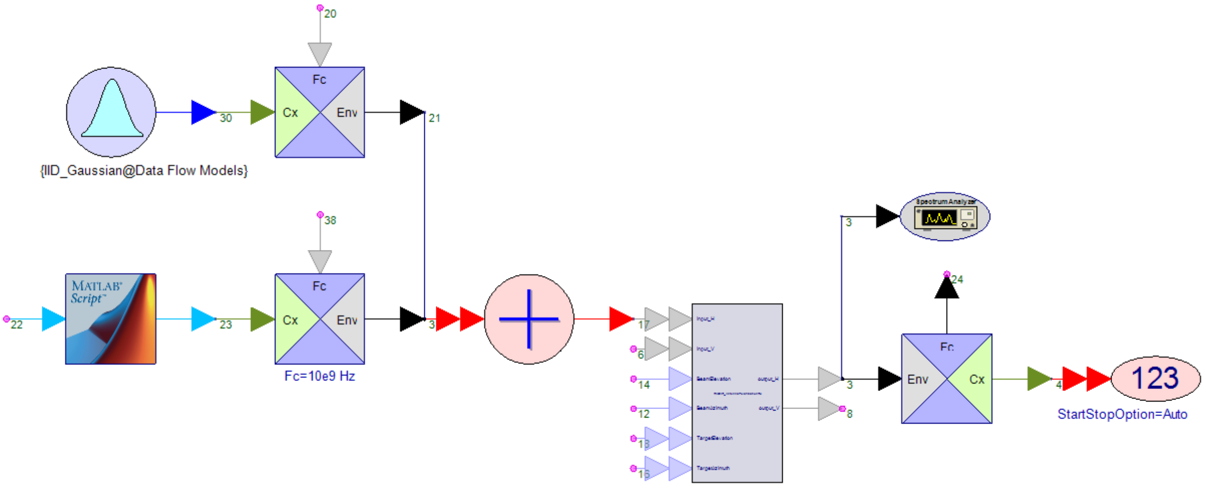

Figure 4-26: Receiver antenna setup.

4.9.6 Results and Discussion

Simulations are done using the platform shown in Figure 4-21 in SystemVue. The snow model is built using a MATLAB script where its thickness is varied from 50 to 300 cm. The Gaussian noise is added in the system with a variance of 0.02. Figure 4-27 shows the input power (P_{in}) measured at the transmitter antenna using a spectrum analyzer. Figure 4-28 shows the output power (P_{out}) measured at the receiver antenna after the addition of a gaussian noise in the simulation setup when $\theta_i = 30^o$ and $d = 50$ cm. Using these two calculated powers, the backscattering coefficient can be calculated for two different incidence angles; hence, snow depth can be retrieved based on our created algorithm in the previous sections.

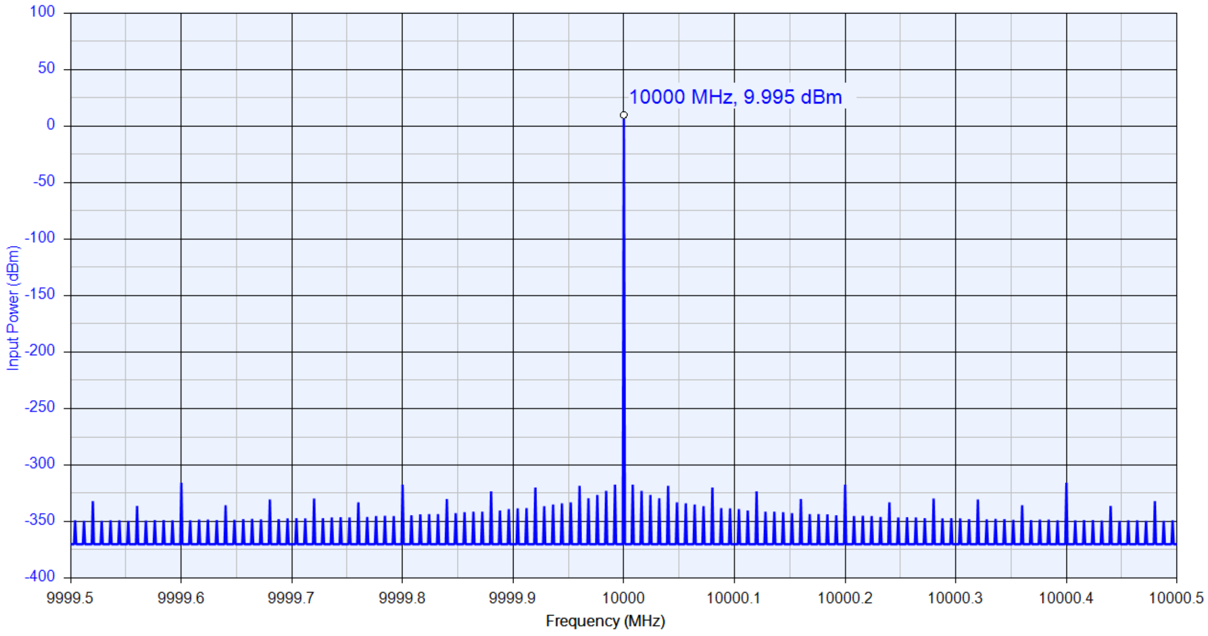

Figure 4-257: Input power spectrum.

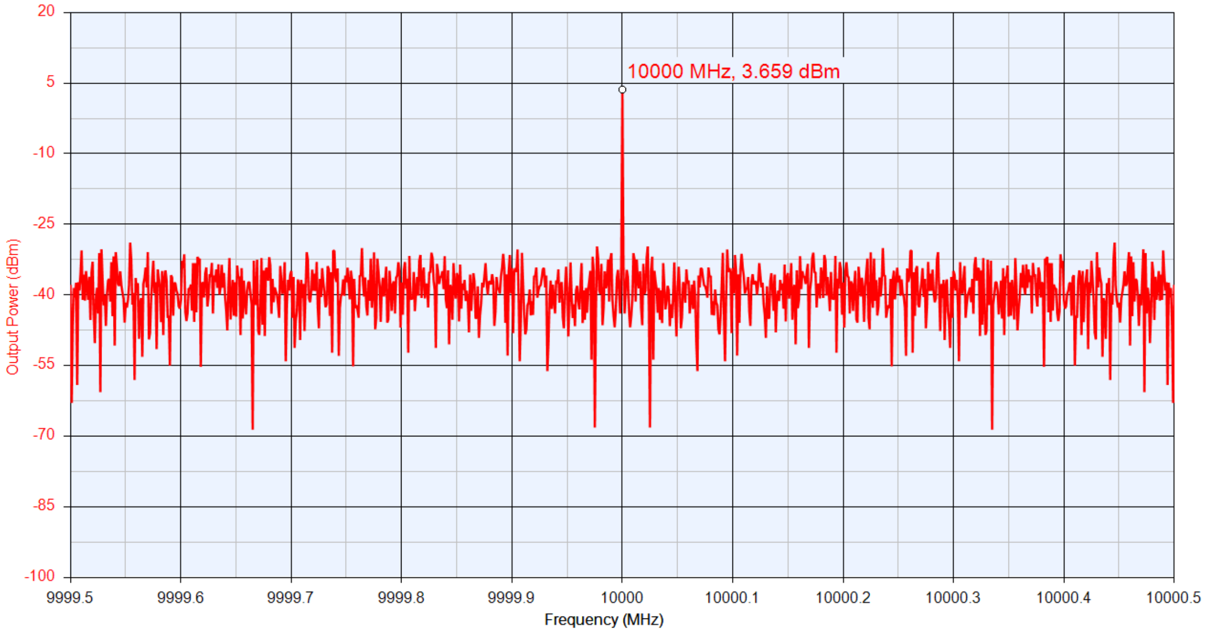

Figure 4-28: Output power spectrum.

Table 4-9: Snow Pack Thickness Calculation Results Using SystemVue.

Input Snow Depth (cm)	P_{in} (dBm)	P_{out} (dBm) at $\theta i = 10^o$	P_{out} (dBm) at $\theta_i = 30^o$	Retrieved Snow Depth (cm)
50	9.995	11.55	3.659	47.43
100	9.995	11.265	5.333	98.02
150	9.995	10.982	6.242	148.36
200	9.995	10.703	6.792	199.09
250	9.995	10.433	7.141	249.43
300	9.995	10.174	7.364	299.83

The snow thickness calculation results are shown in Table 4-9 where the same error is achieved using Monte Carlo simulations in Matlab and electronic simulations in SystemVue. So, the proposed algorithm is well verified in an electronic software that has a shortest path from imagination to verified hardware for systems design. Now, the only left step is the verification of this algorithm using real measurements.

4.10 CONCLUSION

In this chapter, a snow depth retrieval algorithm was presented based on backscattering measurements at L- and X-band using multi-incidence angles. The algorithm requires a priori knowledge of the dielectric and roughness properties of the ground. Calculations were done using Monte Carlo simulations in Matlab where estimated values were in an excellent agreement with simulated ones. Then, the retrieval method was verified in an electronic software where a schematic of a transmitter – target model – receiver was built in SystemVue. The comparison of retrieved values with simulated ones shows an error of less than 2% for a 0.02 noise variance. Our future work is to validate this algorithm experimentally with the use of a MIMO radar.

Conclusion

Snow cover is an integral component of the global climate system making the demand for the estimation of its physical properties very important. Snow monitoring has been an interesting research topic for both the scientific and the remote sensing community, due to the important role of the snow-pack in the hydrological cycle and its many derivative applications for hydrology, meteorology and climate study.

This thesis presents an efficient approach to the understanding of electromagnetic wave propagation and scattering in layered heterogeneous media with rough interfaces. In the frame of this work, a set of numerical simulations are accomplished that allows to calculate the snow density and the backscattering coefficient of air – snow – ground media. These simulations rely on the use of Ansoft's HFSS electromagnetic software which solves Maxwell's equations based on the finite element method. A step-by-step procedure to extract the effective permittivity -or density- of dry and wet snow at 2 GHz was the first presented numerical approach in this thesis. The permittivity values were extracted from the transmission coefficient with the help of Matlab showing a best fit with Looyenga's snow model. As a second step in the numerical validation of physical forward models, the study is developed to calculate the backscattering coefficient of the air – snow – ground system taking into consideration the roughness conditions of the ground layer and the heterogeneity of snow separately. The numerical calculated surface backscattering contribution at frequency 3 GHz was compared with predictions of surface scattering models showing a good agreement with the improved integral equation model (I^2EM). The volume backscattering coefficient results shows an excellent agreement with the S^2RT/R model at frequency in the X-band spectrum (9 GHz). These results are of particular interest since these done numerical approaches give the ability for the choice of the best physical forward models to use in the proposed snow depth retrieval algorithm at the required incident frequencies. It was found that the roughness of the ground as well as the volume scatterers in the snow are the dominant determinants in the effectiveness of the snow depth estimation in the radar.

The second main objective of this thesis was to investigate the possibility of measuring snow thickness over ground based on multiple radar backscattering observations. This requires an implementation of a MIMO (multiple input multiple output) radar which has the potential to operate at two frequencies and can scan multiple incidence angles simultaneously. The design of this sensor was not done throughout this thesis. So, calculations were performed using Monte Carlo simulations in Matlab where the addition of a white gaussian noise was just to reflect a similar data collected from a real radar. The backscattering coefficient was modeled by a statistical histogram obtained after the addition of a WGN with a variance of 0.02. This inverse scattering problem requires the estimation of the snow density first using L-band co-polarized backscattering measurement. Then, snow depth is retrieved from X-band radar backscattering coefficients using two different incidence angles. However, the complexity of advanced radar systems puts added focus on the radar signal processing algorithms which are critical to their development. Creating these algorithms requires generation of test signals. When used with the SystemVue environment, this application provides the basic information needed to create the required test signals earlier in the design cycle, facilitating early hardware verification and demonstrating the validity of the proposed retrieval algorithm. That's why our algorithm was tested by simulating using Agilent's SystemVue electronic system level design software demonstrating that the radar was able to retrieve snow thickness with an error less than 2 % for a 0.476 g/cm^3 snow density and snow depth range values [50-300] cm.

For the future, the implementation of the MIMO radar for snow applications can be accomplished based on the specifications needed for our proposed algorithm to validate the results experimentally. With the use of this sensor design, the retrieval method can be used as an application in climate system for an estimation of the amount of snow fall during the winter and for the detection of snow melt during the spring season.

Bibliography

[1] Barnett, T. P., Adam, J. C., & Lettenmaier, D. P. (2005). Potential impacts of a warming climate on water availability in snow-dominated regions. *Nature*, *438*(7066), 303.

[2] Cui, Y., Xiong, C., Lemmetyinen, J., Shi, J., Jiang, L., Peng, B., & Hu, T. (2016). Estimating Snow Water Equivalent with backscattering at X and Ku band based on absorption loss. *Remote Sensing*, *8*(6), 505.

[3] Shi, J., & Dozier, J. (2000). Estimation of snow water equivalence using SIR-C/X-SAR. I. Inferring snow density and subsurface properties. *IEEE Transactions on Geoscience and Remote Sensing*, *38*(6), 2465-2474.

[4] Koskinen, J. (2001). *Snow monitoring using microwave radars*. Helsinki University of Technology.

[5] Hallikainen, M., Ulaby, F., & Abdelrazik, M. (1986). Dielectric properties of snow in the 3 to 37 GHz range. *IEEE transactions on Antennas and Propagation*, *34*(11), 1329-1340.

[6] Cumming, W. A. (1952). The dielectric properties of ice and snow at 3.2 centimeters. *Journal of Applied Physics*, *23*(7), 768-773.

[7] Ulaby, F. T., Long, D. G., Blackwell, W. J., Elachi, C., Fung, A. K., Ruf, C., & Van Zyl, J. (2014). *Microwave radar and radiometric remote sensing* (Vol. 4, No. 5, p. 6). Ann Arbor: University of Michigan Press.

[8] Cheng, D. K. (1993). Fundamentals of engineering electromagnetics.

[9] Fitzpatrick, R. (2010). Maxwells Equations and the Principles of Electromagnetism. Laxmi Publications, Ltd...

[10] Balanis, C. A. (1999). *Advanced engineering electromagnetics*. John Wiley & Sons.

[11] http://emlab.utep.edu/ee5390em21.htm.

[12] http://www.nrcan.gc.ca/earth-sciences/geomatics/satellite-imagery-air-hotos/satellite-imagery-products/educational-resources/9575.

[13] http://www.ansoft.com/produxts/hf/hfss/

[14] http://edadocs.software.keysight.com/display/empro201101/Understanding+the+Process+of+FEM+Simulation.

[15] Song, K., Zhou, X., & Fan, Y. (2012). Electromagnetic scattering from a multilayered surface with lossy inhomogeneous dielectric profiles for remote sensing of snow. *Progress In Electromagnetics Research*, *25*, 197-209.

[16] *HFSS Field Calculator Cookbook*, Ansoft Corp., 2000, pp. 1-3.

[17] Remski R., "Advanced HFSS Training: The Field Calculator," *Remote Sensing Exploitation Division,* 18-21, Ansoft Corporation.

[18] Mossotti, O. F. (1850). Discussione analitica sull'influenza che l'azione di un mezzo dielettrico ha sulla distribuzione dell'elettricità alla superficie di più corpi elettrici disseminati in esso. *Memorie di Matematica e di Fisica della Societa Itlaiana delle Sceinze*, (Modena), Parte seconda, pp. 49-74.

[19] Clausius, R. (1879). Die mechanische behandlung der electricität. Abschnitt III (F. Vieweg, Braunschweig).

[20] Lorenz, L. (1869). Experimentale og theoretiske undersøgelser over legemernes brydningsforhold. *Det Kongelige Danske Videnskabernes Selskabs Skrifter, Naturvidenskabelig og mathematisk afdeling*, Femte Raekke, Ottonde Bind, (8), pp. 205-248.

[21] Lorenz, L. (1880). Ueber die refractionsconstante. *Annalen der Physik*, *247*(9), 70-103.

[22] Lorentz, H. A. (1880). Ueber die Beziehung zwischen der Fortpflanzungsgeschwindigkeit des Lichtes und der Körperdichte. *Annalen der Physik*, *245*(4), 641-665.

[23] Rayleigh, L. (1892). LVI. On the influence of obstacles arranged in rectangular order upon the properties of a medium. *The London, Edinburgh, and Dublin Philosophical Magazine and Journal of Science*, *34*(211), 481-502.

[24] Sihvola, A. (2013). Homogenization principles and effect of mixing on dielectric behavior. *Photonics and Nanostructures-Fundamentals and Applications*, *11*(4), 364-373.

[25] Sihvola, A. H. (1999). *Electromagnetic mixing formulas and applications* (No. 47). Iet.

[26] Jackson, J. D. (1999). Classical Electrodynamics John Wiley & Sons. *Inc., New York.*

[27] Karkkainen, K., Sihvola, A., & Nikoskinen, K. (2001). Analysis of a three-dimensional dielectric mixture with finite difference method. *IEEE Transactions on Geoscience and Remote Sensing*, *39*(5), 1013-1018.

[28] Pekonen, O., Kärkkäinen, K., Sihvola, A., & Nikoskinen, K. (1999). Numerical testing of dielectric mixing rules by FDTD method. *Journal of Electromagnetic Waves and Applications*, *13*(1), 67-87.

[29] Garnett, J. M. (1904). Colors in material glasses and metal films. *Trans. Roy. Soc.*, *53*, 385-420.

[30] Sihvola, A. H., & Lindell, I. V. (1992). Polarizability modeling of heterogeneous media Dielectric Properties of Heterogeneous Materials ed A Priou.

[31] Polder, D., & Van Santeen, J. H. (1946). The effective permeability of mixtures of solids. *Physica*, *12*(5), 257-271.

[32] Karkkainen, K. K., Sihvola, A. H., & Nikoskinen, K. I. (2000). Effective permittivity of mixtures: Numerical validation by the FDTD method. *IEEE Transactions on Geoscience and Remote Sensing*, *38*(3), 1303-1308.

[33] Sihvola, A. H., & Kong, J. A. (1988). Effective permittivity of dielectric mixtures. *IEEE Transactions on Geoscience and Remote Sensing*, *26*(4), 420-429.

[34] Matzler, C., & Wegmuller, U. (1987). Dielectric properties of freshwater ice at microwave frequencies. *Journal of Physics D: Applied Physics*, *20*(12), 1623.

[35] Mätzler, C. (Ed.). (2006). *Thermal microwave radiation: applications for remote sensing* (Vol. 52). Iet.

[36] Qi, J., Kettunen, H., Wallén, H., & Sihvola, A. (2010, August). Different retrieval methods based on S-parameters for the permittivity of composites. In *Electromagnetic Theory (EMTS), 2010 URSI International Symposium on* (pp. 588-591). IEEE.

[37] Ghodgaonkar, D. K., Varadan, V. V., & Varadan, V. K. (1990). Free-space measurement of complex permittivity and complex permeability of magnetic materials at microwave frequencies. *IEEE Transactions on instrumentation and measurement*, *39*(2), 387-394.

[38] Belhadj-Tahar, N. E., Fourrier-Lamer, A., & De Chanterac, H. (1990). Broad-band simultaneous measurement of complex permittivity and permeability using a coaxial discontinuity. *IEEE Transactions on Microwave Theory and Techniques*, *38*(1), 1-7.

[39] Qi, J., Kettunen, H., Wallén, H., & Sihvola, A. (2011). Different homogenization methods based on scattering parameters of dielectric-composite slabs. *Radio Science*, *46*(5).

[40] TSMS, WMO, CIMO, Training course on weather radar systems. Module A-F, *Turkey Radar Training 1.0/Alanya*, 2005.

[41] Tsang, L., Kong, J. A., & Ding, K. H. (2000). Scattering of Electromagnetic Waves: Theories and Applications. John Wisley & Sons.

[42] http://micro.magnet.fsu.edu/primer/java/reflection/specular/.

[43] Galin, N. (2012). *Measuring snow thickness over Antarctic sea ice with a helicopter-borne 2-8 GHz FMCW radar* (Doctoral dissertation, University of Tasmania).

[44] Beckmann, P., and A. Spizzichino, *The Scattering of Electromagnetic Waves from Rough Surfaces*, Pergamon Press, New York, NY, 1963.

[45] Sain, A., & Melde, K. L. (2012, July). Surface roughness modeling for CB-CPWs. In *Antennas and Propagation Society International Symposium (APSURSI), 2012 IEEE* (pp. 1-2). IEEE.

[46] Zhou, L., Tsang, L., Jandhyala, V., Li, Q., & Chan, C. H. (2004). Emissivity simulations in passive microwave remote sensing with 3-D numerical solutions of Maxwell equations. *IEEE transactions on Geoscience and Remote Sensing*, *42*(8), 1739-1748.

[47] Ulaby, F. T., Moore, R. K., & Fung, A. K. (1982). Microwave remote sensing: Active and passive. Volume 2-Radar remote sensing and surface scattering and emission theory.

[48] Paillou, P., Crapeau, M., Elachi, C., Wall, S., & Encrenaz, P. (2006). Models of synthetic aperture radar backscattering for bright flows and dark spots on Titan. *Journal of Geophysical Research: Planets*, *111*(E11).

[49] Fung, A., & Eom, H. (1981). Multiple scattering and depolarization by a randomly rough Kirchhoff surface. *IEEE Transactions on Antennas and Propagation*, *29*(3), 463-471.

[50] Ghafouri, A., Amini, J., Dehmollaian, M., & Kavoosi, M. A. (2017). Better Estimated IEM Input Parameters Using Random Fractal Geometry Applied on Multi-Frequency SAR Data. *Remote Sensing*, *9*(5), 445.

[51] Fung, A. K., Chen, K. S., & Chen, K. S. (2010). *Microwave scattering and emission models for users*. Artech house.

[52] Sahebi, M. R., Bonn, F., & Bénié, G. B. (2004). Neural networks for the inversion of soil surface parameters from synthetic aperture radar satellite data. *Canadian Journal of Civil Engineering*, *31*(1), 95-108.

[53] Irena, H. (2001). *Inversion of surface parameters using Polarimetric SAR* (Doctoral dissertation, Ph. D. thesis, DLR–HR).

[54] Barrett, B. W., Dwyer, E., & Whelan, P. (2009). Soil moisture retrieval from active spaceborne microwave observations: An evaluation of current techniques. *Remote Sensing*, *1*(3), 210-242.

[55] Chen, K. S., Kao, W. L., & Tzeng, Y. C. (1995). Retrieval of surface parameters using dynamic learning neural network. *Remote Sensing*, *16*(5), 801-809.

[56] Jin, Y. Q., & Li, Z. (2001). Simulation of scattering from complex rough surfaces at low grazing angle incidence using the GFBM/SAA method. *IEEJ Transactions on Fundamentals and Materials*, *121*(10), 917-921.

[57] Ye, H., & Jin, Y. Q. (2005). Parameterization of the tapered incident wave for numerical simulation of electromagnetic scattering from rough surface. *IEEE Transactions on Antennas and Propagation*, *53*(3), 1234-1237.

[58] Lawrence, H., Demontoux, F., Wigneron, J. P., Mialon, A., Wu, T. D., Mironov, V., ... & Kerr, Y. (2010, March). L-Band emission of rough surfaces: Comparison between experimental data and different modeling approaches. In *Microwave Radiometry and Remote Sensing of the Environment (MicroRad), 2010 11th Specialist Meeting on* (pp. 27-32). IEEE.

[59] Huang, S., Tsang, L., Njoku, E. G., & Chan, K. S. (2010). Backscattering coefficients, coherent reflectivities, and emissivities of randomly rough soil surfaces at L-band for SMAP applications based on numerical solutions of Maxwell equations in three-dimensional simulations. *IEEE Transactions on Geoscience and Remote Sensing*, *48*(6), 2557-2568.

[60] Lawrence, H. (2010). *Modelling the effects of surface roughness and a forest litter layer on passive microwave observations: application to soil moisture retrieval by the SMOS mission* (Doctoral dissertation, Université Sciences et Technologies-Bordeaux I).

[61] Fung, A. K., Shah, M. R., & Tjuatja, S. (1994). Numerical simulation of scattering from three-dimensional randomly rough surfaces. *IEEE Transactions on Geoscience and remote sensing*, *32*(5), 986-994.

[62] www.mysimslab.com.

[63] Oh, Y., Sarabandi, K., & Ulaby, F. T. (1992). An empirical model and an inversion technique for radar scattering from bare soil surfaces. *IEEE transactions on Geoscience and Remote Sensing*, *30*(2), 370-381.

[64] Dubois, P. C., Van Zyl, J., & Engman, T. (1995). Measuring soil moisture with imaging radars. *IEEE Transactions on Geoscience and Remote Sensing*, *33*(4), 915-926.

[65] van Zyl, J. J. (2011). *Synthetic aperture radar polarimetry* (Vol. 2). John Wiley & Sons.

[66] Holmgren, J., Sturm, M., Yankielun, N. E., & Koh, G. (1998). Extensive measurements of snow depth using FM-CW radar. *Cold Regions Science and Technology*, *27*(1), 17-30.

[67] Marshall, H. P., & Koh, G. (2008). FMCW radars for snow research. *Cold Regions Science and Technology*, *52*(2), 118-131.

[68] Rott, H., Yueh, S. H., Cline, D. W., Duguay, C., Essery, R., Haas, C., & Nagler, T. (2010). Cold regions hydrology high-resolution observatory for snow and cold land processes. *Proceedings of the IEEE*, *98*(5), 752-765.

[69] Shi, J. (2006, July). Snow water equivalence retrieval using X and Ku band dual-polarization radar. In *Geoscience and Remote Sensing Symposium, 2006. IGARSS 2006. IEEE International Conference on* (pp. 2183-2185). IEEE.

[70] Jaruwatanadilok, S., Kuga, Y., Ishimaru, A., Hussein, Z. A., & McDonald, K. C. (2004, September). Snow thickness estimation using correlation functions at C-band. In *Geoscience and Remote Sensing Symposium, 2004. IGARSS'04. Proceedings. 2004 IEEE International* (Vol. 6, pp. 3705-3708). IEEE.

[71] Hopsø, I. S. (2013). *Wet snow detection by C-band SAR in avalanche forecasting* (Master's thesis, UiT The Arctic University of Norway).

[72] Baghdadi, N., Gauthier, Y., & Bernier, M. (1997). Capability of multitemporal ERS-1 SAR data for wet-snow mapping. *Remote sensing of environment*, *60*(2), 174-186.

[73] Stiles, W. H., & Ulaby, F. T. (1981). Dielectric properties of snow.

[74] Fayad, A., Gascoin, S., Faour, G., Fanise, P., Drapeau, L., Somma, J.,& Escadafal, R. (2017). Snow observations in Mount Lebanon (2011–2016). *Earth System Science Data*, *9*(2), 573.

[75] Tan, S. (2016). *Multiple volume scattering in random media and periodic structures with applications in microwave remote sensing and wave functional materials*. (Doctoral dissertation, Ph. D. thesis, University of Michigan).

[76] Looyenga, H. (1965). Dielectric constants of heterogeneous mixtures. *Physica*, *31*(3), 401-406.

[77] Shi, J., Xiong, C., & Jiang, L. (2016). Review of snow water equivalent microwave remote sensing. *Science China Earth Sciences*, *59*(4), 731-745.

[78] Lu, D. (2010). Simulation and Verification of Pulse Doppler Radar Systems. *Agilent Technologies Application Note.*

[79] Keysight Technologies, "SystemVue Electronic System-Level (ESL) Design Software," [Online]. Available: http://www.keysight.com/en/pc-1297131/systemvue-electronic-system-level-esl-design-software?cc=US.

[80] Leiss Sr, D., EDA, C. E., & Bhargava, A. (2010). Radar System Design and Interference Analysis Using Agilent SystemVue. *Agilent Technologies Application Note.*

[81] Keysight Technologies, "Keysight EEsof EDA SystemVue," [Online]. Available: http://literature.cdn.keysight.com/litweb/pdf/5990-4731EN.pdf?id=1780933.

[82] Keysight Technologies, "SystemVue Electronic System-Level (ESL) Design Software," [Online]. Available: http://www.keysight.com/en/pc-1297131/systemvue-electronic-system-level-esl-design-software?cc=US.

[83] Ritter, D. M. (2017). Verification of Receiver Equalization by Integrating Dataflow Simulation and Physical Channels. *PhD Thesis*.

Appendices

Appendix A

Reflection Coefficient of Air-Snow-Ground Media in MATLAB

```
clear all;
close all;
clc;
d=0.2; %depth of snow in meters
theta=[0:1:90]; %incidence angle in degrees
theta1 = degtorad(theta); %incidence angle in radians
f=1; %frequency in GHz
eps1 = 1; %permittivity of air
eps2=1.9; %permittivity of dry snow
eps3=11.3-i*1.5; %permittivity of soil
c=3e8; %speed of wave in vacuum
lmda0 = c/(f*1e9); % wavelength in free space

%expression of gamma and eta in air
gamma1 = (1i*20*pi*f*sqrt(eps1))/2.99; % jbeta1 since alpha1=0
eta1 = (376.7/sqrt(real(eps1)))*((1-
1i*(imag(eps1)/real(eps1)))^(-1/2));

%expression of gamma and eta in snow
gamma2 = (1i*20*pi*f*sqrt(eps2))/2.99; % wave number in medium
2 which is jbeta2 since alpha2=0
eta2 = (376.7/sqrt(real(eps2)))*((1-
1i*(imag(eps2)/real(eps2)))^(-1/2));

%expression of alpha,beta,eta, and gamma in soil
alpha3 = ((2*pi)/lmda0)*(0.5*real(eps3)*(sqrt(1 +
(imag(eps3)/real(eps3))^2) - 1))^0.5;
beta3 = ((2*pi)/lmda0)*(0.5*real(eps3)*(sqrt(1 +
(imag(eps3)/real(eps3))^2) + 1))^0.5;
eta3 = (376.7/sqrt(real(eps3)))*((1-
1i*(imag(eps3)/real(eps3)))^(-1/2));
gamma3 = alpha3+i*beta3;

%refraction angle in medium 2
theta2 = acos((1-
((sqrt(eps1)/sqrt(eps2)).*sin(theta1)).^2).^(1/2));

%refraction angle in medium 3
theta3 = acos((1-((gamma1/gamma3).*(sin(theta1))).^2).^(1/2));

%for h-polarization
```

```
%r12 = (sqrt(eps1)*cos(theta1)-
sqrt(eps2)*cos(theta2))/(sqrt(eps1)*cos(theta1)+sqrt(eps2)*cos
(theta2));
r12 = (eta2.*cos(theta1)-
eta1.*cos(theta2))./(eta2.*cos(theta1)+eta1.*cos(theta2));
r23 = (eta3.*cos(theta2)-
eta2.*cos(theta3))./(eta3.*cos(theta2)+eta2.*cos(theta3));

reflection = (r12 + r23.*exp(-2.*gamma2.*d.*cos(theta2)))./(1
+ r12.*r23.*exp(-2.*gamma2.*d.*cos(theta2)));
```

Appendix B

HFSS Script to Import N Spheres

```
Dim oAnsoftApp
Dim oDesktop
Dim oProject
Dim oDesign
Dim oEditor
Dim oModule
Set oAnsoftApp = CreateObject("AnsoftHfss.HfssScriptInterface")
Set oDesktop = oAnsoftApp.GetAppDesktop()
oDesktop.RestoreWindow
Set oProject = oDesktop.SetActiveProject("Project2")
oProject.InsertDesign "HFSS", "HFSSDesign1", "DrivenModal", ""
Set oDesign = oProject.SetActiveDesign("HFSSDesign1")
Set oEditor = oDesign.SetActiveEditor("3D Modeler")
oEditor.CreateBox Array("NAME:BoxParameters", "XPosition:=", "0mm", "YPosition:=", _
  "0mm", "ZPosition:=", "0mm", "XSize:=", "100mm", "YSize:=", "100mm", "ZSize:=", _
  "100mm"), Array("NAME:Attributes", "Name:=", "Box1", "Flags:=", "", "Color:=", _
  "(132 132 193)", "Transparency:=", 0.8, "PartCoordinateSystem:=", "Global", "UDMId:=", _
  "", "MaterialValue:=", "" & Chr(34) & "vacuum" & Chr(34) & "", "SolveInside:=", _
  true)
Set oModule = oDesign.GetModule("BoundarySetup")
oModule.AssignPerfectE Array("NAME:PerfE1", "Faces:=", Array(7), "InfGroundPlane:=", _
  false)
oModule.AssignPerfectE Array("NAME:PerfE2", "Faces:=", Array(8), "InfGroundPlane:=", _
  false)
oModule.AssignPerfectH Array("NAME:PerfH1", "Faces:=", Array(9))
```

```
    oModule.AssignPerfectH Array("NAME:PerfH2", "Faces:=", Array(11))

    oModule.AssignWavePort Array("NAME:1", "Faces:=", Array(12), "NumModes:=", 1,
"RenormalizeAllTerminals:=", _

     true, "UseLineModeAlignment:=", false, "DoDeembed:=", false,
Array("NAME:Modes", Array("NAME:Mode1", "ModeNum:=", _

     1, "UseIntLine:=", true, Array("NAME:IntLine", "Start:=", Array("100mm", "50mm",
_

     "0mm"), "End:=", Array("100mm", "50mm", "100mm")), "AlignmentGroup:=", 0,
"CharImp:=", _

     "Zpi")), "ShowReporterFilter:=", false, "ReporterFilter:=", Array(true),
"UseAnalyticAlignment:=", _

     false)

    oModule.AssignWavePort Array("NAME:2", "Faces:=", Array(10), "NumModes:=", 1,
"RenormalizeAllTerminals:=", _

     true, "UseLineModeAlignment:=", false, "DoDeembed:=", false,
Array("NAME:Modes", Array("NAME:Mode1", "ModeNum:=", _

     1, "UseIntLine:=", true, Array("NAME:IntLine", "Start:=", Array("0mm", "50mm",
"0mm"), "End:=", Array( _

     "0mm", "50mm", "100mm")), "AlignmentGroup:=", 0, "CharImp:=", "Zpi")),
"ShowReporterFilter:=", _

     false, "ReporterFilter:=", Array(true), "UseAnalyticAlignment:=", false)

    Dim radii,centerx, centery, centerz

    radii=Array()

    centerx=Array()

    centery=Array()

    centerz=Array()

    for i=0 To 499

      Dim XValue, YValue, ZValue

      XValue=centerx(i)

      YValue=centery(i)

      ZValue=centerz(i)

      RValue=radii(i)

     oEditor.CreateSphere _

      Array ("NAME:SphereParameters", "XCenter:=", XValue*1e-3, "YCenter:=",
YValue*1e-3, _
```

```
        "ZCenter:=", ZValue*1e-3, "Radius:=", RValue*1e-3), _
        Array ("NAME:Attributes", "Name:=", "Sphere", "Flags:=", "", "Color:=", "(132 132 193)", _
        "Transparency:=", 0, "PartCoordinateSystem:=", "Global", "UDMId:=", "", "MaterialValue:=", "" & Chr(34) & "vacuum" & Chr(34) & "", _
        "SolveInside:=", true)
    Next
```